UNIVERSITY OF CALIFORNIA

Los Angeles

Transport and Removal Mechanisms of Trace Organic Pollutants by Nanofiltration and Reverse Osmosis Membranes

A dissertation submitted in partial satisfaction
of the requirements for the degree Doctor of Philosophy
in Civil Engineering

by

Jinwen Wang

2014

ABSTRACT OF THE DISSERTATION

Transport and Removal Mechanisms of Trace Organic Pollutant by Nanofiltration and Reverse Osmosis Membranes

by

Jinwen Wang

Doctor of Philosophy in Civil Engineering

University of California, Los Angeles, 2014

Professor Eric M. V. Hoek, Chair

Nanofiltration (NF) and reverse osmosis (RO) membrane processes have been proved to be promising advanced treatment technologies for purifying water from trace organic pollutants. In order to accurately predict trace organic pollutants rejection by NF/RO membranes, a fully picture of membrane transport mechanism and how membrane intrinsic properties (*i.e.* membrane structure and chemistry) and surrounding environment (*i.e.* water chemistry) affect membrane performance should be fully explored.

The objective and focus of this study is to fully understand trace organic pollutant transport through NF/RO membranes. A comprehensive review on the mechanisms and models of solute transport relevant to osmosis membrane separation processes was presented. Classical models (*i.e.*, pore flow, solution-diffusion, and Nernst-Planck) and

discuss the shortcomings of each, particularly focusing on their inability to explain fundamental relationships between water/solute transport and membrane properties, such as free volume, crystallinity, extent of swelling, and the presence of filler materials in mixed matrix/nanocomposite membranes were critically reviewed.

An extension of the classical solution-diffusion model had been developed that relates transport through NF/RO membranes directly to membrane structure descriptors (i.e., effective barrier layer pore size, porosity and thickness, etc.). In general, model predictions agreed well with experimental data suggesting the model captures the phenomenological behavior of commercial NF/RO membranes for separations relevant to modern water treatment objectives. The model also provides new mechanistic insights about the "effective structure" of NF/RO composite membranes and how trace organic solutes are rejected. These results suggest it is possible and important to fine-tune the surface energy of membrane and membrane structure (pore size, porosity, thickness) to achieve high membrane selectivity for certain solute.

The effects of feed solution ionic strength, pH and divalent cation content on NF/RO membrane structure and performance were elucidated experimentally and fitted with the newly developed model. All the membranes tested became more hydrophilic and swollen with increasing feed solution ionic strength, pH, and divalent cation concentrations. Generally, water permeabilities of all three membranes decreased with ionic strength and divalent cation content, but increased with pH. For RO membranes, neutral solute rejection decreased with pH and divalent cation content, but increased with ionic strength and the salt rejection remained independent with water chemistry except

for very low pH of 3; for a NF membrane, solute rejection was more sensitive to water chemistry and neutral solute rejection decreased with ionic strength, pH, but increased with divalent cation content. Ultimately, these new insights may be useful in selection of already commercial or design of new NF/RO membranes for removal of chemicals of emerging concern in water treatment.

Four different organic solute removals by six different commercial NF/RO membranes in laboratory re-created groundwater matrix were experimentally determined. In addition, membrane structural descriptors and solute-membrane interaction energies were quantified using the newly developed model. SWRO membranes exhibited excellent removal efficiency (> 90%) for both NDMA and 1,4-dioxane in groundwater, while NF membranes showed inefficient separation. Methanol could not be effectively removed by NF/RO membranes. Correlation studies suggested that both size exclusion and thermodynamic partitioning play important roles in trace organics removal and a partition coefficient, which combines both steric effects and solute-membrane interactions, can be employed to predict organic solute rejection by NF/RO membranes.

The dissertation of Jinwen Wang is approved.

Shaily Mahendra

Michael K. Stenstrom

Richard B. Kaner

Eric M.V. Hoek, Committee Chair

University of California, Los Angeles

2014

TABLE OF CONTENTS

LIST OF FIGURES

LIST OF TABLES

ACKNOWLEGEMENTS

I would like to first and foremost express my sincere gratitude to my advisor, Prof. Eric M.V. Hoek. Since he offered a chance for me to spend a summer in his lab almost six years ago, when I was a junior in college, he has continually pushed me to grow up both in academia and in personality. He has held a very high standard to me and we share the same goal, which is to turn my potential to my ability. He offered numerous opportunities to help me challenge myself and become stronger. The experiences he shared with me will always light the road in front of me. I would also like to thank the other members of my doctoral committee, Prof. Shaily Mahendra, Prof. Michael Stenstrom, and Prof. Richard Kaner for their help and advice during my time at UCLA.

Special thank to Dr. Xue Jin, Dr. Fubing Peng and Dr. Xiaofei Huang for taking me under their wings when I was an undergraduate and helping me to shape myself as a graduate student. Also, special thank to Dr. Gregory Guillen, my “American brother”, thank you for talking to me and teaching me patiently while bearing my awkward English, when I first came to US. I would like to give special thank to Dr. Minghua Li, my friend, roommate, and mentor. In addition to being one of the greatest scientists I have had the pleasure to work with, Minghua shared his invaluable research experience in detail with me. I would like to specifically thank Mavis Wong, MaryTheresa Pendergast, Benjamin Feinberg, Catalina Marambio-Jones and Dukwoo Jun for being great friends and lab-mates. I feel lucky to have the opportunity to spend Ph.D life in this amazing group.

I am grateful for Yibing Mo and Dr. Gil Hurwitz for helping me with experiments. I enjoy the time working and talking with you. I must also acknowledge Dr. Derrick Dlamini, Dr. Guy Ramon, Prof. Viatcheslav Freger, Prof. Arne Verliefde, Prof. Bhekie Mamba, Prof. Shaily Mahendra for their contributions to publications and manuscripts currently in submission or preparation.

Financial support was provided by a scholarship from the Chinese Scholarship Council and by the UCLA Henry Samueli School of Engineering and Applied Science and Department of Civil and Environmental Engineering. I am also grateful for financial and analytical support from Water Planet Engineering, LLC and membrane samples provided by Dow Water Solutions.

Finally, I would like to acknowledge my parents for their unconditional love, morale, encouragement and support throughout the years I lived far from them. My wife, Na, thank you for your love and support, thank you for scarifying yourself to come to US and stay with me.

VITA

2009	B.S. Environmental Science Nankai University Tianjin, China
2011	M.S. Civil Engineering University of California, Los Angeles Los Angeles, California
2012	Teaching Assistant Department of Civil and Environmental Engineering University of California, Los Angeles Los Angeles, California
2009-2014	Graduate Student Researcher Department of Civil and Environmental Engineering University of California, Los Angeles Los Angeles, California

PUBLICATIONS AND PRESENTATIONS

J Wang, Y Mo, S Mahendra, EMV Hoek, Effects of Water Chemistry on Structure and Performance of Polyamide Composite Membranes, Journal of Membrane Science, 452,415-425.

J Wang, DS Dlamini, AK Mishra, MM Pendergast, MCY Wong, BB Mamba, V Freger, ARD Verliefde, EMV Hoek, A Critical Review of Transport Through Osmotic Membranes. Journal of Membrane Science, 454, 516-537

DS Dlamini, J Wang, AK Mishra, BB Mamba, EMV Hoek, Effect of Cross-Linking Agent Chemistry and Coating Conditions on Physical, Chemical and Separation Properties of PVA-PSf Composite Membranes, Separation Science and Technology, 49 (1), 22-29.

M Li, ME Noriega-Trevino, N Nino-Martinez, C Marambio-Jones, J Wang, R Damoiseaux, F Ruiz, EMV Hoek, Synergistic bactericidal activity of Ag-TiO2 nanoparticles in both light and dark conditions, Environmental Science and Technology, 2011, 45(20), 8989-8995.

X Jin, M Li, J Wang, C Marambio-Jones, F Peng, X Huang, R Damoiseaux, EMV Hoek, High-throughput screening of silver nanoparticle stability and bacterial inactivation in aquatic media: influence of specific ions. Environmental Science and Technology, 2010, 44(19), 7321-7328.

EMV Hoek, J Wang, A Jawor, Nanofiltration Separations, in: S Lyshevski (Ed.), The Dekker Encyclopedia of Nanoscience and Nanotechnology, 3rd edition, Taylor & Francis LLC, 2013, Accepted, in Press.

J Wang, Y Mo, MM Pendergast, EMV Hoek, Understanding Uncharged Trace Organic Solute Rejection by Reverse Osmosis and Nanofiltration Membranes, The International Desalination Association World Congress on Desalination and Water Reuse, Tianjin, China, October 2013.

J Wang, Y Mo, S Mahendra, EMV Hoek, Effects of Feed Water Inorganic Chemistry On Polyamide NF/RO Membrane Structure, Interfacial Properties and Removal of Trace Organics, Annual Meeting of North American Membrane Society, Boise, Idaho, June 2013.

J Wang, MM Pendergast, EMV Hoek, Structure-Performance Model to Understand and Improve Neutral Solute Removal by RO/NF Membranes, Annual Meeting of North American Membrane Society, New Orleans, Louisana, June 2012.

J Wang, M Li, EMV Hoek, Enhanced Oil-water Separation with a Centrifugal Separator, 11th International Conference on Petroleum Phase Behavior and Fouling, Jersey City, New Jersey, June 2010.

CHAPTER 1

INTRODUCTION

1.1 General Introduction

Clean water supplies are dwindling in the modern world. While the quantity of fresh water remains relatively constant, the demand of our rapidly increasing population has exploded in the last century [1]. Inefficient use of water, climate change driven water scarcity, and industrial pollution have led to the current state in which nearly 1.8 billion people live in water scarce regions and over 780 million people lack access to improved drinking water [2]. Thanks to global efforts of improved sanitation and infrastructure access to improved drinking water has been expanded significantly in the last 20 years [2]. To ensure further improvements and maintain water security into the future new freshwater sources will need to be explored further, such as reclaimed wastewater and desalinated seawater.

Aqueous trace organic pollutants are synthetic and natural organic compounds, such as industrial chemicals (*e.g.*, solvents, intermediates,petrochemiclas), industrial products (*e.g.*, additives, lubricants), pharmaceutically active compounds (PhACs), endocrine disrupting compounds (EDC), biocides (pesticides, nonagricultural biocides), disinfection by-products, surfactants, and dyes[3, 4]. These organic chemicals are widespread in natural waters at low concentrations (µg/L or ng/L) and are considerably toxic, presenting a major environmental problem around the world [3]. Although the specific health effects of these pollutants at low concentrations are not yet fully understood, it is accepted that drinking water should free of such compounds. Thus, suitable treatment technologies are needed.

Membrane processes are now the primary separation technology used in wastewater reclamation and desalination. These technologies are efficient and effective, but there is a continued need to expand and improve their capabilities [5-9]. Improved NF membranes now enable highly energy-efficient removal of color-causing organic matter, hardness minerals, toxic metals, and chemicals of concern, from both natural and industrial waters [10]. Secondary municipal wastewater effluent, brackish groundwater, industrial wastewaters, and seawater are all purified using RO membranes to produce ultra-pure water for potable, agricultural, and industrial purposes [11]. Engineered osmosis processes, such as FO and pressure retarded osmosis (PRO), may further diversify our water future through low-energy desalination, membrane bioreactors, salinity gradient power, and osmotic energy recovery [12-14]. Membranes can be formed with a wide range of structures, chemistries, and performance characteristics by changing the material or altering the fabrication process [9]. The possibilities are seemingly endless, but effective material tailoring requires some degree of *a priori* knowledge. This intuition is difficult to gain due to the lack of predictive models relating membrane structure and chemistry to performance and a less efficient trial-and-error approach is often taken.

Another remaining challenge is a quantitative understanding of the relationship between NF/RO membrane structure, performance and feed solution chemistry. In a recent review, Luo and Wan comprehensively summarized the effect of solution pH and salt content on NF membrane transport [15]. Different mechanisms are proposed depending on solute type [16-22]. For charged solutes, it is thought that increasing ionic strength, divalent cation content and lower pH all reduce Donnan exclusion, and hence, enhance ion permeation through by charged NF/RO membranes [23, 24]. However, charge interactions cannot explain changes in neutral solute rejection, which have been also observed with changes in feed water chemistry. Some researchers suggest reduction in the Stokes radius of neutral solutes due to salt ions with higher hydration energy outcompeting neutral solutes for water molecules [25, 26]. Membrane swelling and de-swelling have also been proposed to explain changes in neutral solute rejection with differences in feed water pH and ionic strength [19]. Freger and co-workers measured changes in polyamide layer thickness using atomic force microscopy (AFM) after soaking membrane in solution with different salt concentrations and pH [20]. They observed a correlation between the changes in polyamide layer thickness, permeability and solution chemistry (salinity and pH).

Historically, it has been difficult to directly characterize NF/RO membrane structure (pore size, film thickness, porosity) when exposed to different water chemistries. First, the current structure characterization techniques may not be accurate enough to resolve subtle changes [15]. Also, most structural characterization techniques are not conducted in representative filtration conditions (saturated with water and solute, wet, flowing and under positive feed pressure). Many researchers have attempted to calculated membrane structure parameters with neutral solute rejection data based on membrane transport models [15, 27, 28]. Luo and Wan fitted experimental glucose rejection data with a membrane transport model considering steric exclusion to estimate an apparent membrane pore size and structure factor (the ratio of membrane thickness to porosity) for high salinity feeds [23]. Verliefde et al. claimed that solute transport predictions made by assuming only steric exclusion significantly overestimated solute rejection. They established a “solute-membrane affinity” model (essentially an extended solution-diffusion model), which considered both steric effect and solute-membrane interaction, to predict neutral solute rejection by NF membranes [28]. However, in these studies only one background water chemistry was evaluated. Moreover, two structure parameters (pore size and structure factor or the ratio of thickness to porosity) were estimated by one transport equation (solute rejection). With only one equation and two unknowns the structure factor was assumed to extract an apparent pore size.

Recently, nanofiltration (NF) and reverse osmosis (RO) processes have been considered for trace organic removal from ground and surface water. However, low to moderate trace organic solute, especially neutral solute (such as NDMA, 1,4-dioxane), rejection by NF/RO membranes has been reported [29-31]. As reviewed by Bellona et al. [18], solute physical-chemical properties, membrane properties and feed water chemistries were all identified to have influences on organic solute rejection by NF/RO membranes. However, solute rejections depend on the combination of all above parameters, so there is no single parameter can be used to correlate with solute rejection for prediction purpose. And it is hard to characterize some of the above key parameters, such as structural parameters of NF/RO membrane under filtration condition.

1.2 Research Hypothesis and Objectives

Based on the above background review and understanding of transport and removal mechanisms of trace organic pollutant by NF and RO membranes from literatures, the following hypotheses were developed:

1. Solute transport through NF/RO membrane is governed by structure-performance relationship.

2. Background water chemistry changes (1) membrane physical structure due to swelling caused by ions; (2) membrane chemical properties (interfacial energy).

3. Rejection of trace organic pollutants by NF/RO membranes can be correlated with solute-membrane partition coefficient, which represents both steric interaction and solute-membrane interaction.

In order to testify the above hypotheses, the present research has the following objectives:

1. Develop a structure-performance transport model with incorporating solute-membrane interaction for NF/RO membranes.

2. Investigate the effect of water chemistry on NF/RO membrane structure and performance.

3. Illustrate the mechanism of trace organic pollutant removal by NF/RO membranes and develop a feasible method to predict membrane rejection.

1.3 Overview of Dissertation

The present dissertation includes 6 Chapters and 1 Appendix. In Capter1, the hypotheses and the objectives after a general introduction.

Chapter 2 is a critical literature review of transport models for osmotic membranes. In each model, the parameters and methods needed to effectively apply the models are laid out with paying particular attention to the inherent advantages and limitations of each.

Chapter 3 presents the mathematical derivation and experimental validation of new structure-performance transport models, including solution-diffusion-affinity model and solution-diffusion-convection-affinity model. The effects of membrane structure and operation condition on membrane transport have also been illustrated.

In Chapter 4, the newly developed transport model is used to more accurately quantify changes in membrane structure and solute-solvent-membrane interactions due to changes in feed water chemistry (ionic strength, pH and divalent cation content). The mechanism of membrane structure change salt induced membrane swelling/deswelling is also presented.

Chapter 5 discussed the removal mechanism of trace organic pollutant by NF/RO membranes. Different parameters describing solute/membrane structure and solute-membrane interaction are used to correlate with solute rejection. And a partition coefficient, which incorporates both solute-membrane structural properties and solute-membrane interaction, is proposed to predict solute rejection by NF/RO membranes.

Finally, a list of major conclusions and suggestions for future research are included in Chapter 6.

1.4 References

[1] Freshwater Crisis, in: National Geographic, 2012.

[2] Progress on sanitation and drinking-water, in, World Health Organization(WHO)/United Nations International Children's Fund (UNICEF) Joint Monitoring Programme for Water Supply and Sanitation, 2012.

[3] R.P. Schwarzenbach, B.I. Escher, K. Fenner, T.B. Hofstetter, C.A. Johnson, U. von Gunten, B. Wehrli, The challenge of micropollutants in aquatic systems, Science, 313 (2006) 1072-1077.

[4] R.P. Schwarzenbach, T. Egli, T.B. Hofstetter, U. von Gunten, B. Wehrli, Global Water Pollution and Human Health, Annu Rev Env Resour, (2010) 109-136.

[5] M. Takht Ravanchi, T. Kaghazchi, A. Kargari, Application of membrane separation processes in petrochemical industry: a review, Desalination, 235 (2009) 199-244.

[6] P. Bernardo, E. Drioli, G. Golemme, Membrane Gas Separation: A Review/State of the Art, Industrial & Engineering Chemistry Research, 48 (2009) 4638-4663.

[7] M.F. San Román, E. Bringas, R. Ibañez, I. Ortiz, Liquid membrane technology: fundamentals and review of its applications, Journal of Chemical Technology & Biotechnology, 85 (2010) 2-10.

[8] K.P. Lee, T.C. Arnot, D. Mattia, A review of reverse osmosis membrane materials for desalination—Development to date and future potential, Journal of Membrane Science, 370 (2011) 1-22.

[9] M. Ulbricht, Advanced functional polymer membranes, Polymer, 47 (2006) 2217-2262.

[10] W.R. Bowen, H. Mukhtar, Characterisation and prediction of separation performance of nanofiltration membranes, Journal of Membrane Science, 112 (1996) 263-274.

[11] C. Fritzmann, J. Löwenberg, T. Wintgens, T. Melin, State-of-the-art of reverse osmosis desalination, Desalination, 216 (2007) 1-76.

[12] T.Y. Cath, A.E. Childress, M. Elimelech, Forward osmosis: Principles, applications, and recent developments, Journal of Membrane Science, 281 (2006) 70-87.

[13] A. Achilli, T.Y. Cath, A.E. Childress, Power generation with pressure retarded osmosis: An experimental and theoretical investigation, Journal of Membrane Science, 343 (2009) 42-52.

[14] B.J. Feinberg, G.Z. Ramon, E.M.V. Hoek, Thermodynamic Analysis of Osmotic Energy Recovery at a Reverse Osmosis Desalination Plant, Environ Sci Technol, 47 (2013) 2982-2989.

[15] J. Luo, Y. Wan, Effects of pH and salt on nanofiltration—a critical review, J Membrane Sci, 438 (2013) 18-28.

[16] S. Bandini, J. Drei, D. Vezzani, The role of pH and concentration on the ion rejection in polyamide nanofiltration membranes, J Membrane Sci, 264 (2005) 65-74.

[17] C. Bellona, J.E. Drewes, The role of membrane surface charge and solute physico-chemical properties in the rejection of organic acids by NF membranes, J Membrane Sci, 249 (2005) 227-234.

[18] C. Bellona, J.E. Drewes, P. Xu, G. Amy, Factors affecting the rejection of organic solutes during NF/RO treatment - a literature review, Water Res, 38 (2004) 2795-2809.

[19] A. Braghetta, F.A. DiGiano, W.P. Ball, Nanofiltration of natural organic matter: pH and ionic strength effects, J Environ Eng-Asce, 123 (1997) 628-641.

[20] V. Freger, Swelling and morphology of the skin layer of polyamide composite membranes: An atomic force microscopy study, Environ Sci Technol, 38 (2004) 3168-3175.

[21] A. Escoda, P. Fievet, S. Lakard, A. Szymczyk, S. Deon, Influence of salts on the rejection of polyethyleneglycol by an NF organic membrane: Pore swelling and salting-out effects, J Membrane Sci, 347 (2010) 174-182.

[22] A.K. Zander, N.K. Curry, Membrane and solution effects on solute rejection and productivity, Water Res, 35 (2001) 4426-4434.

[23] J. Luo, Y. Wan, Effect of highly concentrated salt on retention of organic solutes by nanofiltration polymeric membranes, J Membrane Sci, 372 (2011) 145-153.

[24] V. Freger, T.C. Arnot, J.A. Howell, Separation of concentrated organic/inorganic salt mixtures by nanofiltration, J Membrane Sci, 178 (2000) 185-193.

[25] L. Piculell, S. Nilsson, Effects of salts on association and conformational equilibria of macromolecules in solution
Surfactants and Macromolecules: Self-Assembly at Interfaces and in Bulk, in: B. Lindman, J. Rosenholm, P. Stenius (Eds.), Springer Berlin / Heidelberg, 1990, pp. 198-210.

[26] A. Bouchoux, H. Roux-de Balmann, F. Lutin, Nanofiltration of glucose and sodium lactate solutions - Variations of retention between single- and mixed-solute solutions, J Membrane Sci, 258 (2005) 123-132.

[27] X.L. Wang, Y.Y. Fang, C.H. Tu, B. Van der Bruggen, Modelling of the separation performance and electrokinetic properties of nanofiltration membranes, Int Rev Phys Chem, 31 (2012) 111-130.

[28] A.R.D. Verliefde, E.R. Cornelissen, S.G.J. Heijman, E.M.V. Hoek, G.L. Amy, B.V.d. Bruggen, J.C. van Dijk, Influence of Solute−Membrane Affinity on Rejection of Uncharged Organic Solutes by Nanofiltration Membranes, Environ Sci Technol, 43 (2009) 2400-2406.

[29] E. Steinle-Darling, M. Zedda, M.H. Plumlee, H.F. Ridgway, M. Reinhard, Evaluating the impacts of membrane type, coating, fouling, chemical properties and water chemistry on reverse osmosis rejection of seven nitrosoalklyamines, including NDMA, Water Res, 41 (2007) 3959-3967.

[30] T. Fujioka, L.D. Nghiem, S.J. Khan, J.A. McDonald, Y. Poussade, J.E. Drewes, Effects of feed solution characteristics on the rejection of N-nitrosamines by reverse osmosis membranes, J Membrane Sci, 409 (2012) 66-74.

[31] V.A.Y. Quintanilla, Rejection of Emerging Organic Contaminants by Nanofiltration and Reverse Osmosis Membranes: Effects of Fouling, Modelling and Water Reuse, CRC Press, 2010.

CHAPTER 2

TRANSPORT THROUGH OSMOTIC MEMBRANES: A CRITICAL REVIEW

2.1. Introduction

A fundamental understanding of the mechanisms at play in membrane separations is crucial to furthering the field and intelligently tuning materials to meet the presently growing needs and applications [1]. Transport models are the tools used to understand membrane transport. Two primary categories exist: phenomenological and mechanistic models [2]. Phenomenological models treat the membrane as a “black box” and describe the separation process in terms of measureable parameters, such as solute passage and water flux. Empirical coefficients are used to represent the separation performance of a membrane by relating measured concentrations in the feed and the permeate streams. While these can be used to characterize performance they offer no mechanistic explanation of separation and are, therefore, difficult to compare between materials. Mechanistic transport models have been developed to relate the separation performance observed in a membrane to the physical (*e.g.*, pore structure, solute size) and chemical properties (*e.g.*, energy of interaction) of the membrane and solute materials. Such structure-performance relationships allow for a more fundamental understanding of membrane transport. Herein, we review the types of membranes and relevant mechanistic transport models for osmotic membrane separations. In each model, we lay out the parameters and methods needed to effectively apply the models, paying particular attention to the inherent advantages and limitations of each.

2.2. State of the Art Osmotic Membranes

2.2.1. Integrally-skinned asymmetric membranes

The majority of membranes currently employed in industry are asymmetric porous membranes [3-5]. In asymmetric porous membranes structure and transport properties vary across the membrane thickness. An asymmetric membrane normally consists of a 0.1-1 μm thick dense layer supported by a highly porous, 100-200 μm thick support layer [3, 4]. The dense layer provides the majority of selectivity for the membrane. Separation properties are determined by the chemical nature, size of pores (0.4-1 nm), and thickness of the skin layer. The porous substructure is assumed to provide mechanical support for the thin and fragile selective layer and thought to have little effect on the separation performance of the membrane. Recently, however, the effects of the support layer chemical properties (*e.g.*, hydrophilicity/hydrophobicity) and pore structure (*i.e.*, pore size and porosity) on composite membrane transport have been re-evaluated [6-9].

2.2.2. Thin film composite membranes

In thin film composite membranes, the porous support layer is generally an integrally skinned membrane formed through the non-solvent induced phase separation (NIPS) process. The skin layer is typically formed through either interfacial polymerization or dip coating followed by cross-linking [4, 10]. The most common thin film chemistry for RO membranes is based on a fully aromatic polyamide (PA) formed by interfacial polymerization of *meta*-phenylenediamine (MDP) and trimesoyl chloride

(TMC), while popular polyamide NF membranes are formed by interfacial polymerization of piperazine and TMC [10]. It is assumed that the dense selective layer formed by interfacial polymerization is heterogeneous throughout its thickness (20-200 nm) and highly cross-linked. The surface properties of a PA film are different from the properties within the PA dense layer because the polymer density is not uniformly distributed [11]. The PA dense layer is highly negatively charged since acyl chloride groups are not fully converted to amide in the formation process; however, it was recently reported that direct titration experiments revealed the simultaneous presence of both positive and negative fixed charges in the dense layer of composite PA NF membranes [12]. Freger and Srebnik proposed the fixed charge is not uniform and the film is actually a “sandwich” comprising two oppositely charged layers [13].

The dense coating layer has historically been treated as a non-porous film. Recently more advanced characterization techniques, such as atomic force microscopy, scanning electron microscopy, transmission electron microscopy (TEM), X-ray photoelectron spectroscopy, electron spin resonance, nuclear magnetic resonance (NMR), small angle X-ray scattering, and molecular dynamics simulation have been employed to reveal the dense layer structure. A highly cross-linked PA skin layer structure with sub-nanoscale pores (0.2-1 nm) and low porosity has been reported in literature [14-20].

2.2.3. Thin film nanocomposite membranes

Mixed-matrix membranes contain both organic and inorganic phases. The first mixed-matrix membranes were produced to enhance the performance of gas separation membranes by providing interconnected flow paths of high diffusion rate materials [21]. In aqueous separations, mixed matrix membranes are generally formed from a polymer matrix with inorganic particles dispersed throughout. Classically, micron-scale inorganic fillers (*e.g.*, zeolites and silicalite) were added to polymer membranes to form preferential flow paths for the fast transport of certain molecules [22, 23]. When nanomaterials (*e.g.*, metal and zeolites nanoparticles) are used as the inorganic filler these membranes are referred to as nanocomposite membranes [24-27]. Inorganic particles may be present throughout the thickness of a symmetric or integrally-skinned membrane or exclusively in the coating film of a composite membrane. In theory, mixed matrices add an additional degree of freedom to membrane fabrication since the advantages of a certain filler material can be imbued into a bulk membrane material [21]. Mixed matrices have been employed to improve the overall mechanical and chemical stability of organic membranes and to add certain functionality to the interface of polymer membranes, for example targeted degradation, reduced fouling, or enhanced selectivity [27-32].

There has been a great deal of interest in using organic-inorganic hybrid membranes as next generation membrane materials for water treatment. In a quest to address low water fluxes in membranes, scientists have attempted to use nanoparticles like TiO_2 [33], carbon nanotubes [34], zeolites [35-37], clay [38], non-porous amorphous silica [6] and many more to enhance water flux. Jeong *et al.* incorporated zeolite nanoparticles in the dense layer of a polyamide membrane and increased the water permeability 1.5 times while maintaining the salt rejection [37]. The authors believed the pore in the zeolites acted as a preferential flow path for water to permeate through, while still being small enough to reject salt ions. Pendergast *et al.* incorporated zeolites in both the dense layer and the support layer of composite RO membranes and found that the nanoparticles help membranes to resist compaction under hydraulic pressure [6]. Unfortunately, to this end very few scientists have studied solvent and solute transport in mixed matrix materials.

2.3. Membrane Transport Models

Numerous phenomenological and mechanistic models have been proposed to describe solute and solvent transport through porous and dense membranes. For dense membranes, perhaps most popular is the "solution-diffusion" model, in which permeants dissolve at the membrane interface and then diffuse through the membrane along the concentration gradient. In this model, separation between different permeants results from dissimilarities in the amount of mass that dissolves per membrane volume and/or the rate at which it diffuses through the membrane [5]. Pore-flow models also exist, in which different permeants are separated by size, frictional resistances, and/or charge. In addition to the solution-diffusion and pore-flow models, the Kedem-Katchalsky and Spiegler-Kedem models employ irreversible thermodynamic arguments to derive solute and solvent transport equations while treating the membrane as a "black box" [39-42]. Recently, solute/solvent-membrane affinity has also been taken into account in the convection-diffusion-affinity model [43]. Finally, mixed-matrix membranes introduce new complexities into membrane transport where multiple phases potentially containing different characteristic pore size, solubility, and diffusivity are present within a single membrane.

2.3.1 Solution-diffusion model

The solution-diffusion model applies to “non-porous” membranes in which separation is a result of differences in solubility and diffusivity of permeates. Lonsdale *et al.* [44] proposed the solution-diffusion model to describe transport in “non-porous” membranes based on four assumptions [44-46]: (1) the membrane morphology is homogeneous and non-porous, (2) the solvent and solute dissolve in the membrane nonporous layer and then each diffuses across it down their respective concentration gradient, (3) the solute and solvent diffuse across the membrane independently, each due to its own chemical potential, (4) the chemical gradients are the result of concentration (activity) and pressure gradients across the membrane. The chemical potential difference (Δμ) is given by

$$\Delta\mu_i = R_g T\, ln\, \Delta a_i + V_i \Delta p \tag{2.1}$$

where a_i is the activity of the solute or solvent, V_i is the molar volume, and Δp is the pressure differential across the membrane. The variation of p, μ, and a across the membrane are show in **Fig. 2.1**.

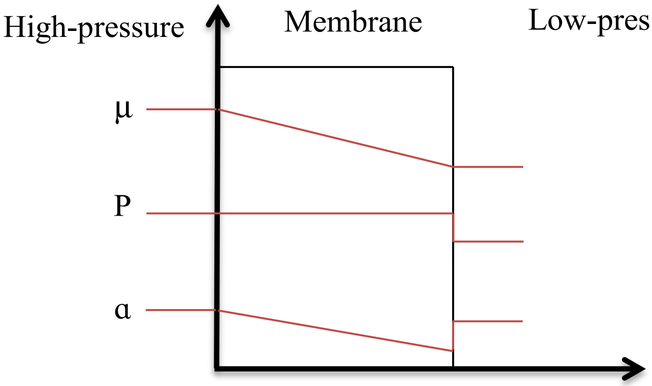

Figure 2.1. Depiction of the assumptions of the solution-diffusion model (adapted from Wijmans *et al.* [47] and Paul [48]), showing chemical potential (μ), pressure (p), and activity (a) gradients across the membrane.

The solution-diffusion model treats permeation with a three-step mechanism: (1) the solutes partition into the polymeric membrane on the feed side, (2) the solutes diffuse through the bulk of the membrane, and (3) the solutes partition into the permeate stream. At present most solute transport studies do not take into account the rate at which the solute or solvent partition into the polymeric membrane of interest, instead they consider diffusion through the membrane as the limiting step. The solution-diffusion process is schematically shown in **Fig. 2.2**. Theoretically, the concentration of component *i* at the feed side membrane surface ($C_{i,1}^{s}$) could be higher or lower than the solute concentration immediately inside the membrane ($C_{i,1}^{m}$); $C_{i,2}^{m}$ and $C_{i,2}^{s}$ are the concentrations just inside and outside the permeate side of the membrane, respectively.

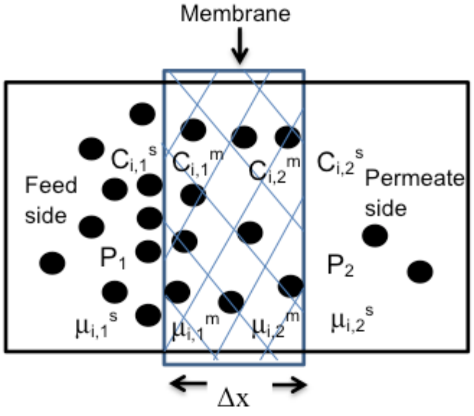

Figure 2.2. Schematic of a solution-diffusion process in a “non-porous” membrane, depicting solutes partitioning into the membrane material at the feed size and then diffusion across the membrane.

There are two parameters used to characterize membrane performance: flux and rejection. Water volumetric flux (J_w) is derived from Henry’s law and Fick’s first law of diffusion and is related to water permeability (A) as follows

$$J_w = A(\Delta p - \Delta \pi) = \frac{K_w D_w^m}{\Delta x} \frac{V_w}{R_g T} (\Delta p - \Delta \pi) \tag{2.2}$$

where $\Delta\pi$ is the osmotic pressure difference across the membrane, D_{wm} is water diffusion coefficient in membrane, K_w is water-membrane partition coefficient ($[\mathrm{kg_{water}} \cdot \mathrm{m^{-3}}_{\mathrm{membrane}}]/[\mathrm{kg_{water}} \cdot \mathrm{m^{-3}}_{\mathrm{solution}}]$), Δx is membrane thickness, and V_w is molar volume of water.

For the solute flux (J_s), Henry's law is ignored because it is assumed that chemical potential gradient due to pressure is negligible. J_s is derived from Fick's law with the assumption that the driving force is almost entirely due to concentration differences,

$$J_s = J_w C_p = B(C_m - C_p) = \frac{K_s D_s^m}{\Delta x} (C_m - C_p) \tag{2.3}$$

Here, D_s^m is the solute diffusion coefficient in the membrane, K_s is the solute-membrane partition coefficient, and C_p and C_m are the solute concentrations in the permeate bulk and at the membrane surface on the permeate side, respectively.

The definition of solute rejection by a membrane is either the observed rejection (R_o) or real rejection (R_r). Observed rejection is calculated from bulk feed (C_f) and the permeate concentrations according to

$$R_o = 1 - \frac{C_p}{C_f} \tag{2.4}$$

while the real rejection *is* calculated from membrane surface and the permeate concentrations as

$$R_r = 1 - \frac{C_p}{C_m} \tag{2.5}$$

Here, the difference between C_m and C_f is due to rejected solute concentration polarization (see **Section 2.5.1** for detailed discussion). However, from the solution-diffusion model (**Eqns. 2.3-2.5**), the real rejection is determined by the apparent solute permeability coefficient ($B = K_s D_s / \Delta x$ in **Eqn. 2.3**) and the water flux as

$$R_r = \frac{J_w}{J_w + B} \tag{2.6}$$

One can predict the basic performance behavior of an RO membrane based on **Eqns. 2** and **6**. Results for a typical seawater RO membrane are shown in **Fig. 2.3**. Water flux linearly increases with increasing applied pressure and salt rejection increases with both water flux and applied pressure.

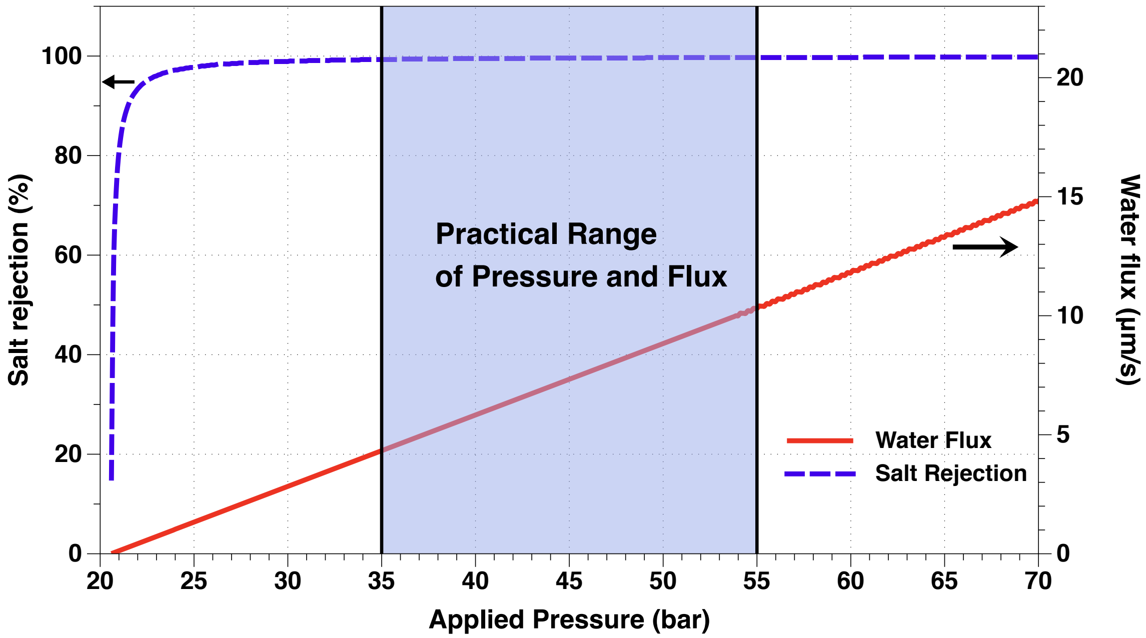

Figure 2.3. Salt rejection and water flux as function of applied pressure ($A = 3 \times 10^{-12}$ m/Pa.s, $B = 3 \times 10^{-8}$ m/s, and $\Delta\pi = 2$ bar)

The solution-diffusion model is widely used to predict the performance of "non-porous" membranes in water treatment applications like NF and RO, as well as dialysis, gas separations, and pervaporation [49-60]. The solution-diffusion model was first used to describe the permeation of gases through a dense rubber septa membrane [61]. Most recently, Miyagi *et al.* [62] studied the transport mechanism of binary organic solvent system through a PDMS-based dense membrane using a regular solution model combined with a solution-diffusion model. Han *et al.* [63] investigated the transport of toluene through organic solvent silicone rubber membranes and concluded that the solution-diffusion model may be suitable for describing the transport of solvent through a membrane. Subramanian *et al.* [64] used the solution-diffusion model to investigate the separation of oil constituents by PDMS-based composite membranes. They used the following systems: triglyceride–tocopherol, triglyceride–oleic acid, and vegetable oil-hexane systems and they observed that diffusivity and solubility of the solvent depends on the molecular weight of solvents.

Despite being widely applied, there are known limitations for the solution-diffusion model. For example, Soltanieh and Gill [45] indicated that this model is limited to membranes with low water content, at which the pore flow can be neglected. Another limitation of the model was discovered by Mazid [65], where it was pointed out that it does not adequately describe J_w and J_s for many RO membranes. These deviations were believed to be due to imperfections in the membrane barrier layer, pore flow (convection effects), and solute-solvent-membrane interactions. To address these shortfalls, a new model was formulated: the solution-diffusion imperfection model. This model was used by Yaroshchuk [66] to describe solute transport in NF membranes and most recently it was used by Fierro *et al.* [67] as a method to describe organic solvent NF of multi-component systems. Yaroshchuk [68] further revised the solution-diffusion imperfection model to account for the fact that the solute concentration at the exit of an imperfection is decreased due to solute diffusion along the membrane towards the surrounding perfect regions.

2.3.2 Pore models

2.3.2.1 Pore-flow (PF) model

Transport through porous membranes is dominated by size exclusion and can be described by the PF model [67]. This model, proposed by Okada and Matsuura [69], is relatively new. The PF model is based on three assumptions: (1) fluids on either side of membrane are in equilibrium with the membrane at the interface, meaning that there is a continuous gradient of chemical potential (μ) across the membrane, (2) the solute and solvent activity gradients across the membrane are zero and the chemical potential gradient across the membrane can be expressed as a pressure gradient, and (3) straight cylindrical pores exist across the thickness of the membrane. The first two assumptions are depicted in **Fig. 2.4**.

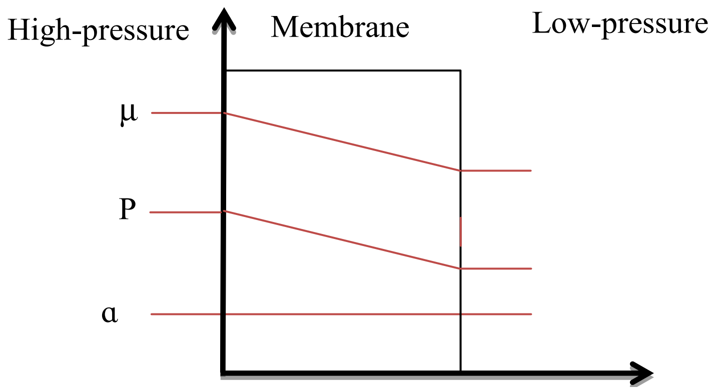

Figure 2.4. Depiction of the assumptions of the pore-flow model (adapted from Wijmans *et al.* [47] and Paul [48]), showing chemical potential (μ), pressure (*P*), and activity (*a*) gradients across the membrane.

Considering the mass transport of a single component (water) system, the liquid transport in porous membranes is described by the Darcy's equation in terms of water flux (J_w) as follows, [70, 71]

$$J_w = \frac{A}{\delta}\left(p_f - p_p\right) \tag{2.7}$$

Whereas the solute flux (J_s) is expressed as follows

$$J_s = \frac{B}{\delta}\left(p_f^2 - p_p^2\right) \tag{2.8}$$

where A is the liquid (solvent) phase transport parameter, B is the solid (solute) phase transport parameter, P_f and P_p are the pressure in the feed and permeate side of the membrane, respectively, and δ is the pore length. The PF model has not been widely used for solute transport description in membrane technology. Banerjee *et al.* [72] used a combination of osmotic pressure and pore flow diffusion to quantify the flux decline and solute rejection, establishing that the PF model gives an idea of the comparative fluxes of ions within the membrane pore. The pore-flow model only considers axial solute concentration gradients. Most of the data and discussion in the literature regarding pore flow of solutes does not explain the role of pore shape relative to solute shape. In addition, the effect of tortuosity in solute rejection and transport has not been clearly stated in present PF models.

2.3.2.2 Modified surface force-pore flow model

The surface force-pore flow (SF-PF) model, which was first proposed by Matsuura and Sourirajan [73], provided a two-dimensional extension of PF model. The SF-PF model assumes: (1) the membrane is micro-porous with cylindrical pores, (2) water transports through the membrane by viscous flow, (3) solute transports through the membrane by both diffusion and convection in pores, and (4) transport through the membrane pores is determined by interaction forces, friction forces, and chemical potential gradients of the water and solute [74, 75]. Since the SF-PF model related membrane performance with both membrane structure (*i.e.* pore size and pore length) and membrane-solute interactions (*i.e.* an electrostatic or a Lennard-Jones type surface potential function), it shows potential to provide more accurate prediction results [73, 76]. However, Mehdizadeh *et al.* indicated that SF-PF model employed a flawed form of material balance and an inconsistent potential function in the pore with the cylindrical pore geometry. As a result, the SF-PF model predicted physically unacceptable results. They corrected the conceptual errors and proposed a modified surface force-pore flow (MD-SF-PF) model [77].

In the MD-SF-PF model, a force balance on a water element in the membrane pore (with pore radius r_p) within axial position z and z + dz and between radial position r and r + dr results in a velocity profile as follows [77],

$$\frac{d^2\alpha(\rho)}{d\rho^2}+\frac{1}{\rho}\frac{d\alpha(\rho)}{d\rho}+\frac{\Delta\wp-\Delta\Pi\left(1-e^{-\Phi(\rho)}\right)}{\beta_1}-\frac{\alpha(\rho)e^{-\Phi(\rho)}}{\beta_1}\left(1-\frac{1}{b(\rho)}\right)\left(1+\frac{\Delta\Pi}{e^{\alpha(\rho)}-1}\right)=0 \quad (2.9)$$

where ρ is dimensionless radial distance in the pore ($\rho = r/r_p$), $\alpha(\rho)$ is dimensionless velocity in the pore ($\alpha(\rho) = \mu_w(\rho)\delta/D_s$), β_1 is dimensionless water viscosity in the pore ($\beta_1 = \eta D_s^w/(r_p^2\pi_2)$), $\Delta\wp = \Delta p/\pi_2$, $\Delta\Pi = (\pi_2-\pi_3)/\pi_2$, $b(\rho)$ is friction parameter at position ρ ($b(\rho) = D_s^w/ D_s^m(\rho)$, where D_s^w is solute diffusivity in bulk solution, $D_s^m(\rho)$ is solute diffusivity in the pore at position ρ), $\mu_w(\rho)$ is water chemical potential, $\Phi(\rho)$ ($\Phi(\rho) = \phi(r)/R_gT$, where $\phi(r)$ is surface wall potential, which represents the net body force acting on the solute by membrane pore wall) is dimensionless potential function, η is water viscosity, π_i is osmotic pressure at location i. The subscripts 1, 2 and 3 refer to feed solution, boundary layer solution and permeate solution, respectively. The boundary conditions for **Eqn. 2.9** are

$\alpha(\rho) = 0$ at $\rho = 1$ (at the pore wall, μ_w is zero)

and

$d\alpha(\rho)/d\rho = 0$ at $\rho = 0$ (at the center of pore, μ_w is constant).

The average solute (with solute radius r_s) flux and water flux can be found by integrating the velocity profile equation over the cross-sectional area as

$$\overline{J_w} = 2\left(\frac{R_gT}{\delta X_{sw}}\right)\int_0^1 \alpha(\rho)\,d\rho \quad (2.10)$$

and

$$\overline{J_s} = 2\left(\frac{1}{\delta X_{sw}}\right)\int_0^{1-\frac{r_s}{r_p}} \frac{\alpha(\rho)}{b(\rho)}\left(\pi_2 + \frac{\pi_2 - \pi_3}{e^{\alpha(\rho)} - 1}\right)e^{-\Phi(\rho)}\rho\, d\rho \tag{2.11}$$

where X_{sw} is the friction constant between solute and water ($X_{sw} = F_{sw}/\Delta \mathrm{u}_{\mathrm{sw}}$, where F_{sw} is friction force between solute and water and Δu_{sw} is difference in velocity of solute and water in pore). With the solute flux and water flux, permeate solute concentration (C_p) can be calculated by

$$C_p = \frac{\overline{J_s}}{J_w} \tag{2.12}$$

Mehdizadeh *et al.* found that the simulation results from MD-SF-PF model were consistent with RO membrane performance [77, 78]. Jain and Gupta [76] incorporated concentration polarization into the MD-SF-PF model and reported that the model predictions of rejection were similar to those simulated by the Spiegler-Kedem model (See **Section 2.3.3**). However, the model failed to provide accurate prediction when some dilute organics, which caused substantial decreases in water flux, were present in solution [79]. The dimensionless transport equations in the MD-SF-PF model can be solved by computational fluid dynamics [80] and Monte Carlo simulations [81].

2.3.3 Irreversible thermodynamics model

Early membrane transport models based on the principle of irreversible thermodynamics correlate transport with mechanical and osmotic pressure gradients. These models assume that the membrane near to equilibrium and the system can be divided into small sub-systems in which local equilibrium exists. Fluxes are derived from phenomenological thermodynamic relationships [82, 83]. These models do not, however, provide insights into mechanistic transport. The Kedem-Katchalsky model is one such model. This model defines J_w as a function of the trans-membrane pressure gradient driving force,

$$J_w = A\left(\Delta p - \sigma \Delta \pi\right) \tag{2.13}$$

The reflection coefficient (σ) was introduced to characterize flux interactions when water and solute cross the membrane through a common channel. According to Wijmans *et al.* [47], $\sigma < 1$ indicates a semi-permeable solute, while $\sigma = 1$ indicates an impermeable solute (complete rejection). In the case of binary solutions, the transport of solutes can be described by

$$J_s = B\Delta\pi + \left(1 - \sigma\right) C_{avg} J_w \tag{2.14}$$

where C_{avg} is the average concentration in the membrane pores. A number of researchers have pointed out that the application of the classical Kedem-Katchalsky model is limited to sufficiently dilute and well-stirred membrane systems with two component solutions [84-87]. The key phenomenological parameters of the Kedem-Katchalsky model are defined as

$$A = \left(\frac{J_w}{\Delta p}\right)_{\Delta\pi = 0} \tag{2.15}$$

$$\sigma = \left(\frac{\Delta p}{\Delta \pi}\right)_{J_w = 0} \tag{2.16}$$

$$B = \left(\frac{J_s}{\Delta \pi} \right)_{J_w = 0} \tag{2.17}$$

and

$$\Delta \pi = R_g T \Delta C \tag{2.18}$$

The real rejection can be expressed as

$$R_r = \frac{C_{avg} J_w + \omega \Delta \pi}{\sigma C_{avg} J_w} \tag{2.19}$$

Because the Kedem-Katchalsky model treats the membrane as a black box, it can be used to describe transport through all types of membranes. Kargol *et al.* [88] investigated RO membrane performance with this model and mechanistic transport equations. Koválcsa *et al.* [89] used the Kedem-Katchalsky model to interpret the performance of an NF membrane in amino acid rejection. Fukuda *et al.* [90] applied the Kedem-Katchalsky model in envisaging a dual solute (KCl-sucrose) system when an impermeable ion is present in the salt-water solution. Paynter *et al.* [91] investigated the dependence of membrane transport properties on temperature using the Kedem–Katchalsky model. Jarzyńska and Pietruszka [92] found that the solvent permeability (*A*) of an aqueous solution of ethyl alcohol depends on the concentration of the solution flowing through the membrane. The dependence of the Kedem–Katchalsky model coefficients on concentration is one of its major disadvantages [45] and the significant difference in concentration across the membrane invalidates the linear irreversible thermodynamics relationships [93]. The model was modified by Spiegler and Kedem [94] to avoid concentration dependence of the transport parameters.

As with Kedem-Katchalsky, the Spiegler-Kedem model is based on irreversible thermodynamics. The major difference between the two models is that the Spiegler-Kedem characterizes membranes in terms of two parameters: solute permeability, *B*, and reflection coefficient, *σ*, and these parameters have no dependence on concentration [95]. Therefore, the Spiegler-Kedem model defines J_w the same way as the Kedem-Katchalsky model, but defines J_s as

$$J_s = B\Delta x \frac{dc}{dx} + \left(1-\sigma\right) J_w C \tag{2.20}$$

Eqn. 2.20 can be integrated across the membrane to yield [76, 83]

$$R_r = 1 - \frac{C_p}{C_m} = \sigma\left(\frac{1-Y}{1-\sigma Y}\right) \tag{2.21}$$

where

$$Y = exp\left[-\frac{J_w\left(1-\sigma\right)}{B}\right] \tag{2.22}$$

Due to the difficulty in estimating the characteristic membrane parameters in **Eqns. 2.21** and **2.22**, the Spiegler-Kedem model is usually coupled with liquid film theory (**Section 2.5.1**) to yield [76, 83, 96]

$$\frac{R_o}{1-R_o} = \frac{\sigma}{1-\sigma}\left\{1 - exp\left[-\frac{J_w\left(1-\sigma\right)}{B}\right]\right\} exp\left(-\frac{J_w}{k_f}\right) \tag{2.23}$$

Observed solute rejection increases with permeate water flux and reflection coefficient, but decreases with solute permeability (**Fig. 2.5**). By using a non-linear parameter estimation technique, the unknown membrane characteristic parameters (*B,* σ,

k_f) can be determined from the given experimental data of R_o and J_w. The solution-diffusion, solution-diffusion imperfection, Kedem-Katchalsky, and Spiegler-Kedem models are frequently used to describe solute transport in NF and RO membranes at laboratory scale [97-100].

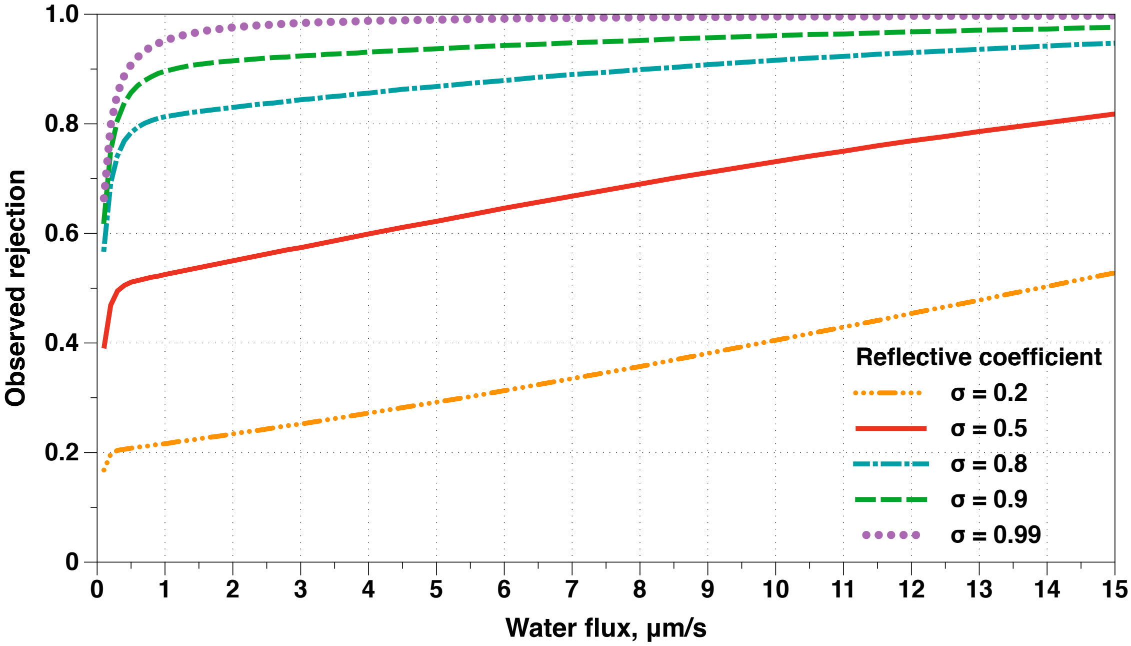

(a)

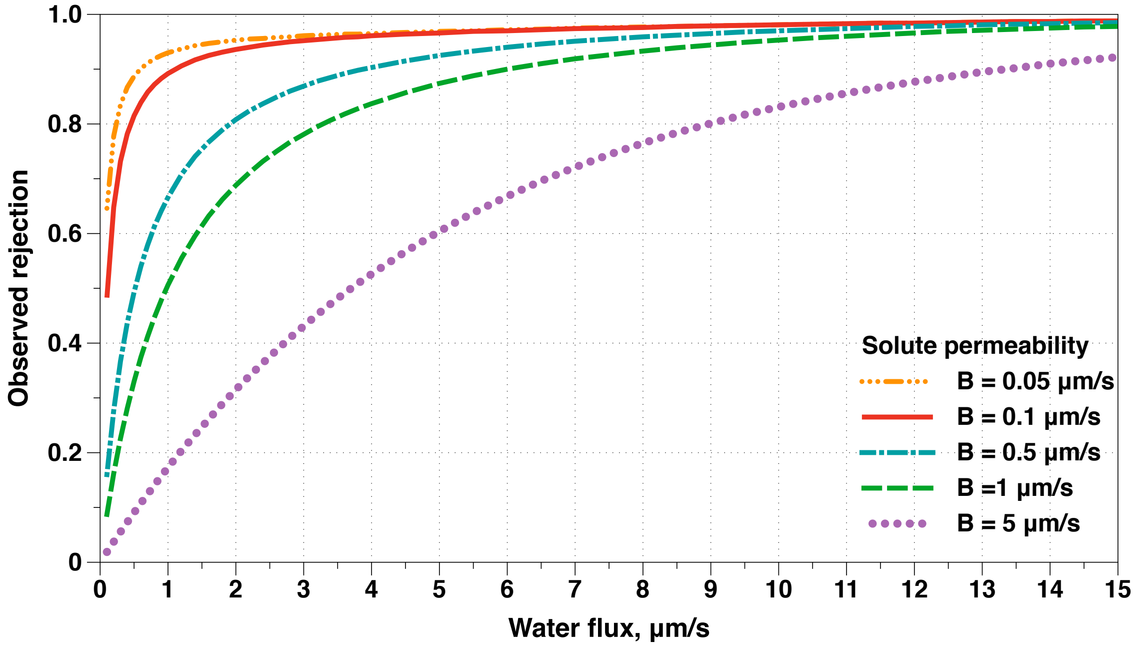

(b)

Figure 2.5. Effect of (a) reflection coefficient (k_f = 10 μm/s, B = 0.05 μm/s) and (b) solute permeability (k_f = 10 μm/s, σ = 0.95) on solute observed rejection based on the Spiegler-Kedem model.

2.3.4. Electrolyte transport and electrokinetic models

For charged solutes (*e.g.*, salt, organic acid) electrokinetic models can be used to describe membrane separations. If the solute concentration within the pore and the concentration gradient along the pore are assumed to be very small the transport modeling in the membrane is based on the extended Nernst-Planck (ENP) equation, which describes solute transport as a combination of diffusion, convection, and electro-migration [101-104]. The governing equation for the steady-state flux, J_i, of a charged solute *i* with charge z_i through membrane pore is

$$J_i = J_w C_{i,p} = -K_{i,d} D_i^{\infty} \frac{dc_i}{dx} + K_{i,c} c_i J_w - \frac{z_i c_i K_{i,d} D_i^{\infty} F}{R_g T} \frac{d\psi}{dx} \tag{2.24}$$

where D_i^{∞} is the solute diffusion coefficient at infinite dilution, $K_{i,d}$ and $K_{i,c}$ are the diffusive and convective hindrance factors accounting for the effect of finite pore size [105], F is the Faraday constant, and ψ is the electrical potential within the pore length, due to charge accumulation close to the pore wall [102]. In some cases, the membrane zeta-potential is taken as an approximation of ψ.

The concentration gradient of an ion i through the membrane can be described as

$$\frac{dc_i}{dx} = \frac{J_w}{K_{i,d} D_i^{\infty}} \left(K_{i,c} c_i - C_{i,p} \right) - \frac{z_i c_i F}{R_g T} \frac{d\psi}{dx} \tag{2.25}$$

Here, $d\psi/dx$ is the electrical potential gradient along the membrane pore length, which is the driving force for the electrical mobility of the ions. The electrical mobility contribution assumes a constant electric field within the membrane pore and, thus, requires invoking a zero current condition,

$$I = \sum_i F z_i J_i = 0 \tag{2.26}$$

and a local electro-neutrality in the membrane,

$$\sum_i z_i c_i + X = 0 \tag{2.27}$$

where X is the charge density (charge/volume) in the membrane pore [106]. Combining **Eqns. 2.25 – 2.27**, yields [101]

$$\frac{d\psi}{dx} = \frac{J_w \sum_i \frac{z_i}{K_{i,d} D_i^{\infty}} \left(K_{i,c} c_i - C_{i,p} \right)}{\frac{F}{R_g T} \sum_i z_i^2 c_i} \tag{2.28}$$

Substituting **Eqn. 2.28** into **Eqn. 2.24** yields

$$\frac{dc_i}{dx} = \frac{J_w}{K_{i,d} D_i^{\infty}} \left(K_{i.c} c_i - C_{i,p} \right) - \frac{z_i c_i J_w}{\sum_i z_i^2 c_i} \sum_i \frac{z_i}{K_{i,d} D_i^{\infty}} \left(K_{i.c} c_i - C_{i,p} \right) \tag{2.29}$$

The boundary conditions for **Eqn. 2.29** are [107]

$$c_i = c_{i,m} \qquad \text{at } x = 0$$

and

$$c_i = c_{i,p} \qquad \text{at } x = \Delta x.$$

Combining **Eqns. 2.24** and **2.29**, ionic fluxes and permeate concentrations corresponding to a given feed side membrane surface concentration and permeate flux can be solved. A more detailed procedure could be found in Bowen *et al.* [14, 108, 109] and Bhattacharjee *et al.* [101].

The above ENP equations combined with the electroneutrality condition require accurate values of certain model parameters, such as membrane effective fixed charge density and membrane thickness, which are difficult to characterize [108]. The non-linear differential equations in the model may also be difficult to solve analytically and fit to experimental data for more than three ionic species in the system [104, 110, 111]. Nevertheless, ENP provides a complete formal framework for describing ionic transport through membranes [108, 110, 112-115]. The only essential assumption is the ideal linear relations hold for each term in **Eqn. 2.24**, (*e.g.*, linearity is assumed between the ion diffusion flux and its activity gradient) [116].

To successfully implement the ENP model two additional models are required: (1) a thermodynamic model of ion exclusion to calculate local concentrations, c_i, (usually within the boundary conditions at membrane-solution interfaces) and (2) a kinetic model to calculate ion hindrance factors $K_{d,i}$ and $K_{c,i}$ [58, 117]. At present, theoretical relations derived for motion of spherical or ellipsoid particles within cylindrical channels are commonly used to calculate hindrance factors [118, 119]. The validity of these macroscopic relations derived for continuous fluids and ideal cylindrical pores when applied to NF and RO membranes – which have irregular pores of molecular dimensions – has not been seriously questioned so far. Presumably, with a proper choice of an effective pore radius they provide a reasonable approximation for the dependence of hindrance factors on the solute radius. However, the distributions of effective pore sizes may lead to rejections lower than 100% for solutes slightly larger than the average effective pore radius.

The ion exclusion relations present the most significant challenge in developing an adequate description of NF membranes. The approach widely used at present views the exclusion mechanism as a combination of Donnan, dielectric, and steric exclusion, which yields the following relation [117, 120-125],

$$\frac{c_i}{C_i} = \left(1-\lambda\right)^2 exp\left(-\frac{Fz_i\Delta\psi_D + \Delta W_i}{R_g T}\right) \tag{2.30}$$

where $\Delta\Psi_D$ and ΔW_i are the electric (Donnan) potential difference and solvation energy difference, respectively, of the ion between membrane and solution. ΔW_i is usually calculated using the Born equation with an appropriately chosen radius of the ion [120]. For known solution composition at the interfaces (c_i) and fixed charge of the membrane (X) the value of Donnan potential $\Delta\Psi_D$ is found by substituting **Eqn. 2.30** for all mobile ions into **Eqn. 2.27**.

Eqn. 2.30 embeds a few critical assumptions, namely: (1) the membrane and/or pore interior are continuous and uniform dielectric media, (2) the ionic species in the membrane are fully dissociated and retain full translational freedom, and (3) ions in the membrane interact with each other and with fixed charges only via a uniform Donnan potential and any pair-wise interactions are negligible. A certain controversy is yet unresolved as to which values of ionic radii are to be used, however, this model or its more sophisticated versions have been widely applied to modeling ion transport in NF and RO [126]. They usually yield good fits for single salts and, using Born or Pauling (bare) radii of the ions, qualitatively agree with the observed effects of ion size on rejection; however, several recent studies demonstrate important discrepancies.

(1) The model fails to consistently describe both single salts and salt mixtures using the same set of parameters [121, 125, 127].

(2) The fitted values of membrane characteristics, such as ε_m or X, significantly vary with feed solution composition [124].

(3) The values of ε_m or X fitted to filtration data strongly disagree with independently measured physical characteristics of the active layer, in particular,

fixed charge measured by Rutherford backscattering spectrometry (RBS) [12, 127-129] and known dielectric characteristics of polymer films swollen in water [130, 131].

(4) The model entirely fails to explain observed dependence of rejection on salt concentration, in particular, for divalent cations [57, 117, 132];

(5) Measurements of salt partitioning by RBS show that the model greatly underestimates salt partitioning and the strength of salt exclusion within RO membranes [133].

These results indicate some fundamental flaws of the physical mechanism assumed in **Eqn. 2.30**. It was recently suggested that one possible reason for the failure is disregard of ion association [117], which should be addressed in future model development [134, 135].

2.4. Additional Transport Considerations

2.4.1. Mixed-matrix membrane models

Studies of transport through mixed-matrix membranes have been conducted experimentally and theoretically since the 1960s [136]. In order to obtain an equation to relate composite membrane permeability to the both matrix phase and the filler phase permeability, and the concentration of the fillers, an analog of transport in mixed matrix membranes in dielectrics (Maxwell model) has been studied comprehensively [136-139]. In the case of a dilute dispersion of spherical fillers, fully oriented along the axis of the applied pressure difference, the effective composite membrane permeability is determined as

$$P_{eff} = P_m \left[\frac{P_d + 2P_m - 2\theta_d \left(P_m - P_d \right)}{P_d + 2P_m + \theta_d \left(P_m - P_d \right)} \right] \tag{2.31}$$

where P is the single component permeability, θ_d is the fraction of dispersed filler material in the membrane, and the subscripts d and m refer to the dispersed and continuous phases, respectively [139]. **Eqn. 2.31** can be rewritten in the form of relative permeability as [137]

$$\frac{P_{eff}}{P_m} = \frac{\frac{P_d}{P_m}\left(1+2\theta_d\right)+\left(2-2\theta_d\right)}{\frac{P_d}{P_m}\left(1-\theta_d\right)+\left(2+\theta_d\right)} \tag{2.32}$$

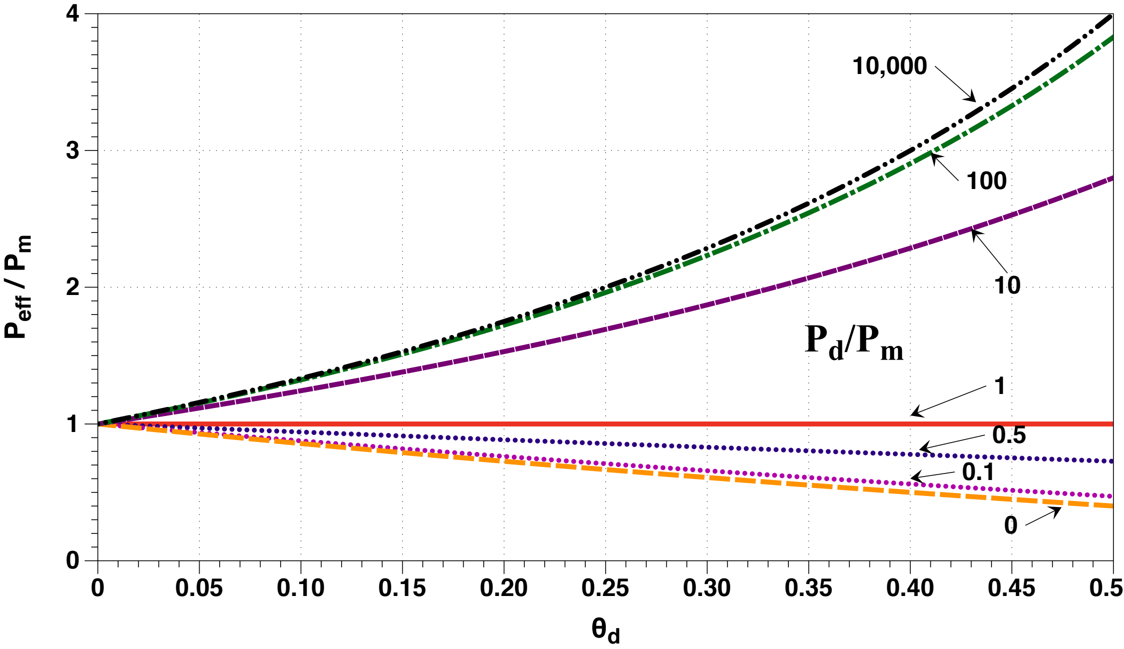

Figure 2.6. Effect of filler volume fraction, θ_d, on the ratio of composite to polymer matrix permeability. Lines drawn represent constant ratio of pure dispersed and continuous phase permeabilities.

Based on **Eqn. 2.32**, a plot of the ratio of effective composite membrane permeability to polymer matrix permeability versus volume fraction of the dispersed fillers can be drawn to indicate the effect the dispersed filler material (**Fig. 2.6**). At extreme ratios of filler permeability to matrix permeability (greater than 100 or less than 0.1) the permeability of the composite becomes less sensitive to the presence of the filler. In the case of high dispersed phase permeability the local direction of the permeate flux is towards the filler particle, while in case of a low dispersed phase permeability the local fluxes preferentially go around the filler particle. Furthermore, if an impermeable or less permeable filler material is used there will be no increase in the effective permeability of the material, in fact it there will be a decrease, unless defects are formed at the dispersed-continuous phase interface [8]. A more detailed explanation can be found in the report published by Bouma *et al*. [137].

2.4.2. Composite membrane transport

The support layer of a composite membrane has long been thought to contribute only mechanical stability and to play no significant role in transport. Until recently, limited information existed in literature about the impacts of support membrane physical–chemical properties on composite membrane formation and resulting performance. One exception is FO membranes, where the support structure determines the extent of internal concentration polarization, reduces the osmotic driving force, and thereby hinders performance (**Section 2.5.2**). It is now thought that the surface chemistry and pore structure of the support membrane may influence the thickness, roughness, and cross-linked structure of NF and RO films, especially those formed by interfacial polymerization. Furthermore, the pore size and porosity of the underlying support may contribute significantly to the diffusive transport through the composite structure. The support membrane material is typically considered an impermeable barrier to species diffusing across the coating film. This means that diffusing species will follow preferential flow paths through the coating film to reach open pores in the underlying support structure. This results in an increase in the effective diffusive path length for water and salt, which impacts water and salt flux (**Fig. 2.7**) [6].

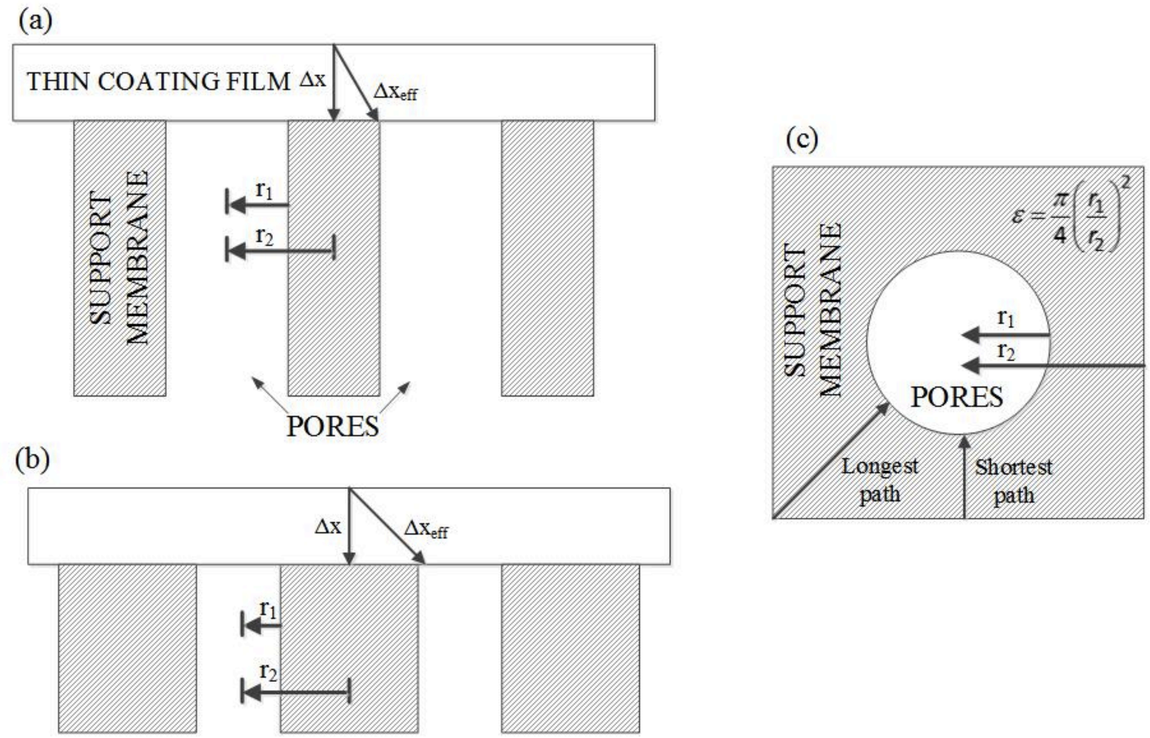

Figure 2.7. Schematic depictions of the effective diffusive path length for different composite membrane structures, such as a) a membrane with a thin coating film and large underlying pores, *versus* b) a membrane with smaller pores and a larger effective path length. c) Finally, an aerial view of the support membrane structure and the effect of pore size and porosity on diffusive path length. Adapted from Pendergast *et al.* [6].

Based on Fick`s law, the ratio of the “real” flux (J_{real}) or permeability (P_{real}) to “ideal” flux (J_{ideal}) or permeability (P_{ideal}) will be identical to the inverse ratio of “real (effective)” diffusive path length (Δx_{eff}) to “ideal” diffusive path length (Δx) by assuming diffusivity and concentration gradient are identical. (Note that this is only valid when the permeate concentration is much smaller than the feed concentration.) Symbolically,

$$\frac{J_{real}}{J_{ideal}} = \frac{\Delta x}{\Delta x_{eff}} = \frac{P_{real}}{P_{ideal}} \tag{2.33}$$

where Δx_{eff} can be derived geometrically from **Fig. 2.7** as

$$\Delta x_{eff} = \varepsilon \Delta x + (1-\varepsilon)\left(\Delta x + \sqrt{\frac{\pi r_1^2}{2\varepsilon}} - r_1 \right) \tag{2.34}$$

Following **Eqns. 2.33** and **2.34**, permeability ratio is plotted in **Fig. 2.8** over a range of coating film thicknesses (Δx), support membrane porosities (ε), and support membrane pore radii (r_1). For a fixed r_1, membranes with smaller Δx are intrinsically more permeable (**Fig. 2.8a**); however, composite membrane permeability also depends on ε of the support membrane skin layer. Ultimately, a thinner coating film requires a more porous support membrane skin layer. **Fig. 2.8b** indicates that for a fixed Δx, support membrane skin layer ε must increase as r_1 increases.

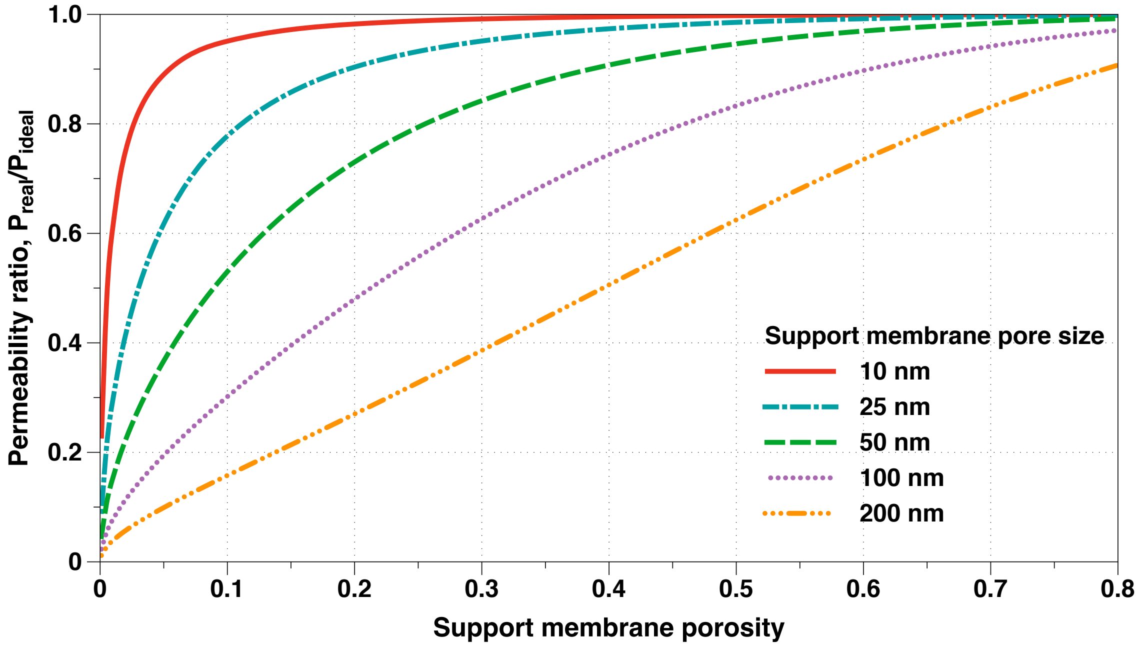

(a)

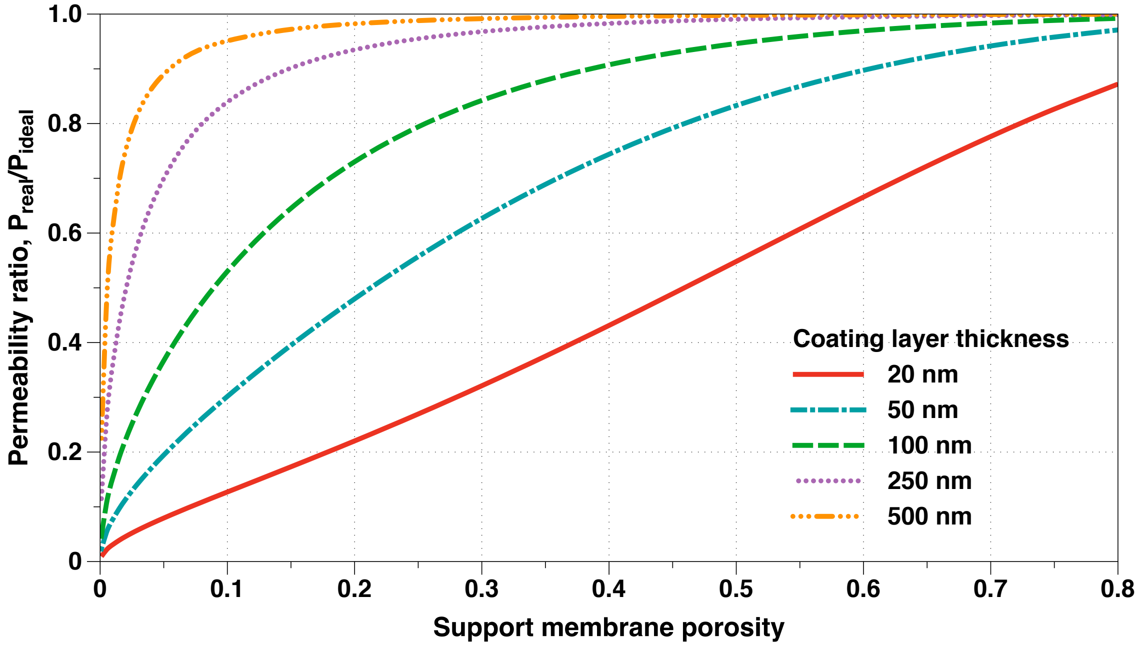

(b)

Figure 2.8. Permeability ratio as a function of the porosity for (a) a fixed support membrane pore size (r_1 = 50 nm) and a (b) fixed coating layer thickness (Δx = 100 nm).

The effect of support membrane skin layer porosity and r_1 on membrane water flux and observed salt rejection is shown in **Fig. 2.9**. As indicated in **Fig. 2.9(a)**, for a fixed Δx, water flux increases as support membrane skin layer porosity increases and as skin layer pore size decreases. For a fixed coating film structure, the maximum water flux is most easily achieved by decreasing pore size and increasing porosity. **Fig. 2.9(b)** suggests, for a fixed Δx, salt rejection increases as support membrane skin layer ε decreases and as r_1 increases. It is also important to point out that for a fixed membrane coating film structure, a minimum salt rejection is fixed (determined by coating film selectivity), but the maximum salt rejection is achieved by decreasing support membrane skin layer porosity and increasing the pore size of the support membrane.

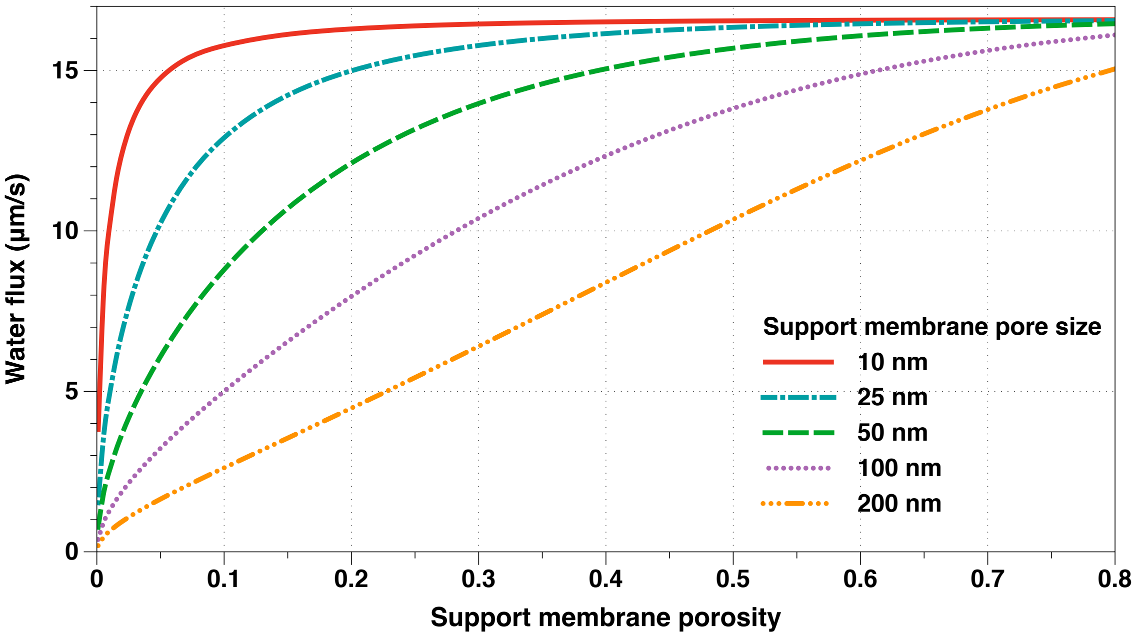

(a)

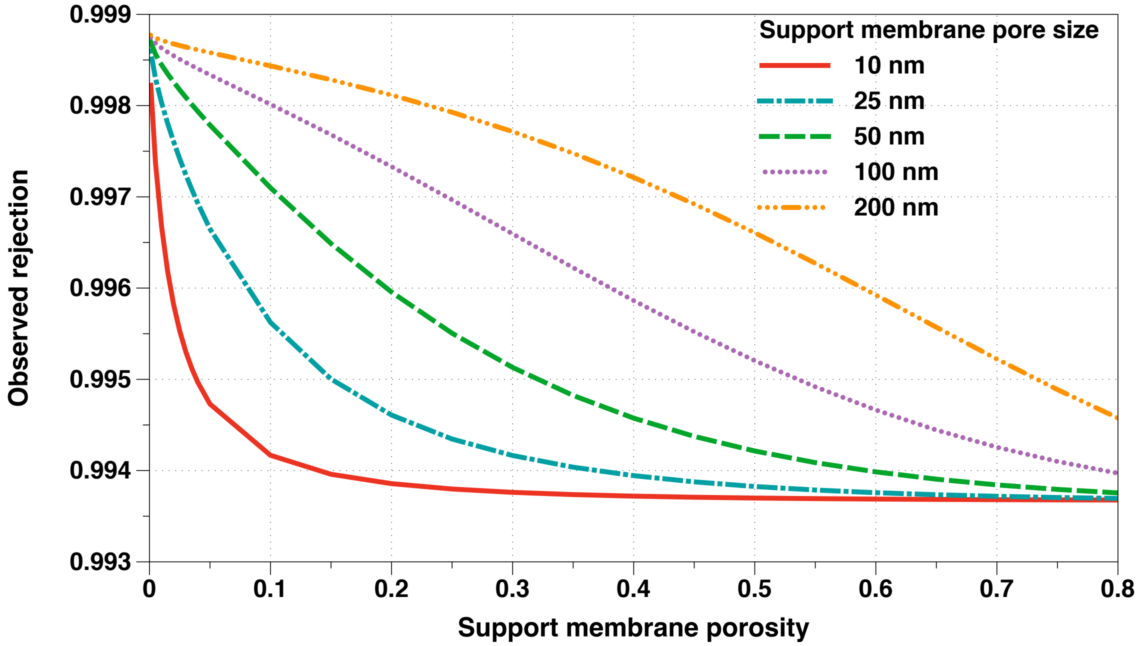

(b)

Figure 2.9. (a) Membrane water flux and (b) observed rejection shown as a function of support membrane porosity and pore size. Calculations made using transport coefficients characteristic of SWRO membrane (Δp = 55 bar, C_f = 32g/L, A = 4×10^{-12} m/Pa.s, B = 2×10^{-8} m/s, T = 298 K, k_f = 1×10^{-5} m/s).

Lonsdale *et al.* [140] experimentally demonstrate differences in water permeability of cellulosic composite membranes by tailoring the pore structure of the support membrane. When the distance between the pores is comparable to the thickness of the thin film, significant decline in water permeability is observed. Ramon *et al.* [9, 141] theoretically investigate the effect of support membrane pore size and porosity on diffusive transport through composite membranes. Based on their study, support membranes with high porosity and small skin layer pores result in high water and salt permeability because the effective diffusive path length for water and salt is shorter. They also find that a water flux distribution exists for composite membranes governed by the interplay between the active layer thickness and support membrane pore structure.

2.5. Solute Mass Transfer Limitations

2.5.1. External concentration polarization

In a NF or RO process, one of the main hindrances to transport through the membrane is the phenomenon known as external concentration polarization (ECP) (**Fig. 2.10**). Water and solutes are transported towards the membrane by permeate convection; water permeates, while rejected solutes can either diffuse through the membrane or back away from the membrane through the hydrodynamic boundary layer into the bulk of the feed. A buildup of rejected solutes occurs at the membrane surface, and hence, ECP increases the feed side salt concentration right at the membrane-feed solution interface, which influences both salt passage and trans-membrane osmotic pressure. With high salinity waters and significant ECP, sparingly soluble salts and organics may exceed their solubility limit and precipitate on the membrane leading to even higher hydraulic pressure requirement for permeation. Furthermore, ECP effects solute rejection. Recall that the real solute rejection (R_r) of a membrane is an intrinsic property of a membrane (**Eqn. 2.5**), whereas the observed rejection (R_o) will be much lower with significant ECP (**Eqn. 2.4**). Fortunately, the detrimental effects of ECP can be reduced by increasing cross-flow velocity to sweep solute molecules flowing parallel to the membrane downstream in the filtration channel and decrease the concentration near the surface of the membrane.

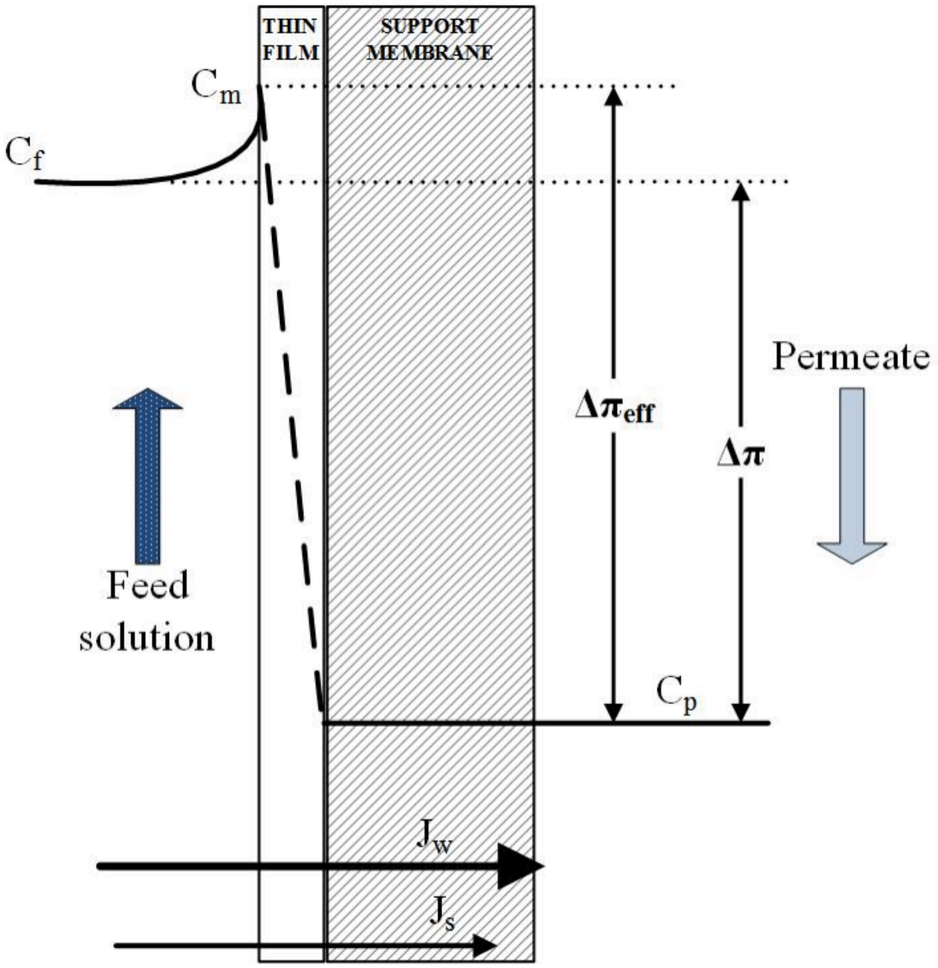

Figure 2.10. Schematic depicting external concentration polarization (ECP) buildup of salt on membrane surface during operation in NF or RO [141].

The ECP can be related to mass transfer by looking at solute rejection. To relate the C_m to C_f we define a parameter called the concentration polarization modulus or the CP modulus,

$$CP = \frac{C_m}{C_f} = \left(1 - R_r\right) + R_r \, exp\left(\frac{J_w}{k_f}\right) \tag{2.35}$$

When k_f increases, which can be achieved by increasing the cross-flow rate across the membrane surface, C_m will decrease and thereby decrease the effect of ECP. Many correlations have been derived to determine k_f either by computational efforts or by experimental results and are available in many handbooks. Several examples of correlations under various flow geometries are given in **Table 2.1**.

Table 2.1 Selected Mass Transfer Coefficient Correlations for Different Flow Geometries

Flow Geometry	Laminar Regime (Re < 2000)	Turbulent Regime (Re > 2000)	Ref.
Thin Rectangular channels without spacers	$\mathrm{Sh} = 1.85\left(\mathrm{ReSc}\frac{d_H}{L}\right)^{0.33}$	$\mathrm{Sh} = 0.04\mathrm{Re}^{0.75}\mathrm{Sc}^{0.33}$	[142]
In a tube	$\mathrm{Sh} = 1.62\left(\mathrm{ReSc}\frac{d_H}{L}\right)^{0.33}$	$\mathrm{Sh} = 0.023\mathrm{Re}^{0.83}\mathrm{Sc}^{0.33}$	[143]
Radial cross flow system	$\mathrm{Sh} = 1.05\left(\mathrm{ReSc}\frac{h}{R_c}\right)^{0.38}$	$\mathrm{Sh} = 0.275\left(\mathrm{Re}^{1.75}\mathrm{Sc}\frac{2H}{L}\right)^{0.33}$	[144-146]
Stirred Cell	$\mathrm{Sh} = 0.23\mathrm{Re}^{0.567}\mathrm{Sc}^{0.33}$	$\mathrm{Sh} = 0.03\mathrm{Re}^{0.66}\mathrm{Sc}^{0.33}\mathrm{Pe}_{test}^{0.16}$	[144, 147, 148]
Rectangular channels with spacers	$\mathrm{Sh} = 0.46\left(\mathrm{ReSc}\right)^{0.36}$	$\mathrm{Sh} = 0.0096\mathrm{Re}^{0.5}\mathrm{Sc}^{0.6}$	[149, 150]

[*] Where Sh (= $k_f d_H/D$) is the dimensionless Sherwood number that represents the ratio of convective to diffusive mass transport. The Reynolds number (Re = $u_0 d_H \rho/\eta$) represents the ratio of inertial to viscous forces for given flow conditions. The Schmidt number (Sc = $\eta/\rho D$) represents the ratio of contributions of viscosity to mass diffusivity. The Péclet number (Pe) represents the ratio of advective to diffusive transport. $\mathrm{Pe}_{\mathrm{test}}$ is the test Péclet number (= $J_w h/D$) that accounts for deviations from non-porous conduits in the system. Additionally, d_H is the hydraulic diameter calculated by (= $2wh/(w+h)$), w is the width of the channel, h is the height of the channel, L is length of channel, R_c is the radius of the flow channel, r_c is the radius of the stirred cell, u_0 is the cross-flow velocity, η is the dynamic viscosity of the solution, ρ is the density of the solution, and D is the diffusion coefficient of the solute in water.

Based on the van `t Hoff equation, the effective osmotic pressure difference ($\Delta\pi_{eff}$) across the membrane for can be calculated as

$$\Delta\pi_{eff} = nC_f R_g T R_r \exp\left(\frac{J_w}{k_f}\right) \tag{2.36}$$

where n is the sum of the charges of the cations and anions in the electrolyte. For example, in a 1:1 electrolyte, such as sodium chloride, $n = 2$. The equation above is only valid for dilute solutions where the mole fraction of water, x_w, is approximately unity. Otherwise, the osmotic pressure (π) is more accurately defined by the Gibbs' equation [151],

$$\pi = -\frac{R_g T}{V_w} \ln x_w \tag{2.37}$$

Most NF and RO membrane surfaces have charged functional groups, which causes solute rejection and in effect, concentration polarization, to change in response to feed solution pH. A study from Childress *et al.* [152] found that polyamide NF membranes with amphoteric surfaces are positively charged below its isoelectric point (pH ~ 5) due to protonation of the amino groups and negatively charged above its isoelectric point due to deprotonation of the carboxyl groups. It was also found that at the membrane isoelectric point, water flux and NaCl rejection were maximal due to decreased electrostatic repulsion and increased pore size. Bellona *et al.* studied the rejection of organic compounds by NF membranes with negative surface charge at neutral solution pH. The rejection of negatively charged organic acids increased with feed water pH (below pK_a) due to an increase in the negative surface charge of the membrane resulting in higher electrostatic repulsion before reaching a plateau in rejection [153]. This plateau is attributed to a trade-off between membrane pore expansion and swelling as a result of functional group deprotonation and increase in rejection from solute deprotonation. A similar study was done by Verliefde *et al.* in which they concluded that neutral and positively charged organic solutes can approach negatively charged NF membrane surfaces close enough to establish hydrophobic interactions [154]. This causes a buildup of neutral and positively charged solutes near the membrane surface, or external concentration polarization. The researchers further attributed the lower rejection of acidic pharmaceuticals by NF membranes to the hydrophobic interactions that help the solutes partition into the membrane. **Fig. 2.11** depicts that at neutral solution pH, RO and NF membrane surfaces typically exhibit negative surface charge, which causes a rejection of negatively charged solutes and an interaction of neutral and positively charged solutes. These electrokinetic characteristics play an important role in how the membrane rejects charged solutes and causes a concentration polarization at the membrane surface, especially with varying solution pH.

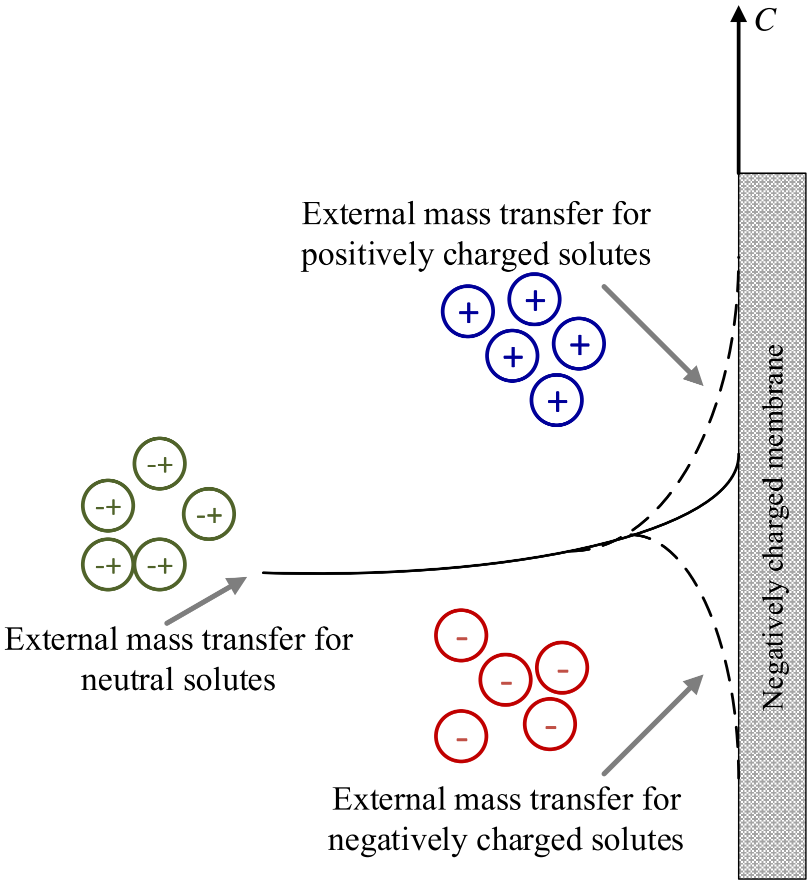

Figure 2.11. Conceptual illustration depicting the difference in external mass transfer between positively charged, negatively charged and neutral solutes.

2.5.2. Internal concentration polarization

The phenomenon of internal concentration polarization is based on the concept of hindered diffusion, which describes solute particles accumulating in a layer of the membrane (*e.g.* Support layer, fouling layer *etc.*). Several factors contribute to the accumulation of solute particles in the membrane layer, including the tortuosity, porosity, and thickness, which consequently hinders the diffusion of solute from the membrane layer.

A simple analytical expression for estimating the dependence of the hindered diffusion coefficient (D^*) on porosity in the membrane layer is given by

$$D^* = \frac{\varepsilon}{\tau} D \tag{2.38}$$

where D is the solute diffusivity in the bulk, e is the membrane porosity, and t ($\approx 1 - \ln e^2$) is the diffusive tortuosity [155]. Recent investigations have shown that fouling or “cake” layer porosities for silica colloids filtered under similar physical and chemical conditions were in the range of 0.3 to 0.7 [156-158]. The ratio of the effective diffusion coefficient to the bulk diffusion coefficient is plotted against cake layer porosity in **Fig. 2.12**. Over the range of typical porosity values the effective diffusion coefficient may be reduced to between 10 and 40 percent of the bulk diffusion coefficient, which results in significantly enhanced salt concentration at the membrane surface.

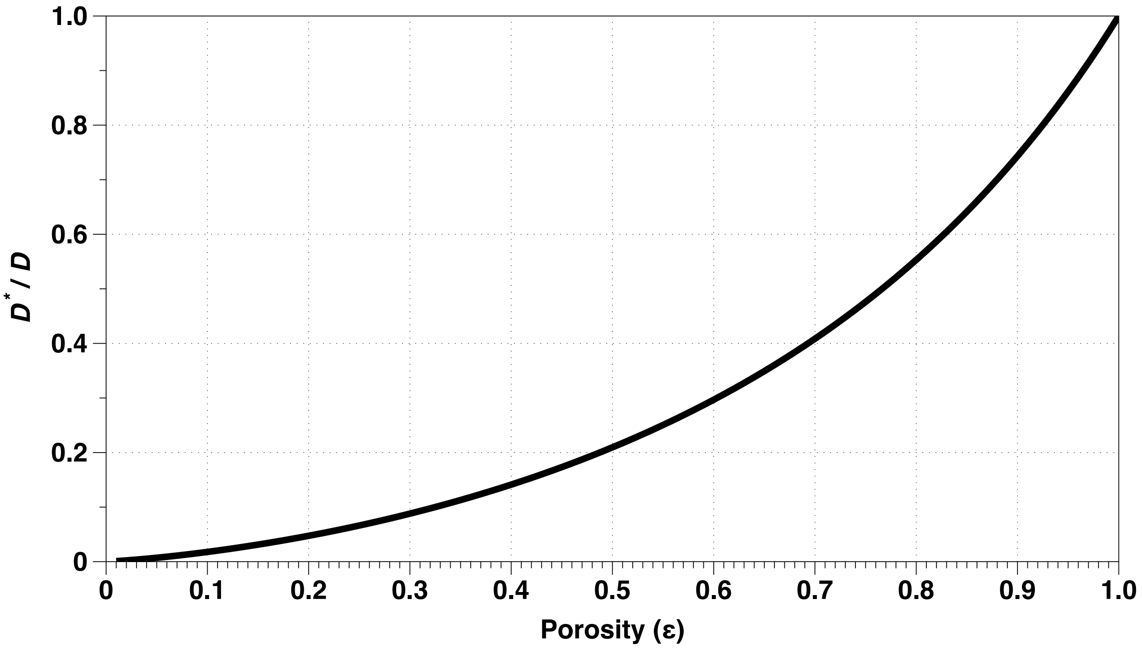

Figure 2.12. Hindered Diffusion as a function of membrane support layer porosity.

In FO processes, the transport of water naturally occurs due to a difference in solute concentration across the membrane, which changes the thermodynamic activity of water. Due to minimal hydraulic pressure, hindered diffusion causes accumulation of solute in the support layer of the membrane, a phenomenon called internal concentration polarization (ICP). When the dense layer of the membrane faces the high concentration draw solution (PRO-mode), concentrative ICP occurs where the solute from the feed solution becomes concentrated in the porous support membrane due to hindered diffusion, decreasing the effective osmotic pressure across the membrane (**Fig. 2.13a**). When the dense layer of the membrane faces the dilute feed solution (FO-mode), dilutive ICP occurs as the draw solution concentration is diminished by the incoming water flux across the membrane (**Fig. 2.13b**). In both cases there is a substantial reduction in the effective osmotic pressure difference, which is the driving force for water flux in FO [159].

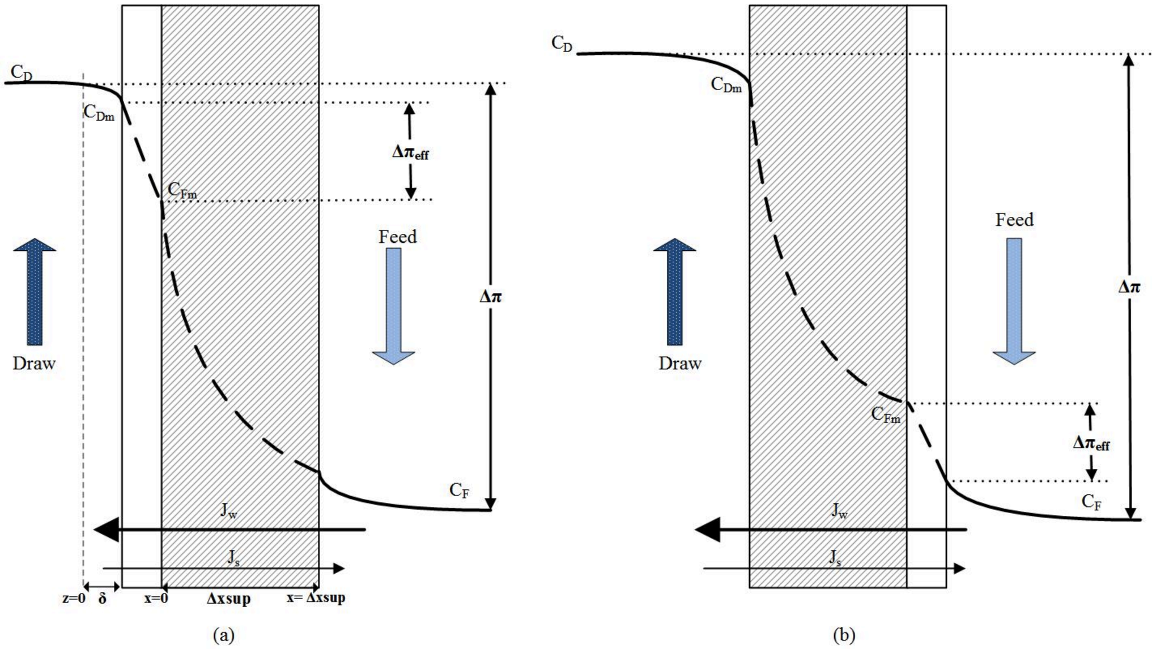

Figure 2.13. Schematic showing the concentration profile through an asymmetric membrane, illustrating the reduction in the osmotic pressure difference due to (a) concentrative ICP in PRO-mode and (b) dilutive ICP in FO-mode [141, 160].

The water flux, J_w, is determined using a similar equation as in RO, except in the case of FO, the osmotic pressure, $\Delta\pi_{eff}$, is the dominant driving force for transport,

$$J_w = A\left(\Delta\pi_{eff} - \Delta p\right) \tag{2.39}$$

Similarly, the salt flux across the active layer, J_s^a, is determined using the solute concentration at the membrane surface, after accounting for ECP and ICP [160],

$$J_s^a = B\left(C_{Dm} - C_{Fm}\right) \tag{2.40}$$

The concentration at the membrane surface is not a measureable quantity, but it can be related to salt flux across the support membrane,

$$J_s^s = -D^s \frac{dC(x)}{dx} - J_w C(x) \tag{2.41}$$

where D^s is the diffusivity of the solute in the porous support layer of the composite membrane. At steady-state conditions, the J_s^s must be equal to J_s^a on the basis of mass continuity,

$$-D^s \frac{dC(x)}{dx} - J_w C(x) = B\left(C_{Dm} - C_{Fm}\right) \tag{2.42}$$

By integrating across the support membrane using the boundary conditions, assuming ICP dominates and ECP is negligible,

$$C(0) = C_{Fm} \text{ at } x = 0$$

$$C(\Delta x_{sup}) = C_F \text{ at } x = \Delta x_{sup},$$

an expression for C_{Fm} can be derived. Using a similar process, an expression for C_{Dm} is also derived by recognizing that at steady-state, J_s^a must equal the salt flux through the boundary layer near the membrane, which is also described with convective and diffusive components,

$$J_s^{BL} = D\frac{dC(z)}{dz} - J_w C(z) \tag{2.43}$$

and the boundary conditions

$$C(0) = C_{Db} \text{ at } z = 0$$

$$C(\delta) = C_{Dm} \text{ at } z = \delta.$$

Assuming the van `t Hoff equation applies and osmotic pressure is proportional to the solution concentration, the expressions for C_{Fm} and C_{Dm} are substituted into **Eqn. 2.43** for J_w to obtain an equation that depends only on measureable quantities [160, 161],

$$J_w = A\left[\frac{\pi_D \exp\left(\frac{-J_w}{k_f}\right) - \pi_F \exp\left(J_w K\right)}{1+\frac{B}{J_w}\left[\exp\left(J_w K\right) - \exp\left(\frac{-J_w}{k_f}\right)\right]} - \Delta p\right] \tag{2.44}$$

Similarly, for the salt flux in the active layer,

$$J_s^a = B\left[\frac{\pi_D \exp\left(\frac{-J_w}{k}\right) - \pi_F \exp\left(J_w K\right)}{1+\frac{B}{J_w}\left[\exp\left(J_w K\right) - \exp\left(\frac{-J_w}{k}\right)\right]}\right] \tag{2.45}$$

where K is a parameter to quantify the extent of ICP called resistance to solute diffusion by the porous substructure, which depends on the orientation of the membrane. For PRO-mode and deionized water as the feed solution ($\pi_F = 0$) [161, 162]

$$K = \left(\frac{1}{J_w}\right) ln\left(\frac{B + A\pi_D - J_w}{B + A\pi_F}\right) \tag{2.46}$$

For FO-mode

$$K = \left(\frac{1}{J_w}\right) ln\left(\frac{B + A\pi_D}{B + A\pi_F + J_w}\right) \tag{2.47}$$

where π_D and π_F are the osmotic pressures of the draw and feed solutions, respectively. To characterize the porous support, it is necessary to uncouple the solute resistance from the draw solution by defining a membrane structural parameter, S, as

$$S = KD = \frac{\Delta x_{eff}\tau}{\varepsilon} \tag{2.48}$$

where Δx_{sup}, τ, and ε are the support membrane thickness, tortuosity, and porosity, respectively [160].

Fig. 2.14 shows a plot of water flux as a function of either water permeability (*A*), salt permeability (*B*) or resistance to solute diffusion (*K*) as presented by **Eqn. 2.44** using experimental data obtained for commercial CTA membrane [141]. When deriving this plot, it is assumed that when parameter *A* is changing, for example, both parameter *B* and *K* are held constant. **Fig. 2.14** shows that as *A* increases, the water flux increases, which is as expected since more water is allowed to permeated through the membrane. However, as *B* or *K* increases, the water flux decreases. As the salt permeability increases, more salt is allowed to diffuse into the support layer, exacerbating ICP, and thereby decreasing the driving force for water flux across the membrane. As *K* increases, the solute in the support layer has difficulty in diffusing out, which again decreases the effective osmotic pressure and the water flux across the membrane. The plot shows that water flux is more sensitive to changes with *A* than with *B* and *K* for the values chosen. This may be because *A* directly affects the water flux, while parameters *B* and *K* affects solute flux, which affects the osmotic pressure and indirectly affects the water flux.

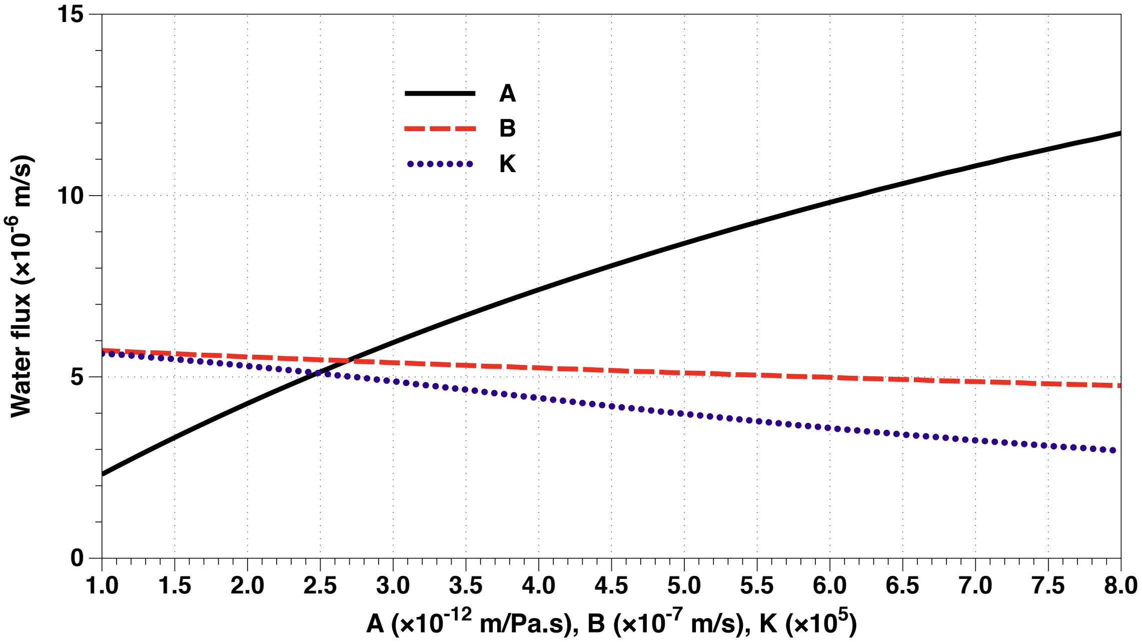

Figure 2.14. Effect of water permeability, salt permeability and resistance to solution diffusion coefficient on FO water flux for a CTA membrane using 32g/L NaCl as draw and deionized water as feed solution.

The water and salt permeability (*A* and *B*) used in calculating *K* and, subsequently, *S* are determined by RO experiments, with the membrane under hydraulic pressure, and do not reflect the accurate transport conditions in FO operation. Recently, Tiraferri *et al.* developed a protocol to determine the transport and structural parameters of FO membranes by conducting only FO experiments. Through a set of experiments of increasing draw solution concentration to determine the water and salt flux and by minimizing the coefficient of variation of the ratio of J_w to J_s, the authors determine *A*, *B,* and *S* without conducting any RO experiments [163].

According to **Eqn. 2.48**, the lowest hindrance to diffusion, or the lowest amount of ICP, is achieved when the FO support membrane is thin, non-tortuous, hydrophilic, and has high porosity [164]. Although thin support membranes may be ideal, FO membranes must still be mechanically robust enough to withstand backwashes in operation and ease in handling. According to a recent study by Widjojo *et al.*, the most permeable and selective FO membranes were formed from a composite membrane of a 50% sulphonated polyethersulfone UF membrane with a dense selective polyamide film formed on top [171]. The composite membrane had a spongy morphology, but had the highest flux and lowest salt passage (using deionized water as the feed solution and 2M NaCl as the draw solution) compared to others reported in literature. The authors conclude that the hydrophilicity of the support membrane has a greater impact on water permeability than the morphology [164]. This highlights that hydrophilicity, or the chemistry of the support membrane, is not incorporated in the membrane structural parameter. Furthermore, Wong *et al.* found that by changing the solution temperature, concentration, and salt composition S can change significantly when testing a commercial cellulose triacetate FO membrane [141]. This reiterates the fact that the solution chemistry affects the structure of the membrane and determines the transport of solutes, which may not be accurately reflected in the structural parameter, probing further consideration and investigation.

2.5.3. Fouling-enhanced external concentration polarization

Membrane fouling in NF/RO applications is another example of hindered diffusion as colloidal deposits also provide the tortuous path that aids in accumulation of solute particles as the support layer in FO membranes. Contrary to FO/PRO operation, in

NF/RO, water flux and salt flux are in the same direction, which offers a more simplified model construction. A fouling layer in NF/RO processes will enhance ECP by a combination of hindered back-diffusion of salt ions and averted cross-flow hydrodynamics within the fouling layer (**Fig. 2.15**). With no particles deposited on the membrane surface, the solute concentration profile quickly reaches steady-state, where solute transport by convection towards the membrane is balanced by solute back-transport from the polarized layer near the membrane surface by diffusion (**Fig. 2.15a**). As colloidal particles accumulate and form a thin cake layer over the surface of the membrane the diffusion of salt ions back into the bulk is hindered because of the tortuous path the ions must travel through in the deposited layer (**Fig. 2.15b**) [165]. Hindered back-diffusion of salt ions trapped in the cake layer leads to an enhanced membrane surface salt concentration (C_m^*) and, thus, enhanced osmotic pressure drop across the membrane ($\mathrm{D}p_{eff}^{*}$).

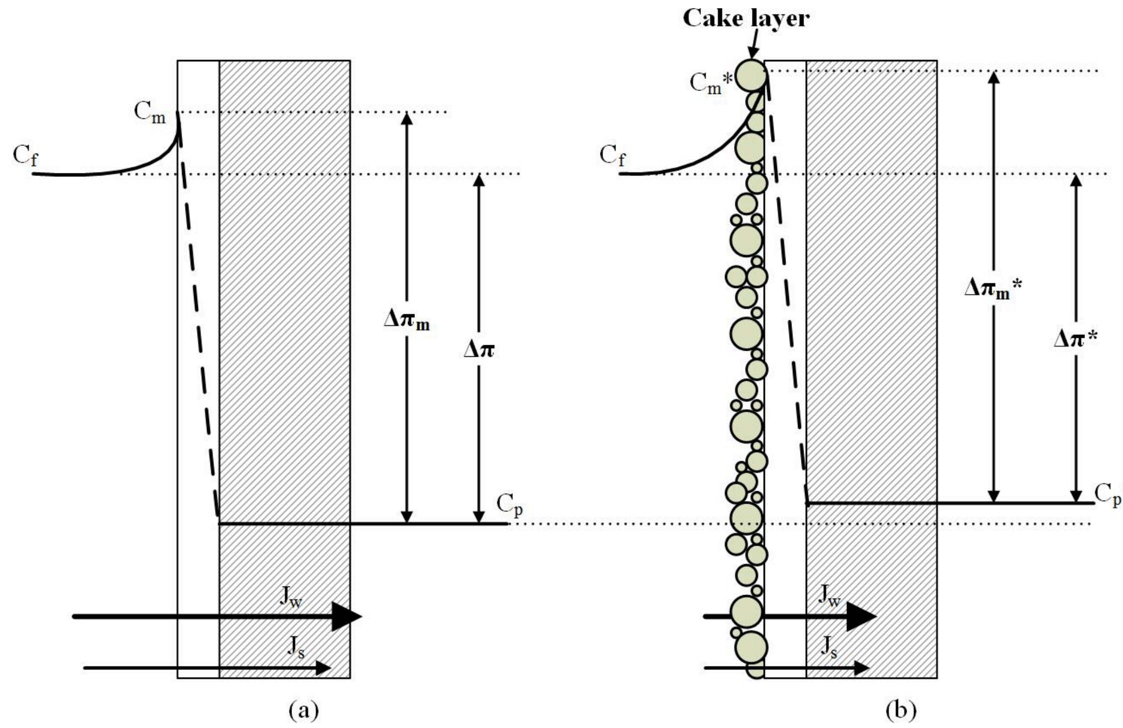

Figure 2.15. Schematic depicting ECP concentration profiles during (a) steady-state and (b) cake layer formation, causing cake-enhanced osmotic pressure.

To describe the transient membrane flux through a fouling layer, the flux is defined as

$$J(t) = \frac{\Delta p}{R_m + R_c(t)} \qquad (2.49)$$

In the standard cake filtration model, flux decline (or decline in trans-membrane pressure) is assumed to arise solely from the added hydraulic resistance of the cake layer. However, it was previously demonstrated that this is an unreasonable assumption for salt rejecting membranes because the primary mechanism of the flux decline is a transient, cake-enhanced osmotic pressure [165, 166]. The cake-enhanced osmotic pressure model begins by rearranging the cake filtration equation into a series of pressure drops

$$\Delta p_m(t) = \Delta p - \Delta\pi^*_{eff}(t) - \Delta p_c(t) \tag{2.50}$$

where the cake-enhanced osmotic pressure is described by,

$$\Delta\pi^*_{eff}(t) = \Delta p - J(t)R_m - J(t)R_c \tag{2.51}$$

$$R_c(t) = \left[\frac{45\eta(1-\varepsilon_c)}{\rho_p a_p^2 \varepsilon_c^3}\right] M_d(t) \tag{2.52}$$

where ε_c is the cake layer porosity, a_p is the particle radius, ρ_p is the particle density and M_d is transient deposit layer mass per unit membrane area, R_m is membrane resistance and R_c is cake layer resistance. The transient driving force for permeation, the trans-membrane pressure ($\Delta p_m = J(\mathrm{t})R_m$), is a function of the constant applied pressure (Δp), the transient cake-enhanced osmotic pressure (Δp_{eff}^*), and the transient trans-cake hydraulic pressure ($\Delta p_{\mathrm{c}} = J(\mathrm{t})R_c$).

The mathematical model that follows is based on three important assumptions. First, the cake layer is thin compared to the salt film-layer thickness. Past investigations have shown that the tangential flow field is relatively unaffected when the cake layer is thin with respect to the channel height [157] because the cake layer does not occupy a significant fraction of the channel cross section [167]. Cross-flow shear rate is relatively unaffected by the presence of the cake layer, and thus the CP layer thickness remains at the film thickness determined prior to particle deposition. Second, the colloid deposit layer does not reject salt ions, so the profile of salt concentration above the colloid deposit layer is unchanged from that prior to cake formation. Third, the effective diffusion coefficient for salt ions trapped within the colloid deposit layer can be estimated with knowledge of the cake layer porosity.

From the previous section, it was described that $D^* = (\varepsilon/\tau)\ D$. Next, the effective mass transfer coefficient is broken down into two parts – one describing mass transfer through the colloid deposit layer and one describing mass transfer from the interface of the colloid layer back into the bulk. The resulting "hindered" mass transfer coefficient (k^*) is estimated from

$$\frac{1}{k^*} = \frac{\delta_c}{D^*} + \frac{\delta_s}{D} \tag{2.53}$$

where δ_c is the colloid deposit layer thickness and δ_s is the difference between the film (δ_f) and cake layer thicknesses. **Eqn. 2.53** comes directly from integrating **Eqn. 2.43** separately across the cake and CP layers. Even if the cake layer is very thin ($\delta_c << \delta_s$) the cake-enhanced osmotic pressure may be significant because the hindered diffusion coefficient can be an order of magnitude smaller than the bulk diffusion coefficient.

Note that the cake layer thickness can be written in terms of cake mass per unit membrane area as $\delta_c = M_d / r_p(1-\varepsilon)$ [157]. Rewriting **Eqn. 2.53**, the hindered mass transfer coefficient expression, in terms of δ_f and δ_c and substituting into **Eqn. 2.36**, results in the following expression for the cake-enhanced osmotic pressure:

$$\Delta\pi^*_{eff}\left(t\right) = 2C_f R_g T R_o \exp\left[\frac{J\left(t\right)}{k_f} + \frac{J\left(t\right) M_d\left(t\right)}{\rho_p(1-\varepsilon_c)}\left(\frac{1-\ln(\varepsilon_c^2)}{D\varepsilon_c} - \frac{1}{D}\right)\right] \tag{2.54}$$

All parameters in this equation are constant or experimentally measurable, except cake porosity (ε_c) and cake-enhanced osmotic pressure (Δp_{eff}^*). Setting **Eqn. 2.54** equal to

Eqn. 2.51 allows direct calculation of the cake layer porosity, and thus, cake-enhanced osmotic pressure.

Using the models described above, the effects of membrane fouling are demonstrated for a high flux RO membrane (A = 9.0×10^{-12} m/s-Pa, B = 6.0×10^{-8} m/s) using different sized colloidal particles under constant flux (**Figs. 2.16-2.17**) and constant pressure (**Figs. 2.18-2.19)** operations. Under constant pressure operation, the cake layer growth of particles with any size will cause membrane flux and rejection decline and CP modulus increase (**Fig. 2.16**) due to increasing cake enhanced osmotic pressure and trans-cake layer pressure. However, the 5 nm particle causes more flux and rejection decline than the 80 nm particle after 10 days of operation, although it produced thinner cake layer and CP modulus. This is due to the ability for smaller particles to pack into a tighter layer with higher hydraulic resistance, thereby significantly enhancing the pressure drop in the cake layer and reducing the trans-membrane pressure (water flux) at constant applied pressure (**Fig. 2.17**).

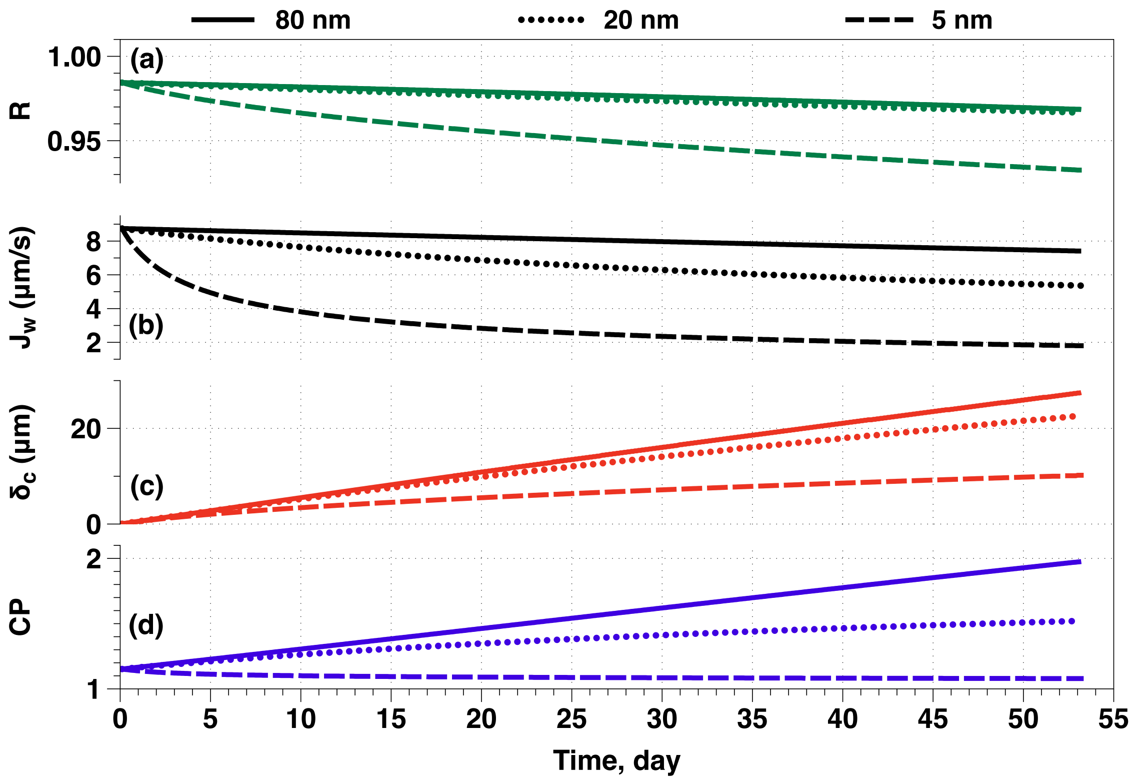

Figure 2.16. (a) Membrane flux, (b) cake layer thickness and (c) CP modulus for a high flux RO membrane fouled by particles with different size under constant applied pressure operation (Δp = 5.7 bar, $D_s = 1.6\times10^{-9}$ m^2/s, ε_c = 0.46, $k_f = 6.1\times10^{-5}$ m/s, C_f = 1.0 g/L)

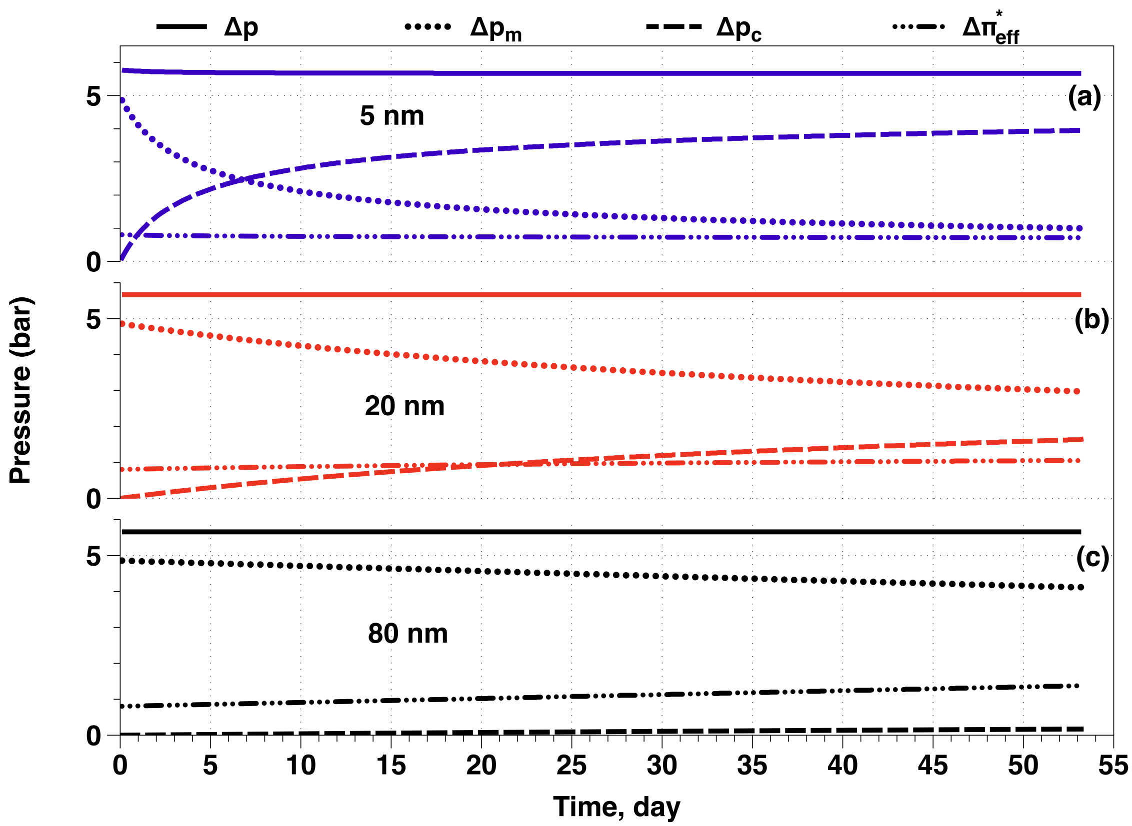

Figure 2.17. Pressure drop and cake-enhanced osmotic pressure for membranes fouled by (a) 5 nm, (b) 20 nm and (c) 80 nm particles under constant applied pressure operation (Δp = 5.7 bar, $D_s = 1.6\times10^{-9}$ m^2/s, ε_c = 0.46, $k_f = 6.1\times10^{-5}$ m/s, C_f = 1.0 g/L)

At constant flux operation, membrane rejection, water flux, cake layer thickness and CP modulus are independent with fouling particle size (**Fig. 2.18**). As cake layer continuing to growth, membrane rejection decreases and CP modulus increases. Applied pressure increases with increasing cake enhanced osmotic pressure and trans-cake layer pressure. However, 5nm particle causes the applied pressure to increase dramatically compared to the 80nm particle due to increasing trans-cake layer pressure caused by increased packing of smaller particles (**Fig. 2.19**).

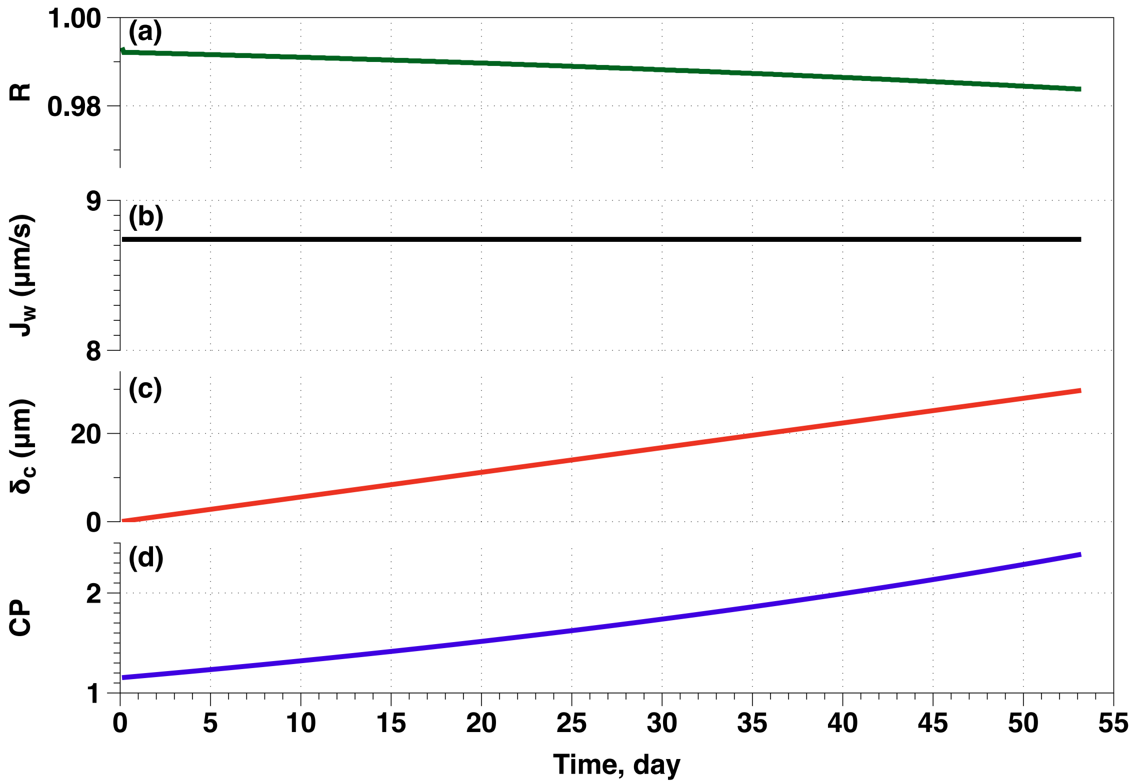

Figure 2.18. (a) Membrane flux, (b) cake layer thickness and (c) CP modulus for a high flux RO membrane fouled by particles with different size under constant flux operation ($J = 8.7\times10^{-6}$ m/s, $D_s = 1.6\times10^{-9}$ m^2/s, $\varepsilon_c = 0.46$, $k_f = 6.1\times10^{-5}$ m/s, $C_f = 1.0$ g/L)

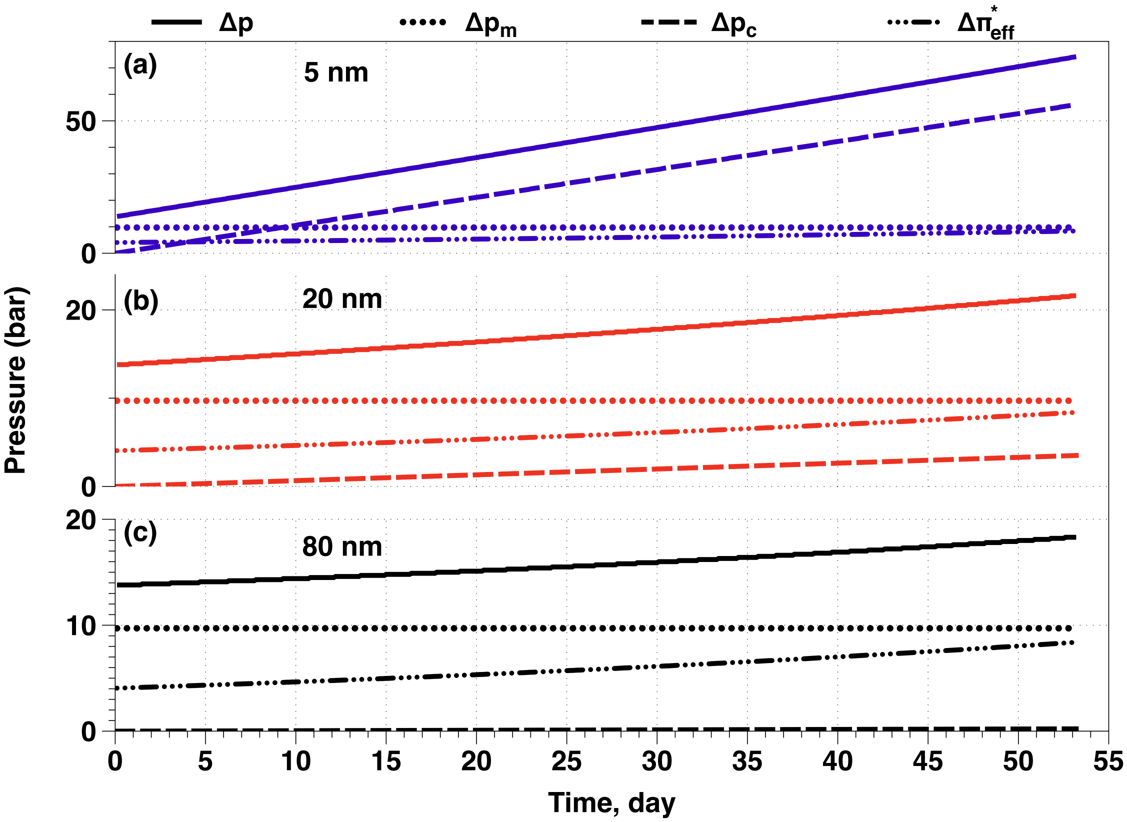

Figure 2.19. Pressure drop and cake-enhanced osmotic pressure for membranes fouled by (a) 5 nm, (b) 20 nm and (c) 80 nm particles under constant applied pressure operation ($J = 8.7\times10^{-6}$ m/s, $D_s = 1.6\times10^{-9}$ m^2/s, $\varepsilon_c = 0.46$, $k_f = 6.1\times10^{-5}$ m/s, $C_f = 1.0$ g/L)

2.6. Conclusions

An impressive amount of work has been done to model solvent and solute transport in osmotic membranes. Phenomenological models based on thermodynamics and mechanistic models based on structure-performance relationships have been proposed and applied widely. Advanced structural characterization techniques provide the ability to measure pore size, porosity, pore length, and tortuosity of both the thin active layer and support structure in osmotic membranes. These membrane structural characteristics should be included in transport models to help mechanistically explain membrane transport and to enable predictions of membrane performance. Transport models can also be used to design “ideal” membranes for targeted applications.

In addition to modeling transport in the membrane active layer, as is typically done, a close look at the support membrane structure is necessary. State-of-the-art osmotic membranes are primarily thin film composite membranes. Support membrane structure needs to be incorporated into composite membrane transport models since skin layer pore size and porosity significantly impact composite membrane permeability and rejection, as shown in modeling studies. Mixed matrix membrane transport models may also be relevant to describe transport through thin film nanocomposite NF, RO, and FO membranes. For example, the impact of filler concentration on composite membrane permeability can be calculated from mixed matrix models to offer insight into nanocomposite membrane design.

Solute gradients across the entire membrane thickness must also be considered. During separation processes solute concentrations may build up at the membrane surface or diminish in the support membrane having serious impacts on overall transport. Both external (ECP) and internal concentration polarization (ICP) play crucial roles in membrane transport. ECP not only raises energy consumption in osmotic membrane processes by increasing osmotic pressure differences across the membrane that need to be overcome, but it also reduces observed membrane rejection. ICP reduces the driving force in FO processes, thereby reducing the process productivity. Understanding and modeling concentration polarization is critical for membrane applications. Operation conditions, such as flux and cross-flow rate, can be optimized to minimize ECP based on

ECP models. To minimize ICP, the support membrane structure model is a powerful tool to design "ideal" support membrane structure.

The pore-flow model, based on size exclusion, incorporates membrane pore size into model equations; however, no other pore structural characteristics (*e.g.*, pore shape, tortuosity) are accounted for. The solution-diffusion model, which assumes thermodynamic equilibrium exists at the membrane interface and both solvent and solute transport through the membrane are driven by chemical potential gradients, has been successfully employed due to its straightforward format. There is no structural information included in the solution-diffusion model and both pore structure and membrane-solute/solvent energetic interactions are excluded. Although Kedem-Katchalsky and Spiegler-Kedem models can be used to describe solute transport of NF and RO membranes, these models treat the membrane as a "black box" and provide no information on the transport mechanism. On the other hand, both the modified solution-diffusion and modified solution-diffusion-convection models provide insight into structure-performance relationships in osmotic membrane transport. Such models will be beneficial in allowing for fine-tuning of future materials for specific separation applications.

The major drawback of all of these models is that they do not consider interactions with charged solutes. Electrokinetic models, such as the extended Nernst-Planck model, provide complete descriptions of ionic species transport through membranes, but these models are impractical for salt mixtures. Future work should seek a combined solution-diffusion, convection, and electro-migration transport model incorporating membrane structural characteristics and solute/solvent membrane interactions should be investigated for both normal and mixed matrix osmotic membranes. The extension of such a unified model to multi-component mixtures should also be explored. For thin film composite membranes, the effects of both support membrane structure and chemistry (*e.g.*, hydrophilicity) on composite membrane transport should be evaluated.

2.7 List of Symbols

a	activity
A	solvent permeability
A_s	contact area between solute molecule and membrane
A_w	contact area between water molecule and membrane
B	solute permeability
c	concentration within membrane
C_D	FO draw solution concentration
C_f	concentration of feed solution
C_F	FO feed solution concentration
C_m	concentration at membrane surface
C_p	permeate solute concentration
CP	concentration polarization modulus
D	diffusion coefficient
D^*	hindered diffusion coefficient
d_H	hydraulic diameter
d_p	deposit particle diameter
F	Faraday constant
h	feed channel height
J_s	solute flux
J_w	solvent flux
K	resistance to solute diffusion
k^*	hindered mass transfer coefficient
k_B	Boltzmann constant
K_c	convective hindrance factor
K_d	diffusive hindrance factor
k_f	mass transfer coefficient of feed channel
K_s	solute-membrane partition coefficient
K_w	solvent-membrane partition coefficient
L	feed channel length
M_∞	mass of membrane with maximum
M_0	initial mass of membrane
M_f	cake layer mass pre membrane unit area
n	sum of the charge of cations and anions in electrolyte
p	pressure
P_d	permeability of dispersed phase of composite membrane
P_{eff}	effective composite membrane permeability
$\mathrm{Pe}_{\mathrm{test}}$	test Peclet number
p_f	feed pressure
P_m	permeability of continuous phase of composite membrane
p_p	permeate pressure
r	radius
R_c	radius of the flow channel

r_c	radius of the stirred cell
Re	Reynolds number
R_f	fouling layer resistance
R_g	gas constant
R_m	membrane resistance
R_o	observed rejection
r_p	pore radius
R_r	real rejection
r_s	solute Stokes radius
r_w	water Stokes radius
S	structure factor
Sc	Schmidt number
Sh	Sherwood number
T	temperature
u_0	cross-flow velocity
V_i	molar volume of species i
W	solvation energy
w	feed channel width
x	axial coordinate
X	charge density
X_{sw}	friction constant between solute and water
x_w	mole fraction of water
z	number of charge
$\alpha(\rho)$	dimensionless solute velocity in the pore
β	concentration polarization factor
β_1	dimensionless solvent viscosity in the pore
γ^-	electron-donor surface tension component
γ^+	electron-acceptor surface tension component
γ^{LW}	Lifshitz-van der Waals surface tension component
δ	pore length
δ_c	colloid deposit layer thickness
ΔG_s	solute-membrane interaction energy
ΔG_w	solvent-membrane interaction energy
Δp	pressure drop across the membrane
δ_s	difference between film and cake layer thickness
Δx	membrane thickness
Δx_{sup}	support layer thickness
$\Delta\pi$	osmotic pressure difference across the membrane
$\Delta\pi_{eff}$	effective osmotic pressure difference across the membrane
$\Delta\pi_s$	osmotic pressure difference across the membrane during NaCl spike
ε	porosity
ε_c	cake layer porosity
ε_f	fouling layer porosity
η	solvent viscosity

θ_a	amorphous volume fraction
θ_d	volume fraction of dispersed fillers
λ	sieving factor
μ	chemical potential
π	osmotic pressure
ρ	radical position
ρ_p	deposit particle density
ρ_w	water density
σ	reflection coefficient
τ	tortuosity
ϕ_s	solute-membrane pore partition coefficient
ϕ_w	solvent-membrane pore partition coefficient
ψ	electrical potential

2.8. References

[1] K. Dworecki, A. Ślęzak, B. Ornal-Wąsik, S. Wąsik, Effect of hydrodynamic instabilities on solute transport in a membrane system, Journal of Membrane Science, 265 (2005) 94-100.

[2] S. Sobana, R.C. Panda, Identification, Modelling, and Control of Continuous Reverse Osmosis Desalination System: A Review, Separation Science and Technology, 46 (2011) 551-560.

[3] R.E. Kesting, The 4 Tiers of Structure in integrally skinned phase inversion membranes and their relevance to various separation regimes, Journal of Applied Polymer Science, 41 (1990) 2739-2752.

[4] M. Mulder, Basic Principles of Membrane Technology, in, Kluwer Academic Publishers, London, 1996.

[5] S. Loeb, S. Sourirajan, High Flow Semipermeable Membrane for separation of water from saline solutions, in, US, May 1964.

[6] M.T.M. Pendergast, J.M. Nygaard, A.K. Ghosh, E.M.V. Hoek, Using nanocomposite materials technology to understand and control reverse osmosis membrane compaction, Desalination, 261 (2010) 255-263.

[7] A.K. Ghosh, E.M.V. Hoek, Impacts of support membrane structure and chemistry on polyamide-polysulfone interfacial composite membranes, Journal of Membrane Science, 336 (2009) 140-148.

[8] M.M. Pendergast, E.M.V. Hoek, A review of water treatment membrane nanotechnologies, Energ Environ Sci, 4 (2011) 1946-1971.

[9] G.Z. Ramon, M.C.Y. Wong, E.M.V. Hoek, Transport through composite membrane, part 1: Is there an optimal support membrane?, Journal of Membrane Science, 415 (2012) 298-305.

[10] J.E. Cadotte, R.J. Petersen, R.E. Larson, E.E. Erickson, New Thin-Film Composite Seawater Reverse-Osmosis Membrane, Desalination, 32 (1980) 25-31.

[11] V. Freger, Nanoscale heterogeneity of polyamide membranes formed by interfacial polymerization, Langmuir, 19 (2003) 4791-4797.

[12] O. Coronell, B.J. Marinas, D.G. Cahill, Depth Heterogeneity of Fully Aromatic Polyamide Active Layers in Reverse Osmosis and Nanofiltration Membranes, Environ Sci Technol, 45 (2011) 4513-4520.

[13] V. Freger, S. Srebnik, Mathematical model of charge and density distributions in interfacial polymerization of thin films, Journal of Applied Polymer Science, 88 (2003) 1162-1169.

[14] W.R. Bowen, A.W. Mohammad, N. Hilal, Characterisation of nanofiltration membranes for predictive purposes - Use of salts, uncharged solutes and atomic force microscopy, Journal of Membrane Science, 126 (1997) 91-105.

[15] N. Hilal, H. Al-Zoubi, N.A. Darwish, A.W. Mohammad, Characterisation of nanofiltration membranes using atomic force microscopy, Desalination, 177 (2005) 187-199.

[16] K.L. Tung, Y.C. Jean, D. Nanda, K.R. Lee, W.S. Hung, C.H. Lo, J.Y. Lai, Characterization of multilayer nanofiltration membranes using positron annihilation spectroscopy, Journal of Membrane Science, 343 (2009) 147-156.

[17] K. Boussu, J. De Baerdemaeker, C. Dauwe, M. Weber, K.G. Lynn, D. Depla, S. Aldea, I.F.J. Vankelecom, C. Vandecasteele, B. Van der Bruggen, Physico-chemical characterization of nanofiltration membranes, Chemphyschem, 8 (2007) 370-379.

[18] J. Stawikowska, A.G. Livingston, Nanoprobe imaging molecular scale pores in polymeric membranes, Journal of Membrane Science, 413 (2012) 1-16.

[19] W.S. Hung, M. De Guzman, S.H. Huang, K.R. Lee, Y.C. Jean, J.Y. Lai, Characterizing Free Volumes and Layer Structures in Asymmetric Thin-Film Polymeric Membranes in the Wet Condition Using the Variable Monoenergy Slow Positron Beam, Macromolecules, 43 (2010) 6127-6134.

[20] F.A. Pacheco, I. Pinnau, M. Reinhard, J.O. Leckie, Characterization of isolated polyamide thin films of RO and NF membranes using novel TEM techniques, Journal of Membrane Science, 358 (2010) 51-59.

[21] C. Zimmerman, A. Singh, W. Koros, Tailoring mixed matrix composite membranes for gas separations, Journal of Membrane Science, 137 (1997) 145-154.

[22] R. Mahajan, D.Q. Vu, W.J. Koros, Mixed matrix membrane materials: An answer to the challenges faced by membrane based gas separations today?, Journal of the Chinese Institute of Chemical Engineers, 33 (2002) 77-86.

[23] M.D. Jia, K.V. Peinemann, R.D. Behling, MOLECULAR-SIEVING EFFECT OF THE ZEOLITE-FILLED SILICONE-RUBBER MEMBRANES IN GAS PERMEATION, Journal of Membrane Science, 57 (1991) 289-296.

[24] J.S. Taurozzi, H. Arul, V.Z. Bosak, A.F. Burban, T.C. Voice, M.L. Bruening, V.V. Tarabara, Effect of filler incorporation route on the properties of polysulfone-silver

nanocomposite membranes of different porosities, Journal of Membrane Science, 325 (2008) 58-68.

[25] L. Brunet, D.Y. Lyon, K. Zodrow, J.C. Rouch, B. Caussat, P. Serp, J.C. Remigy, M.R. Wiesner, P.J.J. Alvarez, Properties of membranes containing semi-dispersed carbon nanotubes, Environmental Engineering Science, 25 (2008) 565-575.

[26] J.H. Choi, J. Jegal, W.N. Kim, Fabrication and characterization of multi-walled carbon nanotubes/polymer blend membranes, Journal of Membrane Science, 284 (2006) 406-415.

[27] L. Yan, Y.S. Li, C.B. Xiang, Preparation of poly(vinylidene fluoride)(pvdf) ultrafiltration membrane modified by nano-sized alumina (Al2O3) and its antifouling research, Polymer, 46 (2005) 7701-7706.

[28] V. Smuleac, L. Bachas, D. Bhattacharyya, Aqueous-phase synthesis of PAA in PVDF membrane pores for nanoparticle synthesis and dichlorobiphenyl degradation, Journal of Membrane Science, (2009).

[29] P. Aerts, A.R. Greenberg, R. Leysen, W.B. Krantz, V.E. Reinsch, P.A. Jacobs, The influence of filler concentration on the compaction and filtration properties of Zirfon (R)-composite ultrafiltration membranes, Separation and Purification Technology, 22-3 (2001) 663-669.

[30] P. Aerts, S. Kuypers, I. Genne, R. Leysen, J. Mewis, I.F.J. Vankelecom, P.A. Jacobs, Polysulfone-ZrO2 surface interactions. The influence on formation, morphology and properties of zirfon-membranes, J. Phys. Chem. B, 110 (2006) 7425-7430.

[31] L. Wu, M. Shamsuzzoha, S.M.C. Ritchie, Preparation of cellulose acetate supported zero-valent iron nanoparticles for the dechlorination of trichloroethylene in water, Journal of Nanoparticle Research, 7 (2005) 469-476.

[32] J.M.N. M.M. Pendergast, A.K. Ghosh, E.M.V. Hoek, Using nanocomposite membrane materials to understand and control reverse osmosis membrane compaction, Desalination, accepted (2010).

[33] M. Luo, Q. Wen, J. Liu, H. Liu, Z. Jia, Fabrication of SPES/Nano-TiO2 Composite Ultrafiltration Membrane and Its Anti-fouling Mechanism, Chinese Journal of Chemical Engineering, 19 (2011) 45-51.

[34] E. Celik, H. Park, H. Choi, H. Choi, Carbon nanotube blended polyethersulfone membranes for fouling control in water treatment, Water Research, 45 (2011) 274-282.

[35] W. Yuan, H. Chen, R. Chang, L. Li, Synthesis and characterization of high performance NaA zeolite-polyimide composite membranes on a ceramic hollow fiber by dip-coating deposition, Desal, 273 (2011) 9-9.

[36] M.L. Lind, A.K. Ghosh, A. Jawor, X. Huang, W. Hou, Y. Yang, E.M.V. Hoek, Influence of Zeolite Crystal Size on Zeolite-Polyamide Thin Film Nanocomposite Membranes, Langmuir, 25 (2009) 10139-10145.

[37] B.H. Jeong, E.M.V. Hoek, Y.S. Yan, A. Subramani, X.F. Huang, G. Hurwitz, A.K. Ghosh, A. Jawor, Interfacial polymerization of thin film nanocomposites: A new concept for reverse osmosis membranes, Journal of Membrane Science, 294 (2007) 1-7.

[38] B.K. Nandi, R. Uppaluri, M.K. Purkait, Effects of dip coating parameters on the morphology and transport properties of cellulose acetate–ceramic composite membranes, Journal of Membrane Science, 330 (2009) 246-258.

[39] G. Suchanek, Mechanistic equations for membrane transport of multicomponent solutions, Gen Physiol Biophys, 25 (2006) 53-63.

[40] M. Mulder, Basic principles of membrane technology, 2nd ed., Kluwer Academic, Dordrecht ; Boston, 1996.

[41] Z.V.P. Murthy, A. Choudhary, Separation and estimation of nanofiltration membrane transport parameters for cerium and neodymium, Rare Metals, 31 (2012) 500-506.

[42] V. Nikonenko, V. Zabolotsky, C. Larchet, B. Auclair, G. Pourcelly, Mathematical description of ion transport in membrane systems, Desalination, 147 (2002) 369-374.

[43] A.R.D. Verliefde, E.R. Cornelissen, S.G.J. Heijman, E.M.V. Hoek, G.L. Amy, B.V.d. Bruggen, J.C. van Dijk, Influence of Solute−Membrane Affinity on Rejection of Uncharged Organic Solutes by Nanofiltration Membranes, Environ Sci Technol, 43 (2009) 2400-2406.

[44] H.K. Lonsdale, U. Merten, R.L. Riley, Transport Properties of Cellulose Acetate Osmotic Membranes, Journal of Applied Polymer Science, 9 (1965) 1341-&.

[45] M. Soltanieh, W.N. Gill, Review of Reverse-Osmosis Membranes and Transport Models, Chem Eng Commun, 12 (1981) 279-363.

[46] W.S.W. Ho, W.S.W.H.K.K. Sirkar, Membrane Handbook, Chapman & Hall, 1992.

[47] J.G. Wijmans, R.W. Baker, The Solution-Diffusion Model - a Review, Journal of Membrane Science, 107 (1995) 1-21.

[48] D.R. Paul, Reformulation of the solution-diffusion theory of reverse osmosis, Journal of Membrane Science, 241 (2004) 371-386.

[49] Y. Zhao, J.S. Taylor, S. Chellam, Predicting RO/NF water quality by modified solution diffusion model and artificial neural networks, Journal of Membrane Science, 263 (2005) 38-46.

[50] Z.V.P. Murthy, S.K. Gupta, Estimation of mass transfer coefficient using a combined nonlinear membrane transport and film theory model, Desalination, 109 (1997) 39-49.

[51] A. Yaroshchuk, X. Martinez-Llado, L. Llenas, M. Rovira, J. de Pablo, Solution-diffusion-film model for the description of pressure-driven trans-membrane transfer of electrolyte mixtures: One dominant salt and trace ions, Journal of Membrane Science, 368 (2011) 192-201.

[52] S. Chellam, J.S. Taylor, Simplified analysis of contaminant rejection during ground-and surface water nanofiltration under the information collection rule, Water Research, 35 (2001) 2460-2474.

[53] L.G. Peeva, E. Gibbins, S.S. Luthra, L.S. White, R.P. Stateva, A.G. Livingston, Effect of concentration polarisation and osmotic pressure on flux in organic solvent nanofiltration, Journal of Membrane Science, 236 (2004) 121-136.

[54] M.S.H. Bader, Nanofiltration for oil-fields water injection operations: analysis of concentration polarization, Desalination, 201 (2006) 106-113.

[55] Y. Ku, S.W. Chen, W.Y. Wang, Effect of solution composition on the removal of copper ions by nanofiltration, Separation and Purification Technology, 43 (2005) 135-142.

[56] A. Yaroshchuk, X. Martinez-Llado, L. Llenas, M. Rovira, J. de Pablo, J. Flores, P. Rubio, Mechanisms of transfer of ionic solutes through composite polymer nano-filtration membranes in view of their high sulfate/chloride selectivities, Desalin Water Treat, 6 (2009) 48-53.

[57] S. Bason, O. Kedem, V. Freger, Determination of concentration-dependent transport coefficients in nanofiltration: Experimental evaluation of coefficients, Journal of Membrane Science, 326 (2009) 197-204.

[58] S. Bason, Y. Kaufman, V. Freger, Analysis of Ion Transport in Nanofiltration Using Phenomenological Coefficients and Structural Characteristics, J. Phys. Chem. B, 114 (2010) 3510-3517.

[59] P. Mukherjee, A.K. SenGupta, Some observations about electrolyte permeation mechanism through reverse osmosis and nanofiltration membranes, Journal of Membrane Science, 278 (2006) 301-307.

[60] E. Csefalvay, V. Pauer, P. Mizsey, Recovery of copper from process waters by nanofiltration and reverse osmosis, Desalination, 240 (2009) 132-142.

[61] J. Chen, J.Q. Huang, J.D. Li, X. Zhan, C.X. Chen, Mass transport study of PVA membranes for the pervaporation separation of water/ethanol mixtures, Desalination, 256 (2010) 148-153.

[62] A. Miyagi, H. Nabetani, M. Nakajima, Analysis of transport mechanism of binary organic solvent system through a PDMS-based dense membrane using a regular solution model combined with a solution-diffusion model, Separation and Purification Technology, 88 (2012) 216-226.

[63] S.J. Han, S.S. Luthra, L. Peeva, X.J. Yang, A.G. Livingston, Insights into the transport of toluene and phenol through organic solvent nanofiltration membranes, Separation Science and Technology, 38 (2003) 1899-1923.

[64] R. Subramanian, K.S.M.S. Raghavarao, H. Nabetani, M. Nakajima, T. Kimura, T. Maekawa, Differential permeation of oil constituents in nonporous denser polymeric membranes, Journal of Membrane Science, 187 (2001) 57-69.

[65] M.A. Mazid, Mechanisms of Transport through Reverse-Osmosis Membranes, Separation Science and Technology, 19 (1984) 357-373.

[66] A.E. Yaroshchuk, The role of imperfections in the solute transfer in nanofiltration, Journal of Membrane Science, 239 (2004) 9-15.

[67] D. Fierro, A. Boschetti-de-Fierro, V. Abetz, The solution-diffusion with imperfections model as a method to understand organic solvent nanofiltration of multicomponent systems, Journal of Membrane Science, 413 (2012) 91-101.

[68] A.E. Yaroshchuk, Solution-Diffusion-Imperfection Model Revised, Journal of Membrane Science, 101 (1995) 83-87.

[69] T. Okada, T. Matsuura, A New Transport Model for Pervaporation, Journal of Membrane Science, 59 (1991) 133-150.

[70] C.L. Chang, C. Hsuan, Y.C. Chang, Pervaporation performance analysis and prediction - using a hybrid solution-diffusion and pore-flow model, Journal of the Chinese Institute of Chemical Engineers, 38 (2007) 43-51.

[71] P. Sukitpaneenit, T.S. Chung, L.Y. Jiang, Modified pore-flow model for pervaporation mass transport in PVDF hollow fiber membranes for ethanol-water separation (vol 362, pg 393, 2010), Journal of Membrane Science, 384 (2011) 226-227.

[72] P. Banerjee, S. De, Coupled concentration polarization and pore flow modeling of nanofiltration of an industrial textile effluent, Separation and Purification Technology, 73 (2010) 355-362.

[73] T. Matsuura, S. Sourirajan, Reverse-Osmosis Transport through Capillary Pores under the Influence of Surface Forces, Ind Eng Chem Proc Dd, 20 (1981) 273-282.

[74] W.S.W. Ho, K.K. Sirkar, Membrane handbook, Van Nostrand Reinhold, New York, 1992.

[75] S. Sourirajan, T. Matsuura, N.R.C. Canada, Reverse Osmosis, Ultrafiltration Process Principles, National Research Council Canada, 1985.

[76] S. Jain, S.K. Gupta, Analysis of modified surface force pore flow model with concentration polarization and comparison with Spiegler-Kedem model in reverse osmosis systems, Journal of Membrane Science, 232 (2004) 45-61.

[77] H. Mehdizadeh, J.M. Dickson, Theoretical Modification of the Surface Force Pore Flow Model for Reverse-Osmosis Transport, Journal of Membrane Science, 42 (1989) 119-145.

[78] H. Mehdizadeh, J.M. Dickson, Evaluation of Surface Force-Pore Flow and Modified Surface Force-Pore Flow Models for Reverse-Osmosis Transport, Chem Eng Commun, 103 (1991) 65-82.

[79] D.E. Meyer, M. Williams, D. Bhattacharyya, Reverse Osmosis, in: Kirk-Othmer Encyclopedia of Chemical Technology, John Wiley & Sons, Inc., 2000.

[80] A. Moradi, A. Farsi, S.S. Mansouri, M. Sarcheshmehpoor, A new approach for modeling of RO membranes using MD-SF-PF model and CFD technique, Res Chem Intermediat, 38 (2012) 161-177.

[81] B. Sen Gupta, M.A. Hashim, Numerical simulation of separation factor of NaCl in surface force pore flow model, Chem Eng Technol, 29 (2006) 1061-1065.

[82] J. Geens, K. Boussu, C. Vandecasteele, B. Van der Bruggen, Modelling of solute transport in non-aqueous nanofiltration, Journal of Membrane Science, 281 (2006) 139-148.

[83] F.B. Peng, X.F. Huang, A. Jawor, E.M.V. Hoek, Transport, structural, and interfacial properties of poly (vinyl alcohol)-polysulfone composite nanofiltration membranes, Journal of Membrane Science, 353 (2010) 169-176.

[84] A. Kargol, M. Przestalski, M. Kargol, A study of porous structure of cellular membranes in human erythrocytes, Cryobiology, 50 (2005) 332-337.

[85] S. Koter, The Kedem-Katchalsky equations and the sieve mechanism of membrane transport, Journal of Membrane Science, 246 (2005) 109-111.

[86] G. Suchanek, On the derivation of the Kargol's mechanistic transport equations from the Kedem-Katchalsky phenomenological equations, Gen Physiol Biophys, 24 (2005) 247-258.

[87] S. Koter, Determination of the parameters of the Spiegler-Kedem-Katchalsky model for nanofiltration of single electrolyte solutions, Desalination, 198 (2006) 335-345.

[88] M. Kargol, A. Kargol, Investigation of reverse osmosis on the basis of the Kedem-Katchalsky equations and mechanistic transport equations, Desalination, 190 (2006) 267-276.

[89] Z. Kovacs, M. Discacciati, W. Samhaber, Modeling of amino acid nanofiltration by irreversible thermodynamics, Journal of Membrane Science, 332 (2009) 38-49.

[90] T. Fukuda, W.K. Yang, A. Yamauchi, KCl transport mechanism across charged mosaic membrane in KCl-sucrose mixed system, Journal of Membrane Science, 212 (2003) 255-261.

[91] S.J. Paynter, B.J. Fuller, R.W. Shaw, Temperature dependence of Kedem-Katchalsky membrane transport coefficients for mature mouse oocytes in the presence of ethylene glycol, Cryobiology, 39 (1999) 169-176.

[92] M. Jarzynska, M. Pietruszka, The application of the Kedem-Katchalsky equations to membrane transport of ethyl alcohol and glucose, Desalination, 280 (2011) 14-19.

[93] G. Jonsson, F. Macedonio, 2.01 - Fundamentals in Reverse Osmosis, in: D. Editor-in-Chief: Enrico, G. Lidietta (Eds.) Comprehensive Membrane Science and Engineering, Elsevier, Oxford, 2010, pp. 1-22.

[94] K.S. Spiegler, O. Kedem, Citation Classic - Thermodynamics of Hyperfiltration (Reverse-Osmosis) - Criteria for Efficient Membranes, Cc/Eng Tech Appl Sci, (1983) 16-16.

[95] O. Kedem, A. Katchalsky, Permeability of Composite Membranes .1. Electric Current, Volume Flow and Flow of Solute through Membranes, T Faraday Soc, 59 (1963) 1918-&.

[96] S. Wadley, C.J. Brouckaert, L.A.D. Baddock, C.A. Buckley, Modeling of Nanofiltration Applied to the Recovery of Salt from Waste Brine at a Sugar Decolorization Plant, Journal of Membrane Science, 102 (1995) 163-175.

[97] C.K. Diawara, S.M. Lo, M. Rumeau, M. Pontie, O. Sarr, A phenomenological mass transfer approach in nanofiltration of halide ions for a selective defluorination of brackish drinking water, Journal of Membrane Science, 219 (2003) 103-112.

[98] N. Hilal, H. Al-Zoubi, A.W. Mohammad, N.A. Darwish, Nanofiltration of highly concentrated salt solutions up to seawater salinity, Desalination, 184 (2005) 315-326.

[99] H. Al-Zoubi, N. Hilal, N.A. Darwish, A.W. Mohammad, Rejection and modelling of sulphate and potassium salts by nanofiltration membranes: neural network and Spiegler-Kedem model, Desalination, 206 (2007) 42-60.

[100] Z.V.R. Murthy, L.B. Chaudhari, Separation of binary heavy metals from aqueous solutions by nanofiltration and characterization of the membrane using Spiegler-Kedem model, Chem Eng J, 150 (2009) 181-187.

[101] S. Bhattacharjee, J.C. Chen, M. Elimelech, Coupled model of concentration polarization and pore transport in crossflow nanofiltration, Aiche J, 47 (2001) 2733-2745.

[102] S. Deon, P. Dutournie, P. Bourseau, Modeling nanofiltration with Nernst-Planck approach and polarization layer, Aiche J, 53 (2007) 1952-1969.

[103] Lakshmin.N, Transport Phenomena in Artificial Membranes, Chem Rev, 65 (1965) 491-+.

[104] L. Dresner, Some remarks on the integration of the extended Nernst-Planck equations in the hyperfiltration of multicomponent solutions, Desalination, 10 (1972) 27-46.

[105] W.M. Deen, Hindered transport of large molecules in liquid-filled pores, AIChE J., 33 (1987) 1409.

[106] E.H. Cwirko, R.G. Carbonell, Transport of Electrolytes in Charged Pores - Analysis Using the Method of Spatial Averaging, J Colloid Interf Sci, 129 (1989) 513-531.

[107] S.L. Ong, W.W. Zhou, L.F. Song, W.J. Ng, Evaluation of feed concentration effects on salt/ion transport through RO/NF membranes with the Nernst-Planck-Donnan model, Environmental Engineering Science, 19 (2002) 429-439.

[108] W.R. Bowen, H. Mukhtar, Characterisation and prediction of separation performance of nanofiltration membranes, J Membrane Sci, 112 (1996) 263-274.

[109] W.R. Bowen, J.S. Welfoot, P.M. Williams, Linearized transport model for nanofiltration: Development and assessment, Aiche J, 48 (2002) 760-773.

[110] T. Tsuru, S. Nakao, S. Kimura, Calculation of Ion Rejection by Extended Nernst-Planck Equation with Charged Reverse-Osmosis Membranes for Single and Mixed Electrolyte-Solutions, J Chem Eng Jpn, 24 (1991) 511-517.

[111] E. Samson, J. Marchand, Numerical solution of the extended Nernst-Planck model, J Colloid Interf Sci, 215 (1999) 1-8.

[112] J.M.K. Timmer, H.C. Vanderhorst, T. Robbertsen, Transport of Lactic-Acid through Reverse-Osmosis and Nanofiltration Membranes, Journal of Membrane Science, 85 (1993) 205-216.

[113] X.A. Hua, H.F. Zhao, R.J. Yang, W.B. Zhang, W. Zhao, Coupled model of extended Nernst-Planck equation and film theory in nanofiltration for xylo-oligosaccharide syrup, J Food Eng, 100 (2010) 302-309.

[114] A.L. Ahmad, B.S. Ooi, Characterization of composite nanofiltration membrane using two-parameters model of Extended Nernst-Planck Equation, Separation and Purification Technology, 50 (2006) 300-309.

[115] G. Imanidis, P. Luetolf, An extended model based on the modified Nernst-Planck equation for describing transdermal iontophoresis of weak electrolytes, J Pharm Sci-Us, 95 (2006) 1434-1447.

[116] R.P. Buck, Kinetics of Bulk and Interfacial Ionic Motion - Microscopic Bases and Limits for the Nernst-Planck Equation Applied to Membrane Systems, Journal of Membrane Science, 17 (1984) 1-62.

[117] S. Bason, V. Freger, Phenomenological analysis of transport of mono- and divalent ions in nanofiltration, Journal of Membrane Science, 360 (2010) 389-396.

[118] W.M. Deen, Hindered Transport of Large Molecules in Liquid-Filled Pores, Aiche J, 33 (1987) 1409-1425.

[119] P.M. Bungay, H. Brenner, The motion of a closely-fitting sphere in a fluid-filled tube, International Journal of Multiphase Flow, 1 (1973) 25.

[120] A. Szymczyk, N. Fatin-Rouge, P. Fievet, C. Ramseyer, A. Vidonne, Identification of dielectric effects in nanofiltration of metallic salts, Journal of Membrane Science, 287 (2007) 102-110.

[121] S. Deon, P. Dutournie, L. Limousy, P. Bourseau, Transport of salt mixtures through nanofiltration membranes: Numerical identification of electric and dielectric contributions, Separation and Purification Technology, 69 (2009) 225-233.

[122] E. Chevereau, N. Zouaoui, L. Limousy, P. Dutournie, S. Deon, P. Bourseau, Surface properties of ceramic ultrafiltration TiO2 membranes: Effects of surface equilibriums on salt retention, Desalination, 255 (2010) 1-8.

[123] Y. Lanteri, P. Fievet, C. Magnenet, S. Deon, A. Szymczyk, Electrokinetic characterisation of particle deposits from streaming potential coupled with permeate flux measurements during dead-end filtration, Journal of Membrane Science, 378 (2011) 224-232.

[124] Y. Lanteri, P. Fievet, S. Deon, P. Sauvade, W. Ballout, A. Szymczyk, Electrokinetic characterization of hollow fibers by streaming current, streaming potential and electric conductance, Journal of Membrane Science, 411 (2012) 193-200.

[125] G. Hagmeyer, R. Gimbel, Modelling the salt rejection of nanofiltration membranes for ternary ion mixtures and for single salts at different pH values, Desalination, 117 (1998) 247-256.

[126] P.J. Attayek, E.S. Meyer, L. Lina, G.C. Rich, T.B. Clegg, O. Coronell, A remotely controlled, semi-automatic target system for Rutherford backscattering spectrometry and elastic recoil detection analyses of polymeric membrane samples, Nucl Instrum Meth A, 676 (2012) 21-25.

[127] W.R. Bowen, J.S. Welfoot, Modelling of membrane nanofiltration - pore size distribution effects, Chem Eng Sci, 57 (2002) 1393-1407.

[128] T.D. Matthews, H. Yan, D.G. Cahill, O. Coronell, B.J. Marinas, Growth dynamics of interfacially polymerized polyamide layers by diffuse reflectance spectroscopy and Rutherford backscattering spectrometry, Journal of Membrane Science, 429 (2013) 71-80.

[129] T.D. Matthews, H. Yan, D.G. Cahill, O. Coronell, B.J. Mariñas, Growth dynamics of interfacially polymerized polyamide layers by diffuse reflectance spectroscopy and Rutherford backscattering spectrometry, Journal of Membrane Science, 429 (2013) 71-80.

[130] S. Bason, Y. Oren, V. Freger, Characterization of ion transport in thin films using electrochemical impedance spectroscopy II: Examination of the polyamide layer of RO membranes, Journal of Membrane Science, 302 (2007) 10-19.

[131] A. Ben-David, S. Bason, J. Jopp, Y. Oren, V. Freger, Partitioning of organic solutes between water and polyamide layer of RO and NF membranes: Correlation to rejection, Journal of Membrane Science, 281 (2006) 480-490.

[132] A.E. Yaroshchuk, Rejection of single salts versus transmembrane volume flow in RO/NF: thermodynamic properties, model of constant coefficients, and its modification, Journal of Membrane Science, 198 (2002) 285-297.

[133] X.J. Zhang, D.G. Cahill, O. Coronell, B.J. Marinas, Partitioning of salt ions in FT30 reverse osmosis membranes, Appl Phys Lett, 91 (2007).

[134] A.E. Yaroshchuk, S.S. Dukhin, Role of Ionic Associates in Membrane Equilibria and Reverse-Osmosis, Colloid J Ussr+, 49 (1987) 1021-1024.

[135] B.J. Marinas, R.E. Selleck, Reverse-Osmosis Treatment of Multicomponent Electrolyte-Solutions, Journal of Membrane Science, 72 (1992) 211-229.

[136] R.D. Noble, Perspectives on mixed matrix membranes, Journal of Membrane Science, 378 (2011) 393-397.

[137] R.H.B. Bouma, A. Checchetti, G. Chidichimo, E. Drioli, Permeation through a heterogeneous membrane: The effect of the dispersed phase, Journal of Membrane Science, 128 (1997) 141-149.

[138] J.C. Maxwell, A treatise on electricity and magnetism, Clarendon press, Oxford,, 1873.

[139] T.S. Chung, L.Y. Jiang, Y. Li, S. Kulprathipanja, Mixed matrix membranes (MMMs) comprising organic polymers with dispersed inorganic fillers for gas separation, Prog Polym Sci, 32 (2007) 483-507.

[140] H.K. Lonsdale, R.L. Riley, C.R. Lyons, D.P. Carosella, Transport in Composite Reverse Osmosis Membranes, in: M. Bier (Ed.) Membrane Processes in Industry and Biomedicine, Plenum Press, New York, 1971.

[141] M.C.Y. Wong, K. Martinez, G.Z. Ramon, E.M.V. Hoek, Impacts of operating conditions and solution chemistry on osmotic membrane structure and performance, Desalination, 287 (2012) 340-349.

[142] G. Shock, A. Miguel, Mass transfer and pressure loss in spiral wound modules, Desalination, 64 (1987) 339-352.

[143] B.K. Dutta, Principles of Mass Transfer and Separation Processes, in, Prentice-Hall, New Delhi, 2007.

[144] S. De, S. Bhattacharjee, P.K. Bhattacharya, Development of Correlations for Mass Transfer Coefficient in Ultrafiltration Systems, Developments in Chemical Engineering and Mineral Processing, 3 (1995) 187-206.

[145] S. Ganguly, P.K. Bhattacharya, Development of concentration profile and prediction of flux for ultrafiltration in a radial cross flow cell, Journal of Membrane Science, 97 (1994) 185-198.

[146] V.S. Minnikanti, S. DasGupta, S. De, Prediction of mass transfer coefficient with suction for turbulent flow in cross flow ultrafiltration, Journal of Membrane Science, 157 (1999) 227-239.

[147] W.S. Opong, A.L. Zydney, Diffusive and Convective Protein Transport through Asymmetric Membranes, Aiche J, 37 (1991) 1499-1510.

[148] K.A. Smith, C.K. Colton, E.W. Merrill, L.B. Evans, Convective Transport in a Batch Dialyzer: Determination of the True Membrane Permeability from a Single Measurement, in: AiChE Symposium Series, 1968.

[149] G. Guillen, E.M.V. Hoek, Modeling the impacts of feed spacer geometry on reverse osmosis and nanofiltration processes, Chem Eng J, 149 (2009) 221-231.

[150] J.A. Howell, Design of Membrane Systems, in: J.A. Howell, V. Sanchez, R.W. Field (Eds.) Membranes in Bioprocessing: Theory and Applications, Springer Netherlands, 1993.

[151] J.C. Crittenden, R.R. Trussell, D.W. Hand, K.J. Howe, G. Tchobanoglous, Reverse Osmosis, in: Water Treatment: Principles and Design, John Wiley & Sons, Hoboken, New Jersey, 2005, pp. 1429-1506

[152] A.E. Childress, M. Elimelech, Relating Nanofiltration Membrane Performance to Membrane Charge (Electrokinetic) Characteristics, Environ Sci Technol, 34 (2000) 3710-3716.

[153] C. Bellona, J.E. Drewes, The role of membrane surface charge and solute physico-chemical properties in the rejection of organic acids by NF membranes, Journal of Membrane Science, 249 (2005) 227-234.

[154] A.R.D. Verliefde, E.R. Cornelissen, S.G.J. Heijman, E.M.V. Hoek, G.L. Amy, B. Van Der Bruggen, J.C. Van Dijk, Influence of Solute-Membrane Affinity on Rejection of Uncharged Organic Solutes by Nanofiltration Membranes, Environ. Sci. Technol., 43 (2009) 2400-2406.

[155] B.P. Boudreau, The diffusive toruosity of fine-grained ulithified sediments, Geochim. Cosmochim. Ac., 60 (1996) 3139-3142.

[156] Y. Endo, M. Alonso, Physical meaning of specific cake resistance and effects of cake properties in compressible cake filtration, Filtration & Separation, 38 (2001) 43-46.

[157] R.S. Faibish, M. Elimelech, Y. Cohen, Effect of interparticle electrostatic double layer interactions on permeate flux decline in crossflow membrane filtration of colloidal suspensions: An experimental investigation, J. Colloid Interf. Sci., 204 (1998) 77-86.

[158] S.G. Yiantsios, A.J. Karabelas, The effect of colloid stability on membrane fouling, Desalination, 118 (1998) 143-152.

[159] A. Achilli, T.Y. Cath, A.E. Childress, Power generation with pressure retarded osmosis: An experimental and theoretical investigation, Journal of Membrane Science, 343 (2009) 42-52.

[160] N.Y. Yip, A. Tiraferri, W.A. Phillip, J.D. Schiffman, L.A. Hoover, Y.C. Kim, M. Elimelech, Thin-Film Composite Pressure Retarded Osmosis Membranes for Sustainable Power Generation from Salinity Gradients, Environ Sci Technol, 45 (2011) 4360-4369.

[161] K.L. Lee, R.W. Baker, H.K. Lonsdale, Membranes for Power Generation by Pressure-Retarded Osmosis, Journal of Membrane Science, 8 (1981) 141-171.

[162] S. Loeb, T. Leonid, E. Korngold, J. Freiman, Effect of porous support fabric on osmosis through a Loeb-Sourirajan type asymmetric membrane, Journal of Membrane Science, 129 (1997) 243-249.

[163] A. Tiraferri, N.Y. Yip, A.P. Straub, S. Romero-Vargas, Castrillon, M. Elimelech, A Method for the Simultaneous Determination of Transport and Structural Parameters of Forward Osmosis Membranes, Journal of Membrane Science, (2013).

[164] N. Widjojo, T.-S. Chung, M. Weber, C. Maletzko, V. Warzelhan, The role of sulphonated polymer and macrovoid-free structure in the support layer for thin-film composite (TFC) forward osmosis (FO) membranes, Journal of Membrane Science, 383 (2011) 214-223.

[165] E.M.V. Hoek, Colloidal Fouling Mechanisms in Reverse Osmosis and Nanofiltration, in: Chem. Eng., Yale University, New Haven, CT, 2002, pp. 207.

[166] E.M.V. Hoek, M. Elimelech, Cake-hindered mass transfer: A major fouling mechanism for salt rejecting membranes, Enivironmental Science & Technology, (2002).

[167] R.H. Davis, Modeling of fouling of crossflow microfiltration membranes, Sep. Purif. Meth., 21 (1992) 75-126.

CHAPTER 3

STRUCTURE-PERFORMANCE MODEL TO UNDERSTAND AND IMPROVE NEUTRAL SOLUTE REMOVAL BY RO/NF MEMBRANES

3.1 Introduction

Many researchers have tried to tackle the challenge of enhancing the removal efficiency of micropollutants by NF and RO [1-6]. These studies investigate operational parameters and removal of different organic solutes, and contribute to better understanding membrane retention mechanisms by developing various solute transport models. Numerous mechanistic and mathematical models have been proposed to describe membrane transport [7-12]. Depending on the membrane, diffusion, pore flow, and Donnan exclusion may all be important mechanisms controlling solute transport.

One of the earliest models proposed for NF and RO transport is the solution-diffusion (SD) model [13]. This model is based on the principle of dissolution of water and solute molecules into membranes with a dense "nonporous" layer, followed by diffusion through the membrane due to the chemical potential gradient across the membrane [14]. The SD model simplifies the whole membrane system a black box, with no consideration of structural parameters. This means the solubility (or partition coefficient) and diffusivity of species in the membrane are not related to physical properties, such as pore structure or charge density [15].

Another model describing NF and RO membrane transport includes pore flow, in addition to the SD model [10, 11, 16]. Dissolution of water and solute molecules is proposed to be governed by steric interactions (*i.e.*, size exclusion) and water/solute-membrane chemical interactions (*i.e.*, affinity). When solute size is larger than membrane characteristic pore size, solute will be 100% excluded by the membrane, such that the solute partition coefficient is effectively zero. If solute size is smaller than membrane characteristic pore size, solute partition coefficient is function of solute size/pore size ratio and solute-membrane interaction energy. After dissolution, water and solute will diffuse through membrane independently. This diffusion is hindered by both steric interactions and affinity.

Another approach for porous membrane model based on Spiegler–Kedem transport equations describes flux of uncharged organics through membranes as a combination of hindered diffusive transport and hindered convective transport [9].

Each model can be applied with some degree of success to predict mass transfer of solutes through certain membranes, but selecting the appropriate approach and determining the model parameters are not easy tasks. For example, the solubility and diffusivity of a particular solute in a given membrane material are hard to reliably measure. Although solubility and diffusivity can be related to membrane characteristic pore size, if pore model is applied, the characteristic pore sizes in NF and RO membrane are too small to characterize by conventional characterization techniques. More advanced technologies, such as atomic force microscopy (AFM) [17] and nuclear magnetic resonance (NMR) [18] need to be employed .

In this study, we developed two water/solute pore-flow transport models, each based on different transport mechanisms. One includes mechanisms of solution-diffusion (SD) and the second includes mechanisms of solution-diffusion-convection (SDC). Characteristic structural properties (*i.e.*, characteristic pore radius and thickness-to-porosity ratio) can be determined from the models by relating the experimental results of water permeability and solute rejection. Rejection of ideal solutes (*e.g.*, ethylene glycol and tetrahydrofuran) were measured with three commercial membranes (NF 270, NF 90 and XLE, Dow Filmtec). Model predictions can then be made for rejection of other solutes. These predicted results can then be compared to experimental rejection statistically in order to validate the models. After model validation, the model could illustrate the effects of membrane structure properties, solute properties, solute-membrane interactions, and operation conditions on selected micropollutants rejection by commercial polyaimide NF/RO membranes and lab synthesized PVA membranes.

3.2 Model Development

In the classical solution-diffusion transport model, water and solute are understood to permeate through a "nonporous" membrane skin layer. However, according to molecular dynamic simulations and advanced characterization techniques (e.g., AFM, TEM, NMR, PALS) the free volume throughout the dense polyamide layer contains interconnected pore-like voids with characteristic dimensions in the size range of 0.2 to 0.6 nm [19-22]. Herein, we model dense polymer film fractional free volume (FFV) with a hypothetical cylindrical capillary pore size (r_p), porosity (ε) and pore length ($\Delta x = \tau l$, τ is tortuosity and l is membrane thickness). Among a number of possible errors introduced by such simplified free volume geometry, one of the more obvious issues is that this model ignores the possibility of having free volume spaces that are partially or wholly inaccessible by either solvent or solute. This model also ignores the well known rugose morphology of polyamide RO membranes, the effects of which are only beginning to be studied theoretically and quantitatively [23, 24].

3.2.1 Extended solution-diffusion model

In the solution-diffusion model, the membrane is treated as a "non-porous" film with thickness Δx. Wang *et al.* modified the solution-diffusion model for NF/RO membranes assuming a porous structure [25]. Based on the classic solution-diffusion model, (volumetric) water flux, J_w, can be expressed as

$$J_w = A\left(\Delta p - \Delta\pi\right) = \frac{K_w D_w^m}{\Delta x}\frac{V_w}{R_g T}\left(\Delta p - \Delta\pi\right) \qquad (3.1)$$

and the water solubility (K_w) in membrane is defined as [12]

$$K_w = \frac{\dfrac{\text{mass of water in the membrane}}{\text{volume of membrane}}}{\dfrac{\text{mass of water in the feed}}{\text{volume of water in the feed}}} = \frac{c_w^m}{C_w^f} \qquad (3.2)$$

where c_w^m is the equilibrium water concentration in the membrane ($\text{kg}_{\text{water}}\cdot\text{m}^{-3}{}_{\text{membrane}}$) and C_w^f is the equilibrium water concentration in the bulk feed solution ($\text{kg}_{\text{water}}\cdot\text{m}^{-3}{}_{\text{solution}}$). c_w^m can be defined as

$$c_w^m = \frac{\text{mass of water in the membrane}}{\text{volume of membrane}} = \frac{\text{mass of water in the membrane}}{\text{volume of membrane pores} \times \dfrac{1}{\text{membrane porosity}}} \qquad (3.3)$$
$$= c_w^p \varepsilon$$

where c_w^p is the equilibrium water mass concentration in membrane pore ($\text{kg}_{\text{water}}\cdot\text{m}^{-3}{}_{\text{pore}}$) and ε is the membrane porosity. The ratio of c_w^p to C_w^f can be defined as the water-membrane pore partition coefficient (ϕ_w) [11]

$$\phi_w = \frac{\dfrac{\text{mass of water in the membrane}}{\text{volume of membrane pore}}}{\dfrac{\text{mass of water in the feed}}{\text{volume of water in the feed}}} = \frac{c_w^p}{C_w^f} \qquad (3.4)$$

Combining **Eqns. 3.2-3.4** yields

$$K_w = \phi_w \varepsilon \tag{3.5}$$

According to the water-membrane partition model [10, 11]

$$\phi_w = \left(1-\lambda_w\right)^2 exp\left(-\frac{\Delta G_w}{k_B T}\right) \tag{3.6}$$

where ΔG_w is water-membrane interaction energy, k_B is Boltzmann constant, and λ_w is the ratio of the Stokes radius of water, r_w, to the membrane pore radius, r_p. The diffusion coefficient of water in the membrane (D_w^m) can be related to water diffusivity in bulk (D_w^∞) by the diffusive hindrance factor (K_d) [16]

$$D_w^m = K_d D_w^\infty \tag{3.7}$$

Combining **Eqn. 3.1-3.7** yields

$$J_w = \frac{K_d D_w^\infty \varepsilon}{\Delta x}\left(1-\lambda_w\right)^2 exp\left(-\frac{\Delta G_w}{k_B T}\right)\frac{V_w}{R_g T}\left(\Delta p - \Delta\pi\right) \tag{3.8}$$

and

$$A = \frac{K_d D_w^\infty \varepsilon}{\Delta x}\left(1-\lambda_w\right)^2 exp\left(-\frac{\Delta G_w}{k_B T}\right)\frac{V_w}{R_g T} \tag{3.9}$$

Eqn. 3.8 describes membrane water flux as a function of the pressure drop across the membrane and structural factors (*i.e.*, characteristic pore radius, r_p, and thickness-to-porosity ratio, $\Delta x/\varepsilon$).

Water-membrane interaction energy (ΔG_w) can be related to the interfacial surface tension of water and the membrane [26]

$$\Delta G_w = -2A_w\left(\sqrt{\gamma_w^{LW}\gamma_m^{LW}} + \sqrt{\gamma_w^{+}\gamma_m^{-}} + \sqrt{\gamma_w^{-}\gamma_m^{+}}\right) \tag{3.10}$$

where γ_i^{LW} is the apolar Lifshitz-van der Waals component of the surface tension and γ_i^{+} and γ_i^{-} are the polar electron-acceptor and electron-donor components of the surface tension. Subscripts w and m refer to water and membrane, respectively. A_w (= $\pi r_w^2/2$) is the area of contact between a water molecule and the membrane pore wall.

According to solution-diffusion theory [12, 14], J_s is described by the equation

$$J_s = B\left(C_m - C_p\right) = \frac{K_s D_s^m}{\Delta x}\left(C_m - C_p\right) = \frac{K_s D_s^m}{\Delta x}\left(\beta C_f - C_p\right) \tag{3.11}$$

where β is the concentration polarization factor and D_s^m is the average solute diffusion coefficient in membrane. The solute solubility coefficient in membrane (K_s) is defined as [12]

$$\begin{aligned} K_s &= \frac{\dfrac{\text{mass of solute in the membrane}}{\text{volume of membrane}}}{\dfrac{\text{mass of solute in the feed}}{\text{volume of solution in the feed}}} = \frac{c_s^m}{C_s^f} \\ &= \frac{\dfrac{\text{mass of solute in the membrane}}{\text{volume of membrane pore}} \times \dfrac{\text{volume of membrane pore}}{\text{volume of membrane}}}{\dfrac{\text{mass of solute in the feed}}{\text{volume of solution in the feed}}} \\ &= \frac{c_s^p}{C_s^f}\varepsilon \end{aligned} \tag{3.12}$$

where c_s^m is the equilibrium solute concentration within membrane (kg solute·m^{-3} membrane), c_s^p is the equilibrium solute concentration in membrane pore (kg solute·m^{-3} membrane pore), and ε is the membrane porosity. Solute-membrane partition coefficient (ϕ_s) can be defined as [11]

$$\phi_s = \frac{\dfrac{\text{mass of solute in the membrane}}{\text{volume of membrane pore}}}{\dfrac{\text{mass of solute in the feed}}{\text{volume of solution in the feed}}} = \frac{c_s^p}{C_s^f} \tag{3.13}$$

Combining **Eqns. 3.11-3.13** yields

$$J_s = \frac{\phi_s \varepsilon D_s^m}{\Delta x}\left(\beta C_f - C_p\right) \tag{3.14}$$

The average solute diffusion coefficient in membrane (D_s^m) can be related to solute diffusion coefficient in infinity water (D_s^∞) by hindrance factor (K_d) [16]

$$D_s^m = K_d D_s^\infty \tag{3.15}$$

According to solute-membrane partition model [10, 11]

$$\phi_s = \left(1-\lambda_s\right)^2 exp\left(-\frac{\Delta G_s}{k_B T}\right) \tag{3.16}$$

where ΔG_s is solute-membrane interaction energy and λ_s is the ratio of Stokes radius (r_s) to membrane pore radius (r_p). Combining **Eqns. 3.14-3.16** yields

$$J_s = B\left(\beta C_f - C_p\right) = \frac{K_d D_s^\infty \varepsilon}{\Delta x}\left(1-\lambda_s\right)^2 exp\left(-\frac{\Delta G_s}{k_B T}\right)\left(\beta C_f - C_p\right) \tag{3.17}$$

Combing **Eqns. 2.4 and 3.17** yields

$$R_o = 1 - \frac{C_p}{C_f} = 1 - \frac{\beta B}{J_w + B} = 1 - \frac{\beta \dfrac{K_d D_s^\infty \varepsilon}{\Delta x}\left(1-\lambda_s\right)^2 exp\left(-\dfrac{\Delta G_s}{k_B T}\right)}{J_w + \dfrac{K_d D_s^\infty \varepsilon}{\Delta x}\left(1-\lambda_s\right)^2 exp\left(-\dfrac{\Delta G_s}{k_B T}\right)} \tag{3.18}$$

Eqn. 3.18 describes the observed rejection of a solute as a function of water flux and membrane structural factors. It is important to notice here that if the water flux and solute-membrane interaction energy are known, the solute rejection becomes solely dependent on r_p and $\Delta x/\varepsilon$. When experimentally measured ideal solute rejection and membrane water permeability are fit into **Eqns. 3.9 and 3.18**, the values of r_p and $\Delta x/\varepsilon$ can be determined. Then, **Eqn. 3.18** becomes a predictive model for rejection of other solutes.

The free energy of interaction between solute and membrane immersed in water can be determined from [26]

$$\Delta G_s = 2A_s \left[\begin{array}{l} \sqrt{\gamma_s^{LW}\gamma_w^{LW}} + \sqrt{\gamma_m^{LW}\gamma_w^{LW}} - \sqrt{\gamma_m^{LW}\gamma_s^{LW}} - \gamma_w^{LW} + \sqrt{\gamma_w^+}\left(\sqrt{\gamma_s^-} + \sqrt{\gamma_m^-} - \sqrt{\gamma_w^-}\right) \\ + \sqrt{\gamma_w^-}\left(\sqrt{\gamma_s^+} + \sqrt{\gamma_m^+} - \sqrt{\gamma_w^+}\right) - \sqrt{\gamma_m^-\gamma_s^+} - \sqrt{\gamma_m^+\gamma_s^-} \end{array} \right] \tag{3.19}$$

where γ_i^{LW} is the apolar Lifshitz-van der Waals component of the surface tension and γ_i^+ and γ_i^- are the polar electron-acceptor and electron-donor components of the surface tension. Subscripts *s*, *w*, and *m* refer to solute, water and membrane, respectively. A_s (= $\pi r_s^2/2$) is the contact area between a solute molecule and the membrane.

3.2.2. Modified solution-diffusion-convection model

Solute transport can also be described as a combination of diffusive and convective transport through the model structure of capillary pores [9]. J_s across the membrane can be described as [11]

$$J_s = J_s^D + J_s^C = -K_d D_s^\infty \frac{dc}{dx} + \frac{J_w}{\varepsilon} K_c c \tag{3.20}$$

where J_s^D is diffusive solute flux, J_s^C is convective solute flux, c is solute concentration within membrane pore, and K_c is convective hindrance factor. Observed rejection can be obtained by integrating **Eqn. 3.20** across the membrane thickness using the boundary conditions

$$c = \phi_s \beta C_f \qquad \text{at } x = 0$$

$$c = \phi_s C_p \qquad \text{at } x = \Delta x$$

resulting in

$$R_o = 1 - \frac{C_p}{C_f} = 1 - \frac{\beta\left(1-\lambda_s\right)^2 exp\left(-\frac{\Delta G_s}{k_B T}\right) K_c}{1 - \left[1 - \left(1-\lambda_s\right)^2 exp\left(-\frac{\Delta G_s}{k_B T}\right) K_c\right] exp\left(-\frac{J_w K_c \Delta x}{K_d D_s^\infty \varepsilon}\right)} \tag{3.21}$$

If J_w and ΔG_s are known the R_o is solely dependent on membrane characterized pore size (r_p) and thickness-to-porocity ratio ($\Delta x/\varepsilon$), which are also the governing parameters in determining membrane water permeability (**Eqn. 3.8**) and as with the modified solution diffusion model, experimentally obtained R_o and J_w can be used to characterize r_p and $\Delta x/\varepsilon$. Further, **Eqn. 3.21** can be used to predict rejection of other solutes.

The hindrance coefficients (K_d and K_c) are difficult to accurately determine, however, various estimations have been proposed in literature. Bungay and Brenner [27] proposed expressions for K_d and K_c as a function of λ ($= r_s/r_p$, $0 < \lambda < 1$) and water/solute partition coefficients, ϕ,

$$K_d = \frac{6\pi}{K_t} \tag{3.22}$$

$$K_c = \left(2-\phi\right)\frac{K_s}{2K_t} \tag{3.23}$$

$$K_t = \frac{9}{4}\pi^2\sqrt{2}\left(1-\lambda\right)^{-\frac{5}{2}}\left[1+\sum_{n=1}^{2} a_n\left(1-\lambda\right)^n\right]+\sum_{n=0}^{4} a_{n+3}\lambda^n \tag{3.24}$$

and

$$K_s = \frac{9}{4}\pi^2\sqrt{2}\left(1-\lambda\right)^{-\frac{5}{2}}\left[1+\sum_{n=1}^{2} b_n\left(1-\lambda\right)^n\right]+\sum_{n=0}^{4} b_{n+3}\lambda^n \tag{3.25}$$

The constants in **Eqns. 3.24** and **3.25** are listed in **Table 3.1** [28].

Table 3.1. Constants of the Bungay and Brenner correlation.

a_1	a_2	a_3	a_4	a_5	a_6	a_7
-1.22	1.53	22.51	-5.61	-0.34	-1.22	1.65
b_1	**b_2**	**b_3**	**b_4**	**b_5**	**b_6**	**b_7**
0.12	-0.044	4.02	-3.98	-1.92	4.39	5.01

3.3 Materials and Methods

3.3.1 Solutes

The solutes used in this modeling study were selected based on their different physicochemical properties (polarity and aromaticity). Six different model solutes (ethylene glycol (EG), tetrahydrofuran (THF), diethylphthalate (DEP), benzene, glycerol and hexane), which were divided into four categories (aromatic polar, aromatic apolar, aliphatic polar and aliphatic apolar), were chosen. The solutes and their physicochemical properties were listed in **Table 1**. The solutes radius used in the modeling were Stokes radius, which were calculated by

$$r_s = \frac{kT}{6\pi\eta D} \tag{3.26}$$

where η is the water dynamic viscosity ($\eta = 1.002\times10^{-3}$ Pa.s, at 293 K).

Table 3.2. Physicochemical characteristics for selected organic solutes.

	MW (g/mol)	r_s [29]	D_∞ ($\times 10^{-5}$cm^2/s)	log K_{ow}	γ^{LW} (mJ/m^2)	γ^+ (mJ/m^2)	γ^- (mJ/m^2)
Glycerol	92	0.19	1.10	-1.76	34.0	3.92	57.4
EG	62	0.18	1.16	-1.36	29.0	1.92	47.0
THF	72	0.21	0.99	1.94	27.4	0	15.0
Hexane	78	0.26	0.85	3.90	18.4	0	0
DEP	222	0.32	0.61	2.42	36.5	0	0.99
Benzene	78	0.19	1.1	2.13	28.9	0	2.7

3.3.2 Membranes

The membranes used in this modeling study were both commercially available and laboratory hand-casting NF/RO membranes for different applications: water softening NF membranes: HL (GE Osmonics, Fairfield CT, USA), NF90 and NF270 (Dow Filmtec, Midland MI, USA); brackish water RO membrane: XLE (Dow Filmtec, Midland MI, USA); seawater RO membrane: SWC3+ (Hydranautics, Oceanside CA, USA); and laboratory hand-casting membrane PVAm. All the commercially available membranes are polyamide thin film composite membranes. The PVAm membrane is a malic acid cross-linked Poly(vinyl alcohol)-Polysulfone composite NF membrane. The details of the PVAm membrane synthesis and characterization can be found in a previous publication [30].

3.3.3 Solute and membrane surface tensions

In order to calculate solute-membrane interaction energy (ΔG_i) by using Eq. (11), membrane, solute, solvent (water) surface tension components need to be characterized. The surface tension components of solutes and water can be found in literatures. The membrane surface tension components can be evaluated by Young-Dupré equation [31, 32]:

$$\gamma_w^T\left(1+cos\theta\right)=2\left(\sqrt{\gamma_m^{LW}\gamma_w^{LW}}+\sqrt{\gamma_m^+\gamma_w^-}+\sqrt{\gamma_m^-\gamma_w^+}\right) \tag{3.27}$$

where θ is the contact angle formed between a droplet of liquid L and the tested membrane surface. Three Young-Dupré equations can be set up by performing three times contact angle measurements using three different liquids (water, ethylene glycol and diiodomethane). The three unknown variables of membrane surface tension components can be solved from these three equations.

All contact angle measurements were conducted using an automatic contact angle goniometer (DSA10 KRÜSS GmbH, Hamburg, Germany) equipped with commercial contact angle calculation software (Drop Shape Analysis, KRÜSS GmbH). At least twelve equilibrium contact angles were measured for each sample at different locations. The highest and lowest values were discarded before calculating the average contact angle.

3.3.4 Rejection evaluation

The separation performance of NF and RO membranes (NF270, NF90, XLE) was evaluated in a bench scale cross-flow membrane filtration system equipped with six parallel membrane cells (effective membrane area is 19.4 cm^2, with width of 2.54 cm, length of 7.62 cm and channel height of 0.10 cm, for each membrane cell). Pure water permeability was determined using 18 MΩ laboratory deionized water at 25 °C and applied pressures between 0.69 – 2.76 MPa (100 – 400 psi). The cross-flow rate was set at 0.55 $Gal \cdot min^{-1}$ (3.46×10^{-5} $m^3 \cdot s^{-1}$). Flow conditions were controlled so that the Reynolds number was maintained at 1900 with a mesh spacer in the feed channel. This ensured that the external mass transfer coefficient was 2.42×10^{-4} $m \cdot s^{-1}$, producing a concentration polarization modulus in the range of 1.04 – 1.26 for permeate fluxes in the range of 1 $\times 10^{-6}$ –55 $\times 10^{-6}$ $m \cdot s^{-1}$. Flux was measured by a digital flow meter. Before testing, all the membranes were compacted with deionized water at 3.10 MPa (450 psi) and 25 °C for 16 hours. After permeability measurements, the same membranes were used to characterize the selectivity of selected solutes. Both ethylene glycol and tetrahydrofuran were spiked into deionized water at 30 mg $carbon \cdot L^{-1}$. Solute rejection was found by measuring total organic carbon in feed and permeate solutions. During the rejection experiments, feed pressure was varied (0.69 – 2.76 MPa), while temperature (25 °C) and external mass transfer coefficient (2.42×10^{-4} m/s) were kept constant. In order to eliminate the effect of adsorption of solute onto the membrane surface and into membrane inner structure, feed solution was filtered through all the membranes at 2.76 MPa (400 psi) and 25 °C for 24 hours prior to rejection tests.

3.4 Results and Discussion

3.4.1 Model validation

The surface tension parameters of membrane and solute, determined from contact angle test or adapted from literatures, are shown in **Table 3.3**. These values are combined with **Eqn. 3.10 and 3.19**, and the solute-membrane interaction energy is calculated (**Table 3.4**).

Table 3.3. Membrane surface contact angle and surface tension components.

Membrane	Contact angle (°)			γ^{LW} (mJ/m^2)	γ^{+} (mJ/m^2)	γ^{-} (mJ/m^2)
	Water	**Glycerol**	**Diiodomethane**			
NF 270	39.7	27.6	31.6	43.4	0.24	37.8
NF 90	67.5	53.4	33.9	36.6	0.78	9.28
XLE	67.6	50.1	18.2	37.2	0.41	8.94
HL	41.2	34.6	23.1	44.7	1.07	26.6
SWC3+	58.3	7.0	11.6	49.8	0.44	14.5
PVAm	21.6	48.9	35.5	41.8	0.00	64.0

Table 3.4. Water/solute-membrane interaction energy.

ΔG ($\times 10^{-21}$ J)	NF 270	NF 90	XLE
Water	-2.62	-2.44	-1.78
EG	0.58	-0.09	-0.18
THF	-0.76	-2.40	-2.60

Experimentally obtained membrane water permeability and EG rejection data were fitted into SD model (Equations (1) and (3)) and SDC model (Equations (1) and (5)), independently. The experimental and model fitted EG rejection curves were plotted in **Figure 3.1**. The values of membrane characterized pore size (r_p) and porosity to thickness ratio ($\varepsilon/\Delta x$), obtained by model fitting as well as from literature [19], are shown in **Table 3.5**.

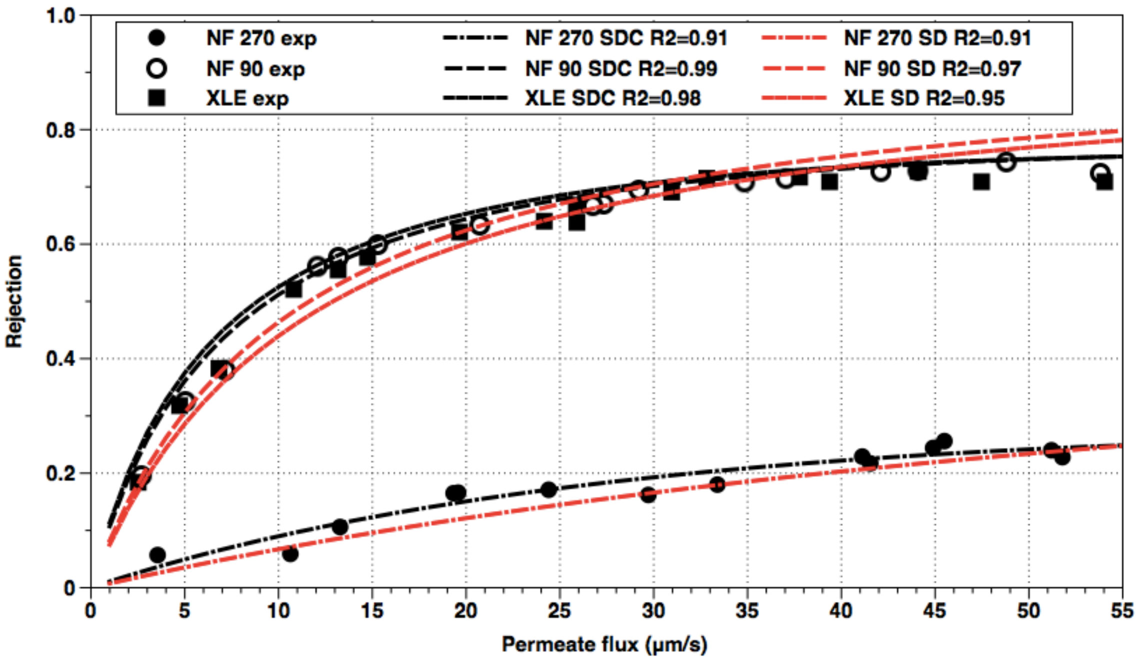

Figure 3.1. Experimental and fitted EG rejection as function of permeate flux.

Table 3.5. Fitted membrane characteristic pore radius and thickness/porosity ratio.

	NF270			NF90			XLE		
	SDC	SD	Ref.	SDC	SD	Ref.	SDC	SD	Ref.
r_p **(nm)**	0.29	0.35	0.34	0.24	0.25	0.25	0.24	0.25	N.A.
$\Delta x/\varepsilon$ **(nm)**	94	188	N.A.	61	113	N.A.	72	98	N.A.

N.A.: not available

Among the three membranes tested, NF270 membrane has largest characteristic pore radius and thickness/porosity ratio (**Table 3.5**). The NF90 and XLE membranes have very similar structural characteristics and separation performance. The membrane characteristic pore radius and thickness-to-porosity ratio obtained by fitting experimental data to the SDC model are larger than these obtained by the SD model.

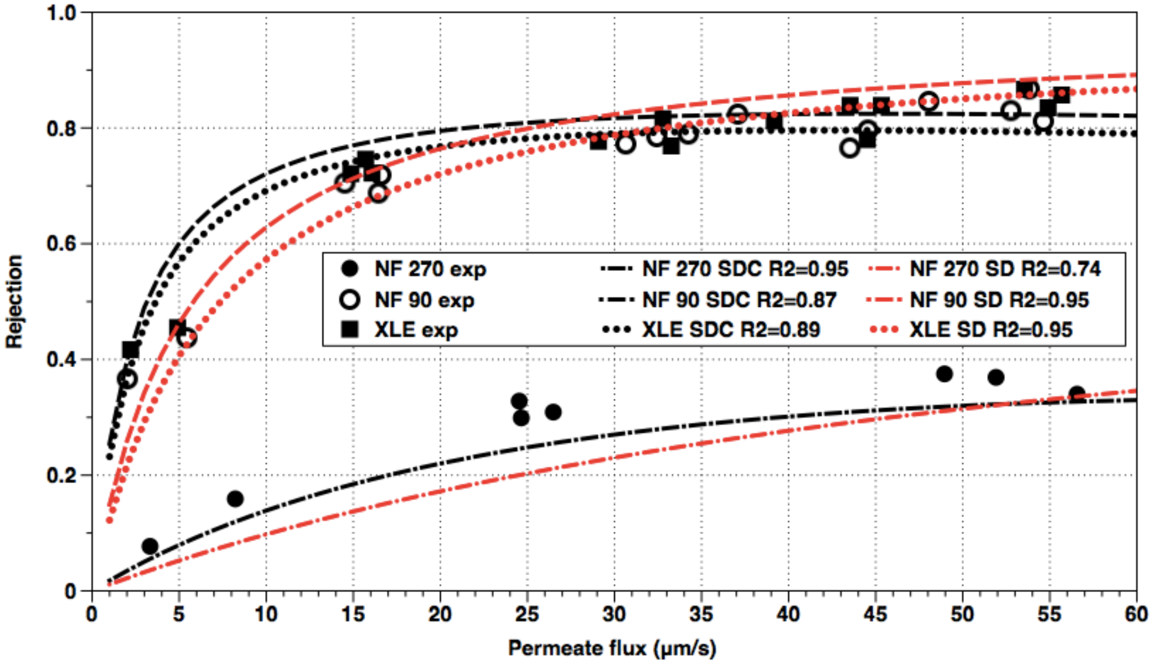

Figure 3.2. Experimental and predicted THF rejection as function of permeate flux.

With membrane characterized pore size (r_p) and porosity to thickness ratio ($\varepsilon/\Delta x$) known (**Table 3.5**), both the SD and SDC transport models can be used to predict the rejection of other solutes by NF270, NF90 and XLE membranes. The experimental and model fitted THF rejection curves were plotted in **Figure 3.2**, regression analysis was used to evaluate the model fitting. For NF90 and XLE membranes, the SD model prediction fitted experimental rejection data better than SDC model. However, the SDC model fits data better than the SD model for the NF270 membrane. The results suggest for tight NF (*e.g.*, NF90) and brackish water RO (*e.g.*, XLE) membranes solution-diffusion mechanism should be employed to explain membrane transport. For NF membranes with large characteristic pore radius, the mechanism of convection must be included.

3.4.2 Solute/membrane surface tension and interaction energy

ΔG_s (**Table 3.6**) can be used to quantify the interaction (either attractive or repulsive) between solute and membrane. If $\Delta G_s > 0$, repulsive interaction exists between organic solute and membrane. The transport of solute molecules through membrane pore will be denied. A high solute rejection of membrane can be expected. If $\Delta G_s < 0$, there will be attractive force between solute and membrane. Meanwhile, the solute transport through membrane pore will be favored. The membrane will have low rejection to solute. Due to the organic nature of polymeric membrane, organic solutes tend to partition into membrane (organic) phase from water phase. This tendency can be explained by hydrophobicity of organic solute. Octanol-water partitioning coefficient (K_{ow}) is normally used by environmental scientists to quantify the hydrophobicity of organics. In this study, except the aliphatic polar solute glycerol, all other solutes exhibited negative interaction free energy with all the polymeric membranes. The transport of these organic solutes through polymeric membranes is favored.

Table 3.6. Solute-Membrane interaction free energy.

ΔG_s ($\times 10^{-21}$ J)	**PVAm**	**NF270**	**HL**	**SWC3+**	**XLE**
Glycerol	2.24	1.44	1.49	0.51	0.36
Hexane	-2.11	-3.56	-4.02	-5.84	-6.82
DEP	-2.59	-5.01	-5.65	-8.78	-9.73
Benzene	-0.41	-1.29	-1.48	-2.59	-3.00

Based on the data shown in **Table 3.6**, glycerol has positive interaction free energy with all membranes, because it is a very hydrophilic organic solute ($\log K_{ow} = -1.76$). Among the three solutes showed negative ΔG_s, DEP has the largest negative ΔG_s and benzene has the smallest negative ΔG_s with all the membranes. DEP is an aromatic polar organic molecule, which is more likely to partition into aromatic or polar organic phase due to the similarity of the structure. All the membranes used in this study contain either aromatic (polyamide) or polar (PVA) structure. Also, the Stokes radius of DEP is the highest among all the solutes in this study, so the contact area between DEP and membrane is the largest. As a result, DEP has the highest attractive interaction with membranes. The reason for why aliphatic apolar solute hexane has higher attractive interaction with membranes is that hexane has larger Stokes radius (contact area) than benzene.

For all the membranes in this study, commercial available polyamide membranes show either less positive (glycerol) ΔG_s or more negative (hexane, benzene, DEP) ΔG_s values than laboratory hand-casting PVA membrane. This can be explained by the difference in hydrophobicity/hydrophilicity of membrane surface. Polyamide membranes, which has large amount of aromatic structure, are usually considered as relatively hydrophobic membrane with water contact angle in the range of 60 – 70°. However, the water contact angle of PVAm membrane is 22°, which suggests a relatively hydrophilic surface. Hydrophobic organic solutes (hexane benzene and DEP) are more easily attracted by relative hydrophobic polyamide membranes than hydrophilic PVAm membrane, which result in more negative value for solute-membrane interaction energy.

Polyamide NF membranes (HL, NF270) have less negative ΔG_s values than polyamide RO membranes (SWC3+, XLE). The cross-linking degree in polyamide NF membrane is lower than that in polyamide RO membrane. Consequently, there will be more free carboxylic functional groups available in membrane structure. So, the surface hydrophilicity of NF membrane is higher than RO membrane.

3.4.3 Prediction of solute rejection

In order to predict solute rejection using **Eqn. 3.21**, operation parameters (J_w, k_f), solute property parameters (r_s, D_s), membrane structure property parameters (r_p, Δx and ε), solute-membrane interaction parameter (ΔG_s) are required (assume the temperature is constant at 293 K). In this study, values of solute property parameters and ΔG_s were fixed in all model simulations. Other parameters will use the default values if not defined, which are shown in **Table 3.7**. The default values of model fitting parameters were chosen based on normal industrial operation conditions and typical membrane properties. Also, the values of fitting parameters will be optimized according to the model prediction results.

Table 3.7. Model fitting parameters.

Parameter		**Unit**	**Default value**
Pore size	r_p	nm	0.40
Solvent flux	J_v	μm/s	20
Mass transfer coefficient	k_f	μm/s	300
Concentration polarization	β		1.07
Boltzmann constant	k	$\times 10^{-23}$ J/K	1.38
Temperature	T	K	298.15
Coating film thickness	Δx	nm	200
Surface porosity	ε		0.04

3.4.3.1 Effect of operation parameters

3.4.3.1.1 Effect of permeate flux

The prediction of solutes rejection by membranes as a function of permeate flux was shown in **Figure 3.3**. Based on the results, within the practical permeate flux range (0 – 30 μm/s), solute rejection by membrane increased as membrane permeate flux increased. However, the increasing in solute rejection became slow when the permeate flux was relatively high, which is corresponded to salt rejection study in other research work [33]. As the permeate flux increases, progressively more solvent (water) passes through membrane relative to solute. This leads to the concentration of solute in permeate side decreases with increasing permeate flux. According to Eq. (5), as the concentration of solute in permeate going down, the solute rejection should increase. The results here suggest that operating NF/RO process at high membrane throughput (permeate flux) will also benefit the solute rejection. So, the following modeling investigation will be performed with high permeate flux (20 μm/s).

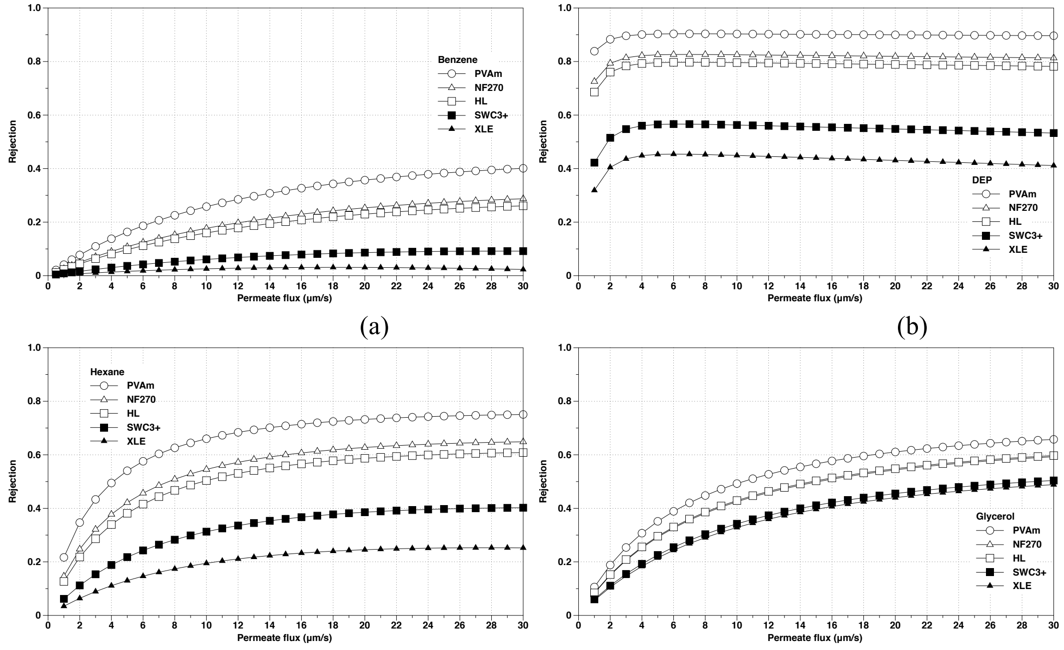

(a) (b)

(c) (d)

Figure 3.3. Predicted rejection of benzene (a), DEP (b), hexane (c) and glycerol (d) as a function of permeate flux.

3.4.3.1.2 Effect of external mass transfer

Figure 3.4 presents the prediction of solute rejection as a function of external mass transfer coefficient. Similar behavior was observed with the effect of permeate flux on solute rejection. Large external mass transfer coefficient is required to obtain high solute rejection, especially for benzene rejection by commercial RO membranes. During the NF/RO process, concentration polarization will reduce the difference of solute concentration across the membrane, thereby lowing the solute rejection by membrane. One of the effective ways to reduce concentration polarization is to enhance external mass transfer to avoid solute accumulation at the membrane surface. As a result, the NF/RO process should be operated with high external mass transfer coefficient. Based on the rejection prediction in this study, the external mass transfer coefficient should be set at 300 μm/s. Then the concentration polarization factor β will be 1.07 (Re = 1,900), which can meet the recommendation requirement (1.2 - 1.3) for different water qualities [34].

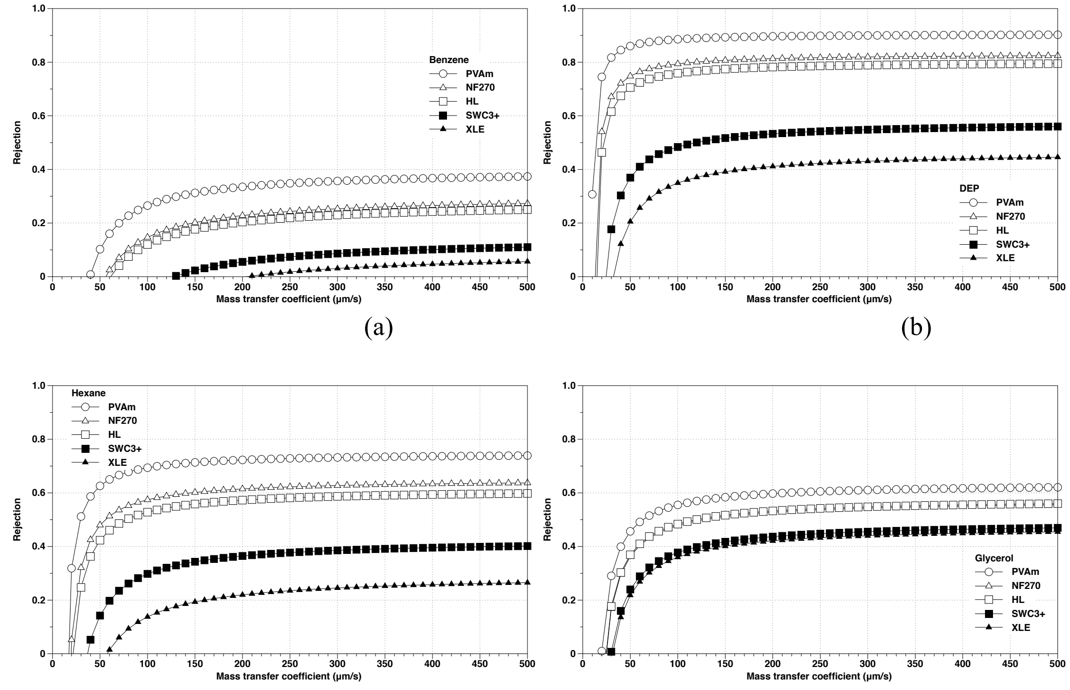

(a) (b)

(c) (d)

Figure 3.4. Predicted rejection of benzene (a), DEP (b), hexane (c) and glycerol (d) as a function of external mass transfer coefficient.

3.4.3.2 Effect of membrane structural properties

3.4.3.2.1 Membrane thickness

The membrane thickness here is defined as membrane selective layer (polyamide or PVA) effective thickness. The assumption is that the support layer (usually is made of polysulfone) of NF/RO membrane has no contribution to organic solute rejection in this study. To investigate the effect of membrane thickness on solute rejection, various membrane selective layer thickness values, which are range from 40 nm to 300 nm [33, 34], were fitted into the transport model. The solute prediction results were shown in **Figure 3.5**. When the membrane film thickness is substantially increased, the solute rejection increases as well. It is important to notice that the solute rejection dependence on film thickness becomes less significant after the film thickness reaches certain value (critical thickness). The prediction trend here is similar as some experimental study [35]. The explanation for this trend is the solute molecule will experience longer diffusion pass length when it travels through a thicker film. At the same time, the solute internal mass transfer resistance also increases. So the solute rejection will increase as the film thickness increases. For all the solutes used in this study, membrane with a 200 nm thick selective layer is preferred for solute rejection.

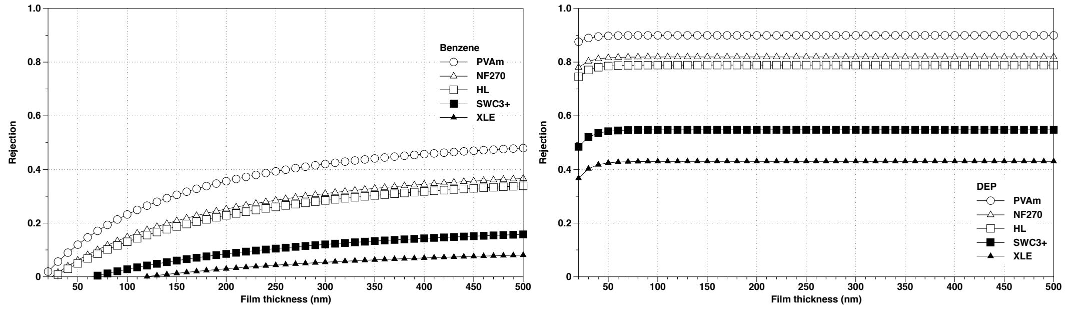

(a) (b)

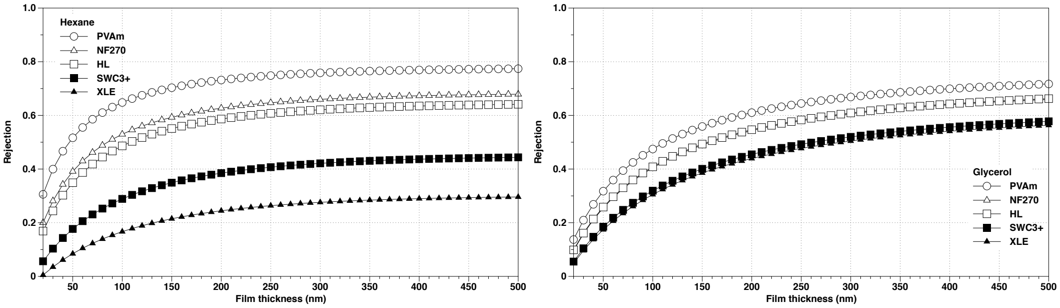

(c) (d)

Figure 3.5. Predicted rejection of benzene (a), DEP (b), hexane (c) and glycerol (d) as a function of membrane thickness.

3.4.3.2.2 Membrane pore size

The solute-membrane partition coefficient is dependent on the ratio (λ) of solute size to membrane pore size, which represents the size exclusion effects. NF/RO membranes, which are used for separation at molecule level, are usually called as non-porous membranes. However, the void phase or free volume of NF/RO membranes can be regarded as cylindrical pores whose radius will be in the range of 0.2 – 1.0 nm [36-38]. The membrane pore size can be characterized by fitting the experimental solute rejection data to transport model. In this study, the solutes rejection by the membranes was predicted by varying the membrane pore size.

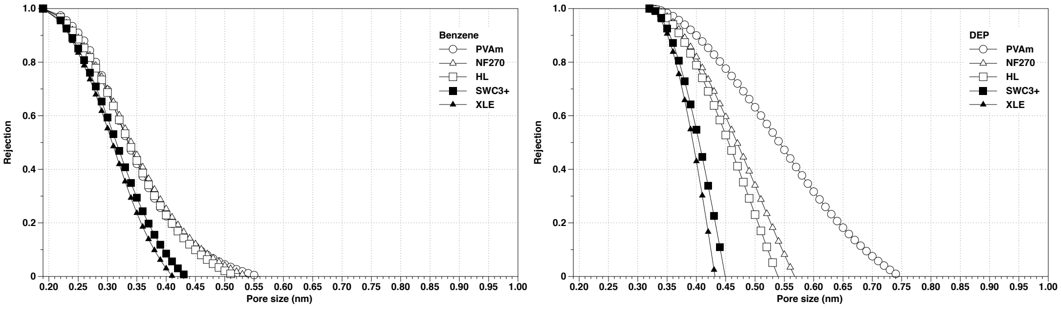

(a) (b)

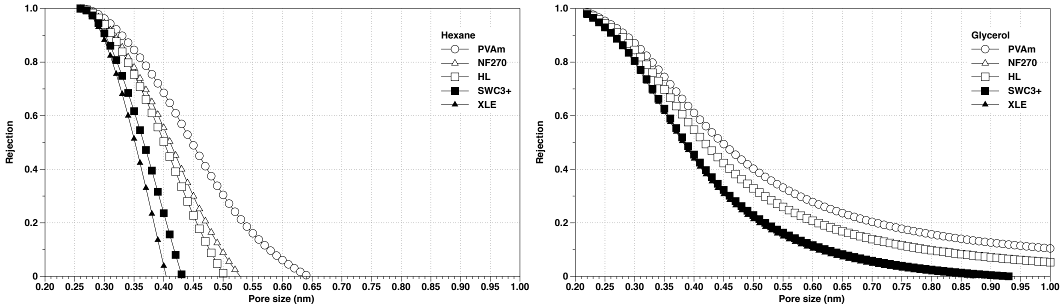

(c) (d)

Figure 3.6. Predicted rejection of benzene (a), DEP (b), hexane (c) and glycerol (d) as a function of membrane pore size.

As the results shown in **Figure 3.6**, the effect of membrane pore size on solute rejection is dramatic, especially for the cases when solute-membrane interaction free energy is negative (benzene, DEP and Hexane). The solute rejection drops because the solutes travel more easily through the pore when the pore is more open (larger pore size). The area of membrane pore wall will also increase as pore size increases. The attractive interaction ($\Delta G_s < 0$) between solute and membrane pore wall will further enhance the decrease of solute rejection. The results suggest that in order to achieve higher solute rejection, the membrane should be engineered with small pore.

3.4.3.2.3 Membrane porosity

Polymeric membranes are composited by two phases: a solid polymer phase occupied by the polymer chains and branches, and a void phase (free volume). As indicated previously, the membrane free volume provides a route for molecule to diffuse through the membrane. The fraction of free volume is referred to membrane porosity. For dense membrane (NF/RO), the membrane porosity is usually in the range of 0.01 – 0.10. Solutes rejection as a function of membrane porosity was shown in **Figure 3.7**. The solute rejection decreased as the membrane porosity decreased, especially there would be almost no rejection for benzene by RO membrane if the membrane porosity was as high as 0.06. However, the DEP rejection by membrane is almost constant when the membrane porosity is the only variable. When the membrane porosity increased, the fraction of membrane free volume also increased. According to the free volume theory, the mobility of solute in polymeric membrane, M_s is defined as [30]:

$$M_s = A\exp(-\frac{B}{\varepsilon}) \tag{3.28}$$

where A and B are constants ,which are independent of the solute concentration and temperature, but dependent only on the solute size. **Eqn. 3.27** indicates that solute mobility will increase as the membrane porosity increases. The increase in solute mobility will also reduce the solute rejection by membrane. Based on the results shown in this study, a dense (low porosity) membrane is favored for solute rejection.

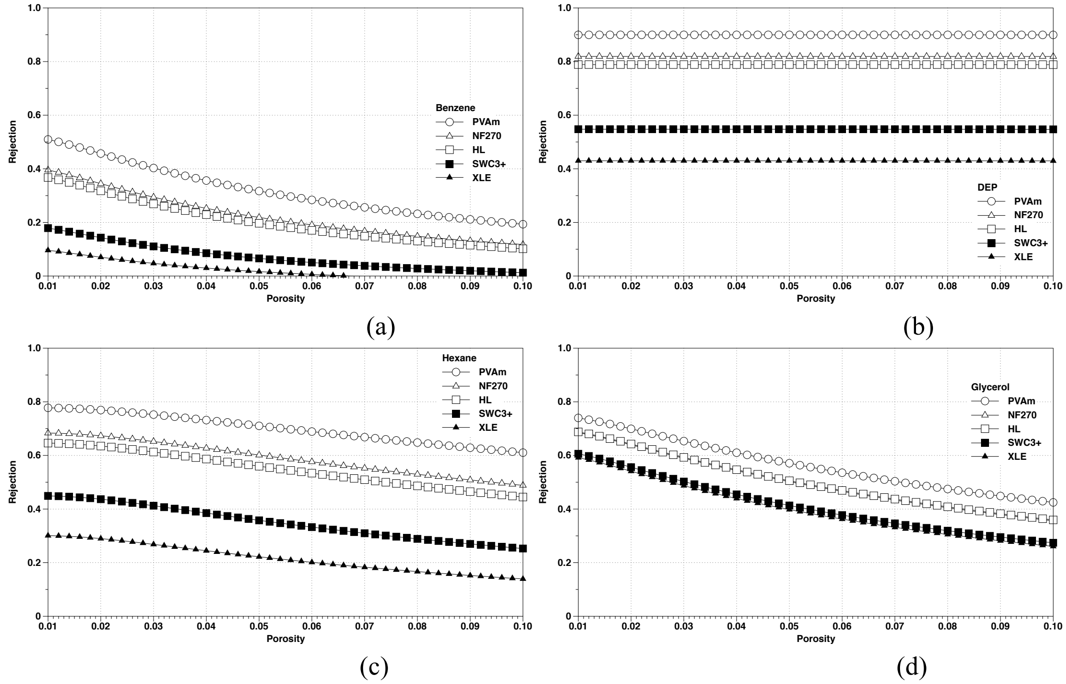

(a) (b)

(c) (d)

Figure 3.7. Predicted rejection of benzene (a), DEP (b), hexane (c) and glycerol (d) as a function of membrane porosity.

3.4.4 Implications on membrane development

Both specific water flux and solute rejection vary dramatically with λ, $\Delta x/\varepsilon$, and ΔG (**Fig. 3.8**). Variations in λ and $\Delta x/\varepsilon$ produce opposite trends for specific J_w and R_o. If one wants to maximize J_w, a membrane should have small $\Delta x/\varepsilon$ and large r_p; however, R_o will be sacrificed. The only option to optimize both specific J_w and R_o is to select a membrane material that exhibits large positive ΔG_s and large negative ΔG_w. For apolar solutes removal, this can be achieved by selecting a hydrophilic (polar) membrane. However, to remove a hydrophilic solute, it is hard to find a membrane material with both large positive ΔG_s and large negative ΔG_w, because solid materials are predominantly monopolar electron-donors [39]. These results demonstrate how understanding the role of structural and chemical properties of the membrane on its performance can help inform the materials engineering process.

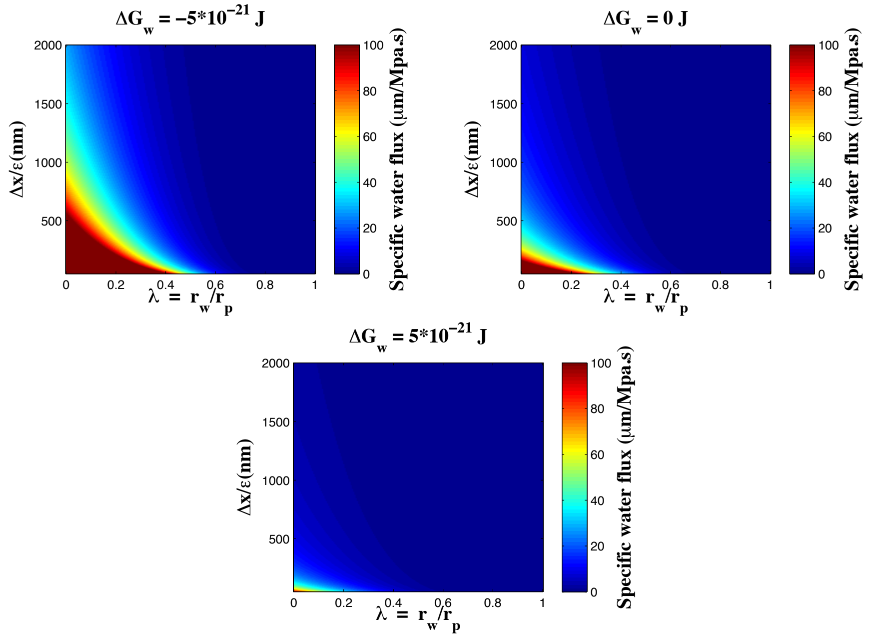

(a)

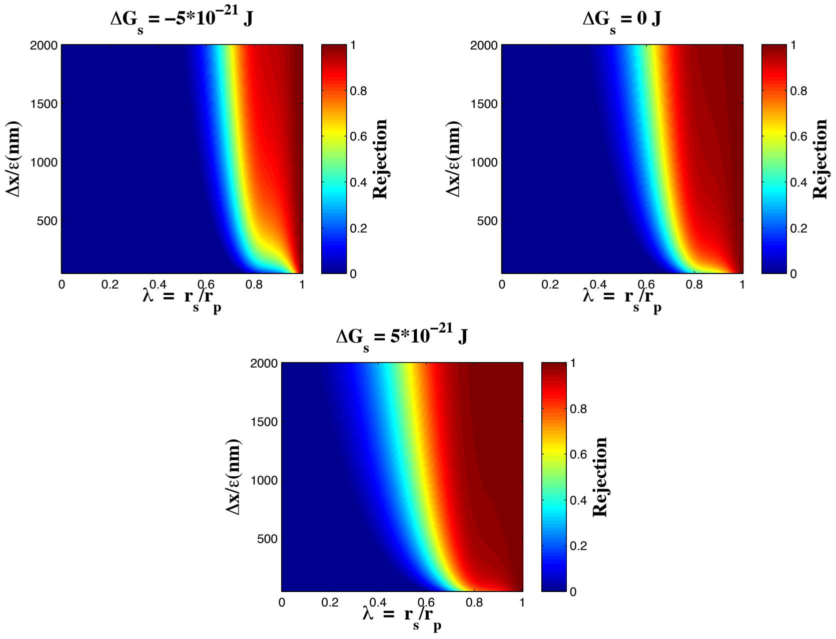

$\Delta G_s = -5*10^{-21}$ J
$\Delta G_s = 0$ J
$\Delta G_s = 5*10^{-21}$ J
Δx/ε(nm)
2000
1500
1000
500
0
0.2
0.4
0.6
0.8
1
$\lambda = r_s/r_p$
Rejection

(b)

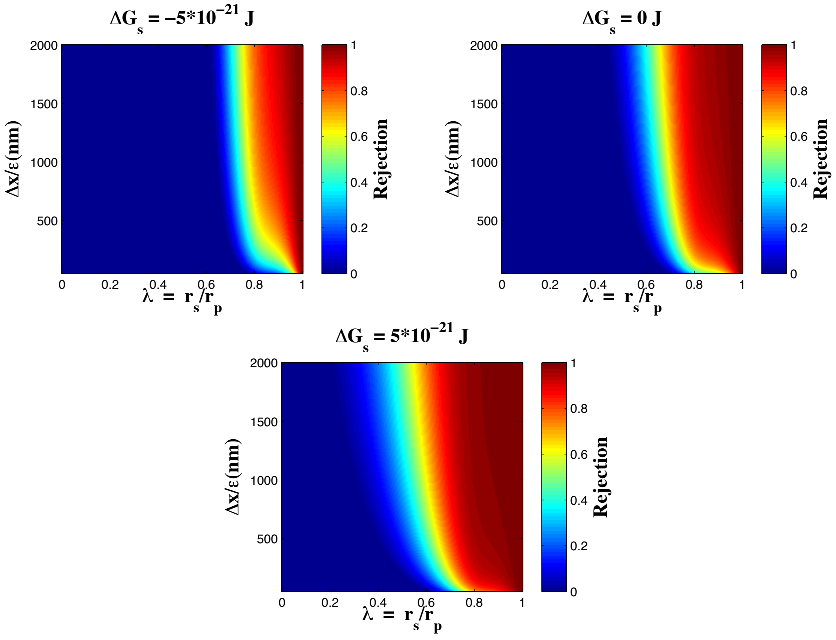

$\Delta G_s = -5*10^{-21}$ J
$\Delta G_s = 0$ J
$\Delta G_s = 5*10^{-21}$ J
Δx/ε(nm)
2000
1500
1000
500
0
0.2
0.4
0.6
0.8
1
$\lambda = r_s/r_p$
Rejection

(c)

Figure 3.8. Illustration of effect of physical parameters (λ and $\Delta x/\varepsilon$) and energetic interactions (ΔG) on (a) membrane specific water flux (**Eqn. 3.8**) and solute rejection based on (b) the improved solution-diffusion model (**Eqn. 3.18**) and (c) the convection-diffusion-affinity model (**Eqn. 3.21**). ($D_w = 2.2\times10^{-9}$ m^2/s, $D_s = 1.2\times10^{-9}$ m^2/s, $k_f = 1\times10^{-4}$ m/s, $T = 293$ K, $J_w = 1\times10^{-5}$ m/s).

3.5 Conclusions

In general, model predictions agree well with experimental data suggesting the model captures the phenomenological behavior of commercial NF/RO membranes for separations. The model suggests the "effective pore size" may be on the order of 0.24 to 0.35 nm and the "effective diffusion path length" (i.e., barrier layer thickness) may be on the order of 10 to 20 nm; model-derived pore sizes are consistent with literature reported values for the same membranes, but thicknesses are an order of magnitude less than what is historically related to polyamide coating film thickness. These new insights provide a framework for the creation of next-generation NF/RO membrane structures specifically targeting emerging trace organic contaminants of concern for human health and environmental protection.

The model was employed to predict uncharged organic solutes rejection by commercial available polyamide membranes and laboratory hand-casting PVA membranes. The results reported here confirmed previous studies that the membrane solute rejection strongly depends on the ratio of solute size to membrane pore size and solute-membrane interaction free energy. Moreover, the dependences of operation parameters, membrane structure parameters and solute properties were also clearly presented by the modeling prediction. With given membranes, applying optimal operation condition (permeate flux, mass transfer coefficient) can enhance the solute rejection. These results suggest it is possible and important to fine-tune the surface tension of membrane and membrane structure (pore size, porosity, thickness) to achieve high selectivity for certain solute.

3.6 References

[1] M.R. Boleda, K. Majamaa, P. Aerts, V. Gomez, M.T. Galceran, F. Ventura, Removal of drugs of abuse from municipal wastewater using reverse osmosis membranes, Desalin Water Treat, 21 (2010) 122-130.

[2] D. Dolar, K. Kosutic, D.M. Pavlovic, B. Kunst, Removal of emerging contaminants of industrial origin by NF/RO - A pilot scale study, Desalin Water Treat, 6 (2009) 197-203.

[3] J.L. Cartinella, T.Y. Cath, M.T. Flynn, G.C. Miller, K.W. Hunter, A.E. Childress, Removal of natural steroid hormones from wastewater using membrane contactor processes, Environ Sci Technol, 40 (2006) 7381-7386.

[4] F.S. Kegel, B.M. Rietman, A.R.D. Verliefde, Reverse osmosis followed by activated carbon filtration for efficient removal of organic micropollutants from river bank filtrate, Water Sci Technol, 61 (2010) 2603-2610.

[5] M.E. Williams, J.A. Hestekin, C.N. Smothers, D. Bhattacharyya, Separation of organic pollutants by reverse osmosis and nanofiltration membranes: Mathematical models and experimental verification, Ind Eng Chem Res, 38 (1999) 3683-3695.

[6] B. Van der Bruggen, C. Vandecasteele, Removal of pollutants from surface water and groundwater by nanofiltration: overview of possible applications in the drinking water industry, Environ Pollut, 122 (2003) 435-445.

[7] S. Loeb, S. Sourirajan, Sea Water Demineralization by Means of an Osmotic Membrane, in: Saline Water Conversion?II, AMERICAN CHEMICAL SOCIETY, 1963, pp. 117-132.

[8] T. Matsuura, S. Sourirajan, Reverse-Osmosis Transport through Capillary Pores under the Influence of Surface Forces, Ind Eng Chem Proc Dd, 20 (1981) 273-282.

[9] K.S. Spiegler, O. Kedem, Thermodynamics of Hyperfiltration (Reverse-Osmosis) - Criteria for Efficient Membranes, Cc/Eng Tech Appl Sci, (1983) 16-16.

[10] S. Bhattacharjee, A. Sharma, P.K. Bhattacharya, Estimation and influence of long range solute. Membrane interactions in ultrafiltration, Ind. Eng. Chem. Res., 35 (1996) 3108.

[11] A.R.D. Verliefde, E.R. Cornelissen, S.G.J. Heijman, E.M.V. Hoek, G.L. Amy, B.V.d. Bruggen, J.C. van Dijk, Influence of Solute−Membrane Affinity on Rejection of Uncharged Organic Solutes by Nanofiltration Membranes, Environ Sci Technol, 43 (2009) 2400-2406.

[12] G.M. Geise, H.B. Park, A.C. Sagle, B.D. Freeman, J.E. McGrath, Water permeability and water/salt selectivity tradeoff in polymers for desalination, Journal of Membrane Science, 369 (2011) 130-138.

[13] D.R. Paul, Reformulation of the solution-diffusion theory of reverse osmosis, J Membrane Sci, 241 (2004) 371-386.

[14] R.W. Baker, Membrane Transport Theory, in: Membrane Technology and Applications, John Wiley & Sons, Ltd, 2004, pp. 15-87.

[15] B. Kunst, K. Košutić, Removal of Emerging Contaminants in Water Treatment by Nanofiltration and Reverse Osmosis
Emerging Contaminants from Industrial and Municipal Waste, in: D. Barceló, M. Petrovic (Eds.), Springer Berlin / Heidelberg, 2008, pp. 103-125.

[16] W.M. Deen, Hindered transport of large molecules in liquid-filled pores, AIChE J., 33 (1987) 1409.

[17] W.R. Bowen, A.W. Mohammad, N. Hilal, Characterisation of nanofiltration membranes for predictive purposes - Use of salts, uncharged solutes and atomic force microscopy, J Membrane Sci, 126 (1997) 91-105.

[18] J.D. Jeon, S.J. Kim, S.Y. Kwak, H-1 nuclear magnetic resonance (NMR) cryoporometry as a tool to determine the pore size distribution of ultrafiltration membranes, J Membrane Sci, 309 (2008) 233-238.

[19] N. Hilal, H. Al-Zoubi, N.A. Darwish, A.W. Mohammad, Characterisation of nanofiltration membranes using atomic force microscopy, Desalination, 177 (2005) 187-199.

[20] S.H. Kim, S.Y. Kwak, T. Suzuki, Positron annihilation spectroscopic evidence to demonstrate the flux-enhancement mechanism in morphology-controlled thin-film-composite (TFC) membrane, Environ Sci Technol, 39 (2005) 1764-1770.

[21] Y.C. Jean, W.S. Hung, C.H. Lo, H. Chen, G. Liu, L. Chakka, M.L. Cheng, D. Nanda, K.L. Tung, S.H. Huang, K.R. Lee, J.Y. Lai, Y.M. Sun, C.C. Hu, C.C. Yu, Applications of positron annihilation spectroscopy to polymeric membranes, Desalination, 234 (2008) 89-98.

[22] H.M. Chen, W.S. Hung, C.H. Lo, S.H. Huang, M.L. Cheng, G. Liu, K.R. Lee, J.Y. Lai, Y.M. Sun, C.C. Hu, R. Suzuki, T. Ohdaira, N. Oshima, Y.C. Jean, Free-volume depth profile of polymeric membranes studied by positron annihilation spectroscopy: Layer structure from interfacial polymerization, Macromolecules, 40 (2007) 7542-7557.

[23] G.Z. Ramon, M.C.Y. Wong, E.M.V. Hoek, Transport through composite membrane, part 1: Is there an optimal support membrane?, J Membrane Sci, 415 (2012) 298-305.

[24] G.Z. Ramon, E.M.V. Hoek, Transport through composite membranes, part 2: Impacts of roughness on permeability and fouling, J Membrane Sci, 425 (2013) 141-148.

[25] J. Wang, Y. Mo, S. Mahendra, E.M.V. Hoek, Effects of Water Chemistry on Structure and Performance of Polyamide Composite Membranes, Journal of Membrane Science, submitted (2013).

[26] C.J. van Oss, Development and applications of the interfacial tension between water and organic or biological surfaces, Colloids Surf., B, 54 (2007) 2.

[27] P.M. Bungay, H. Brenner, The motion of a closely-fitting sphere in a fluid-filled tube, International Journal of Multiphase Flow, 1 (1973) 25.

[28] V. Silva, P. Pradanos, L. Palacio, A. Hernandez, Alternative pore hindrance factors: What one should be used for nanofiltration modelization?, Desalination, 245 (2009) 606-613.

[29] W. Korner, U. Bolz, W. Sussmuth, G. Hiller, W. Schuller, V. Hanf, H. Hagenmaier, Input/output balance of estrogenic active compounds in a major municipal sewage plant in Germany, Chemosphere, 40 (2000) 1131-1142.

[30] F. Peng, Z. Jiang, E.M.V. Hoek, Tuning the molecular structure, separation performance and interfacial properties of poly(vinyl alcohol)-polysulfone interfacial composite membranes, J Membrane Sci, 368 (2011) 26-33.

[31] S. Bhattacharjee, A. Sharma, P.K. Bhattacharya, Estimation and influence of long range solute. Membrane interactions in ultrafiltration, Ind Eng Chem Res, 35 (1996) 3108-3121.

[32] v.O. Carel Jan, Development and applications of the interfacial tension between water and organic or biological surfaces, Colloids and Surfaces B: Biointerfaces, 54 (2007) 2-9.

[33] F.B. Peng, X.F. Huang, A. Jawor, E.M.V. Hoek, Transport, structural, and interfacial properties of poly (vinyl alcohol)-polysulfone composite nanofiltration membranes, J Membrane Sci, 353 (2010) 169-176.

[34] J. Kucera, Reverse Osmosis: Design, Processes, and Applications for Engineers, Wiley, 2011.

[35] S. Azari, M. Karimi, M.H. Kish, Structural Properties of the Poly(acrylonitrile) Membrane Prepared with Different Cast Thicknesses, Ind Eng Chem Res, 49 (2010) 2442-2448.

[36] Y. Kiso, K. Muroshige, T. Oguchi, M. Hirose, T. Ohara, T. Shintani, Pore radius estimation based on organic solute molecular shape and effects of pressure on pore radius for a reverse osmosis membrane, J Membrane Sci, 369 (2011) 290-298.

[37] K. Kosutic, L. Kastelan-Kunst, B. Kunst, Porosity of some commercial reverse osmosis and nanofiltration polyamide thin-film composite membranes, J Membrane Sci, 168 (2000) 101-108.

[38] K. Kosutic, B. Kunst, Removal of organics from aqueous solutions by commercial RO and NF membranes of characterized porosities, Desalination, 142 (2002) 47-56.

[39] C.J. van Oss, Chapter Four Determination of Interfacial Tensions between Water and Other Condensed-Phase Materials, in: J.v.O. Carel (Ed.) Interface Science and Technology, Elsevier, 2008, pp. 51-57.

CHAPTER 4

EFFECTS OF WATER CHEMISTRY ON STRUCTURE AND PERFORMANCE OF POLYAMIDE COMPOSITE MEMBRANES

4.1 Introduction

The main goal of this chapter was to expand upon the extended solution-diffusion model of Verliefde et al. [1] to more accurately quantify changes in membrane structure and solute-solvent-membrane interactions due to changes in feed water chemistry (ionic strength, pH and divalent cation content). Ultimately, this work provides new structure-performance insights into polyamide NF/RO membrane separation performance. Herein, the extended solution-diffusion model accounts for both water flux and (neutral) solute rejection. Therefore, we provide two equations that allow one to directly solve for the two membrane structural descriptors (i.e., effective pore radius and structure factor) by properly fitting to experimentally observed flux and rejection data.

4.2 Materials and Methods

4.2.1. Membranes and chemicals

Representative polyamide NF and RO membranes (NF90, NF270, BW-XLE; Dow Film Tec Corp., Minneapolis, Minnesota, USA) were received as flat sheet samples and stored in laboratory deionized water at 4 °C upon receipt. Chemical agents used to adjust feed water chemistry were all analytical grade (Fisher Scientific, Pittsburgh, Pennsylvania, USA). Ethylene glycol (EG, Sigma-Aldrich, St. Louis, MO) was used as a model neutral solute in performance tests. Key physical-chemical properties of EG are provided in **Table 4.1**.

Table 4.1 Physic-chemical properties of ethylene glycol.

Chemical formula	Molecular weight (g/mol)	Stokes radius (nm)	Diffusivity (cm^2/s)	pK_a
$C_2H_6O_2$	62	0.184*	1.16×10^{-5} [2]	14.2 [3]

* Calculated by Stokes-Einstein equation in [4]

4.2.2. Membrane performance experiments

The separation performance of NF and RO membranes was evaluated in a bench scale cross-flow membrane filtration system equipped with six parallel membrane cells, each with an effective membrane area of 19.4 cm^2 (2.54 cm width, 7.62 cm length) and cross-flow channel height of 1 mm. A detailed description of the test apparatus is previously published [5]. Water flux was determined at 20 °C and applied pressures between 0.21 to 1.72 MPa (30 to 250 psi). The cross-flow rate was set at 3.46×10^{-5} $m^3\cdot s^{-1}$ (0.55 $Gal\cdot min^{-1}$) in all experiments providing a cross-flow Reynolds number of 1,900 accounting for a mesh feed spacer placed in the feed channel. The external mass transfer coefficient was 2.42×10^{-4} $m\cdot s^{-1}$, producing a concentration polarization factor in the range of 1.04 – 1.13 for permeate fluxes in the range of 1 to 30 $\mu m\cdot s^{-1}$. Permeate flux was measured by a digital flow meter (Optiflow 1000, Agilent Technology, Forster City, CA) placed on the permeate line from each cross-flow membrane module.

Prior to testing, all the membranes were compacted with 0.056 µS/cm deionized water at 2.76 MPa (400 psi) and 20 °C for 18 hours. After water flux measurements, the same membranes were used to characterize solute rejection under various water chemistries. Feed water ionic strength was adjusted by adding various amounts of NaCl. Feed water pH was adjusted with 1M NaOH and 1M HCl solutions. $CaCl_2$ and $MgCl_2$

was added to provide divalent cation content. New sets of membranes were used for each series of experiments. EG was spiked into deionized water at 20 mg carbon·L^{-1}. EG rejection was found by measuring total organic carbon in feed and permeate solutions. Salt rejection was evaluated by measuring conductivities of feed and permeates solution. The addition of osmotic pressure due to salt rejection had been taken into account when calculating membrane water permeability. During the rejection experiments, feed pressure was varied from 0.21 to 1.72 MPa, while temperature (20 °C) and external mass transfer coefficient (2.42×10^{-4} m/s) were kept constant. In order to eliminate the effects of initial adsorption of solute onto the membrane surface and into membrane inner structure, feed solution was filtered through all the membranes for 24 hours before rejection measurements were obtained.

4.2.3. Membrane and solute surface tension characterization

The membrane and solute interfacial tensions and water/solute-membrane interaction energies were determined from measured contact angles using an automated contact angle goniometer (DSA10, Krüss GmbH, Hamburg, Germany). At least twelve equilibrium contact angles at different locations were measured for each sample. The details of contact angle measurements were described in previous publication [6]. Contact angles measurement for different water chemistries (polar liquid), diiodomethane (apolar liquid) and EG (polar liquild) enables determination of surface tension components for membranes using the extended Young-Dupré equation [6]

$$\gamma_w^T\left(1+\frac{cos\theta}{r}\right)=2\left(\sqrt{\gamma_m^{LW}\gamma_w^{LW}}+\sqrt{\gamma_m^+\gamma_w^-}+\sqrt{\gamma_m^-\gamma_w^+}\right) \tag{4.1}$$

where θ is the contact angle formed between the droplet of liquid and membrane surface, *r* is the roughness area ratio (i.e. the ratio of actual surface area for a rough surface to the planar area) [7]. The membrane surface roughness was analyzed form atomic force microscopy (AFM) measurement and an average of six measurements were used to produce the final roughness data (**Table 4.2**).

Table 4.2 Roughness of membranes.

Membrane	***R_a*** **(nm)**	***R_q*** **(nm)**	***R_m*** **(nm)**	***SAD*** **(%)**
NF270	3.2 ± 1.6	4.0 ± 1.6	54 ± 20	0.4 ± 0.2
NF90	31.2 ± 5.4	40.5 ± 7.0	401 ± 75	19.1 ± 5.0
XLE	44.1 ± 10.3	58.2 ± 14.6	580 ± 88	33.6 ± 5.7

R_a: average deviation (above or below) the mean plane.
R_q: RMS deviation or z-data standard deviation.
R_m: maximum deviation between largest + and - z-values, spread of distribution.
SAD: surface area difference, increase in surface area over projected flat plate area (r = 1+ *SAD*).

The surface tension components for EG and the liquids are given in **Table 4.3** [8]. These data and measured contact angles were used to calculate interfacial free energies.

Table 4.3 Surface tension parameters of liquids.

Chemicals	γ_s^T **(mJ/m^2)**	γ_s^{LW} **(mJ/m^2)**	γ_s^+ **(mJ/m^2)**	γ_s^- **(mJ/m^2)**
EG	48	29	1.92	47
Diiodomethane	50.8	50.8	0	0
Water	72.8	21.8	25.5	25.5

4.3 Results and Discussion

4.3.1 Effects of water chemistry on membrane performance

4.3.1.1. Feed ionic strength

Membrane water permeability and solute rejection (salt and EG) was evaluated while changing the ionic strength of feed water. Membrane water permeability was measured at the same operation conditions and normalized to water permeability measured with DI water as feed. And all solute rejections were measured at the same permeate water flux (~13 μm/s). As shown in **Figure 4.1a**, for all the membranes, membrane water permeability decreased as ionic strength in feed water increased. The trend here was the same as the experimental results published by Freger [9] and Braghetta et al. [10]. Among the three commercial membranes, the loss of water permeability for NF270 (up to 33 %) was less significant than for NF90 (up to 46 %) and XLE (up to 47 %). It is important to notice that, for all three membranes, their initial pure water permeability was almost fully recovered within experimental error, so the effect of solution water chemistry on these membranes appeared fully reversible.

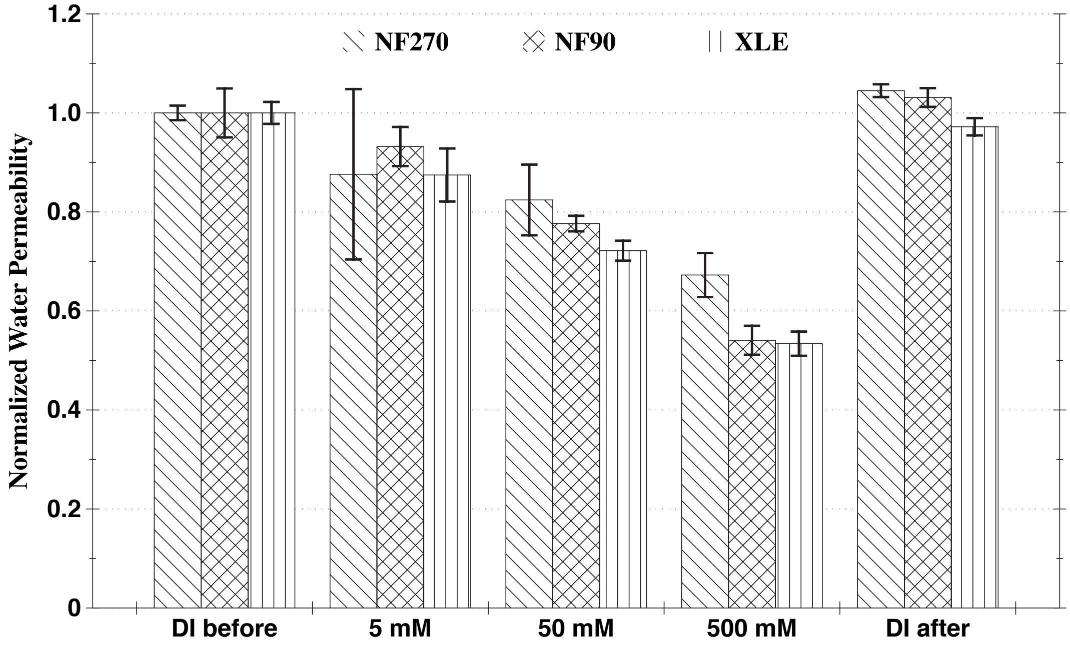

(a)

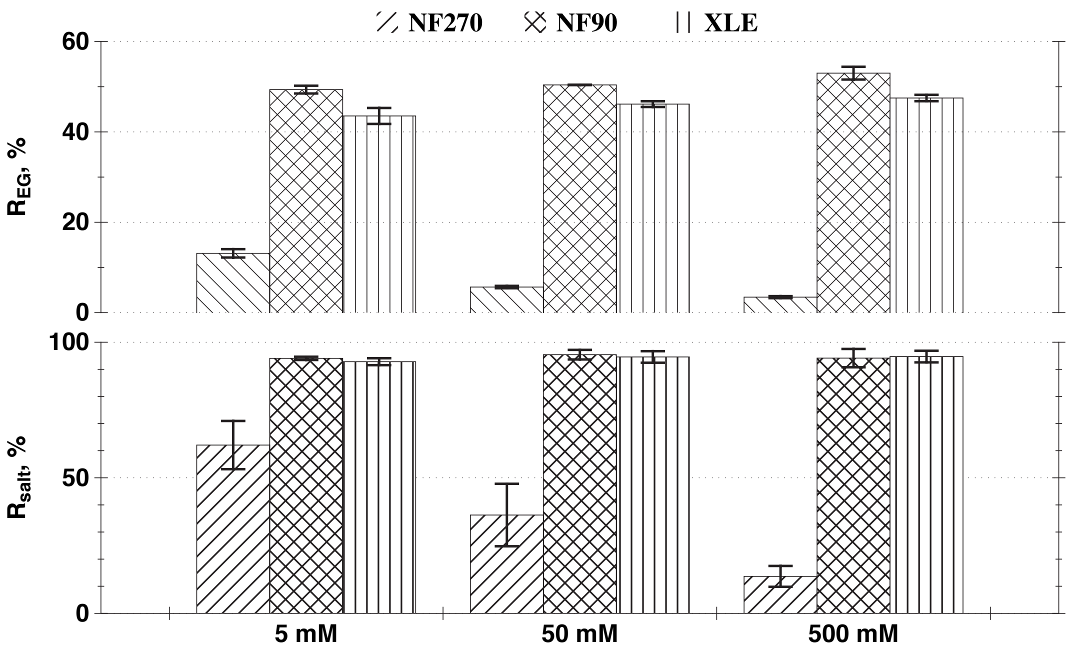

(b)

Figure 4.1. Experimental data illustrating the effects of ionic strength on (a) water permeability normalized against measured with deionized water and (b) solute (NaCl and EG) rejection. Experimental conditions: cross-flow Re 1,900, feed temperature 20 °C, and pH 6.0±0.2. Solute rejection data reported for water flux about 13 μm/s.

Figure 4.1b shows the salt rejection for the three membranes at feed concentrations ranging from 5 mM to 500 mM. For NF90 and XLE membranes, there is no significant difference in salt rejection while varying feed salt concentration. However, NaCl retention by NF270 decreased with increasing NaCl concentration in the feed. Mazzoni et al. reported salt rejection deceases as the salt concentration increases for Desal-5 DK membranes [11]. The charge screening effect of the counter-ions on the membrane charge sites is stronger when the feed salt concentration increases. Meanwhile, the electrostatic repulsive interaction between membrane and salt ion will decrease, which will cause the decrease of salt retention [12]. The results in this study suggest that, for dense membrane NF90 and XLE, the charge screening effect in salt rejection deduction is less significant as for NF270 membrane.

For NF90 and XLE membranes, EG rejection increased with increasing solution ionic strength from 5 mM to 500 mM. Similar results have been reported by Braghetta et al., in which increased PEG rejection by NF membrane at high ionic strength was observed [10]. However, for NF270, EG rejection decreased with ionic strength from 5 mM to 500 mM. These results were consistent with results of studies on N-Nitrosodimethylamine (NDMA) rejection by ESPA3 membrane conducted by Steinle-Darling et al. [13]. Luo et al. also found that glucose retention for NF270 membrane decreased with increasing salt concentration [14].

4.3.1.2 Feed pH

Membrane water permeability was tested with different feed solution pH and normalized to water permeability measured with DI water as feed, as shown in **Figure 4.2a**. For NF270, membrane water permeability increased with pH from 3 to 9 and decreased from pH 9 to 11. For NF90 and XLE, membrane water permeability increased with pH from 3 to 7, then decreased with pH from 7 to 11. However, membrane water permeability of NF 90 and XLE were less sensitive to solution pH than NF 270. As same as varying solution ionic strength, membrane water permeability of all three membranes could also be recovered.

Figure 2b shows the effect of feed solution pH on salt rejection for the tested membranes. NF90 and XLE membrane are less pH sensitive in salt retention when pH is varied from 5 to 11. However, when solution pH decreased to 3, NF90 and XLE membrane salt rejection also decreased. For NF270, salt rejection first decreased with feed pH and then increased, which is similar with results in Kim et al. [15] and Xu et al. [16]. When feed solution pH was further increased to 11, the salt rejection deceased.

The effect of feed solution pH on EG rejection was also illustrated in **Figure 4.2b**. For all three membranes, the decrease in EG rejection was observed at a pH between 3 and 9. When the solution pH was further increased to 11, the EG rejection also increased. The trend observed here is similar with Schäfer et al., as they found the rejection of the steroid estrone by NF (TFC-SR1) and RO (TFC-S) membranes decreased when solution pH approached the pKa of estrone [17]. Also, Bellona et al. also reported their findings that rejection of ibuprofen by NF90 and NF200 membranes was the highest at pH 3, then the rejection slightly decreased at pH 5 before it increased again beyond a pH 7 [18].

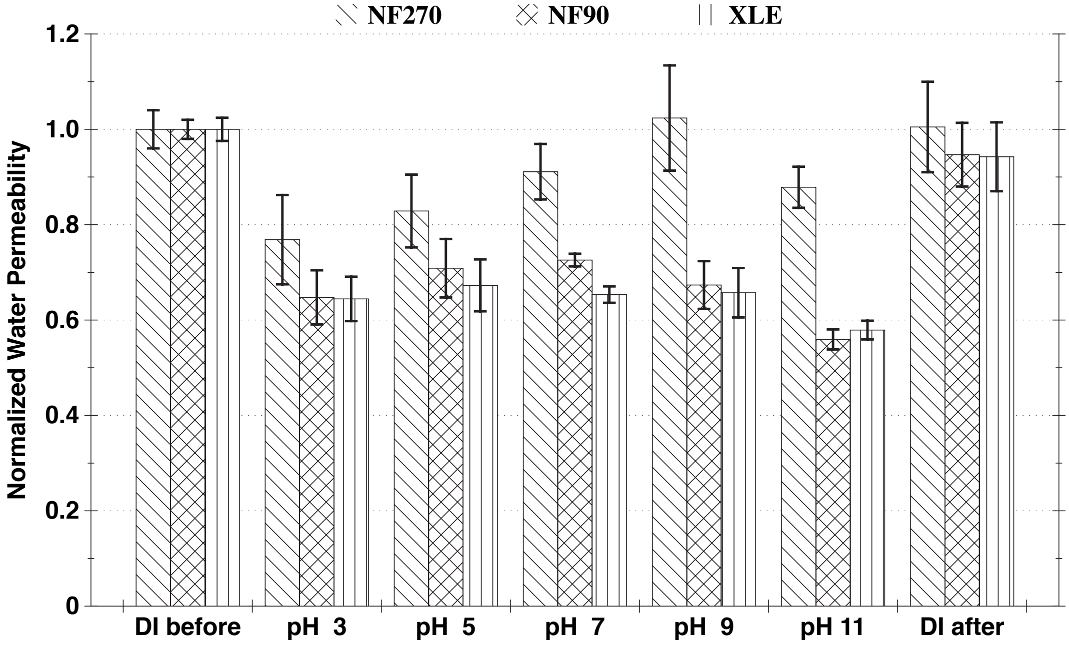

(a)

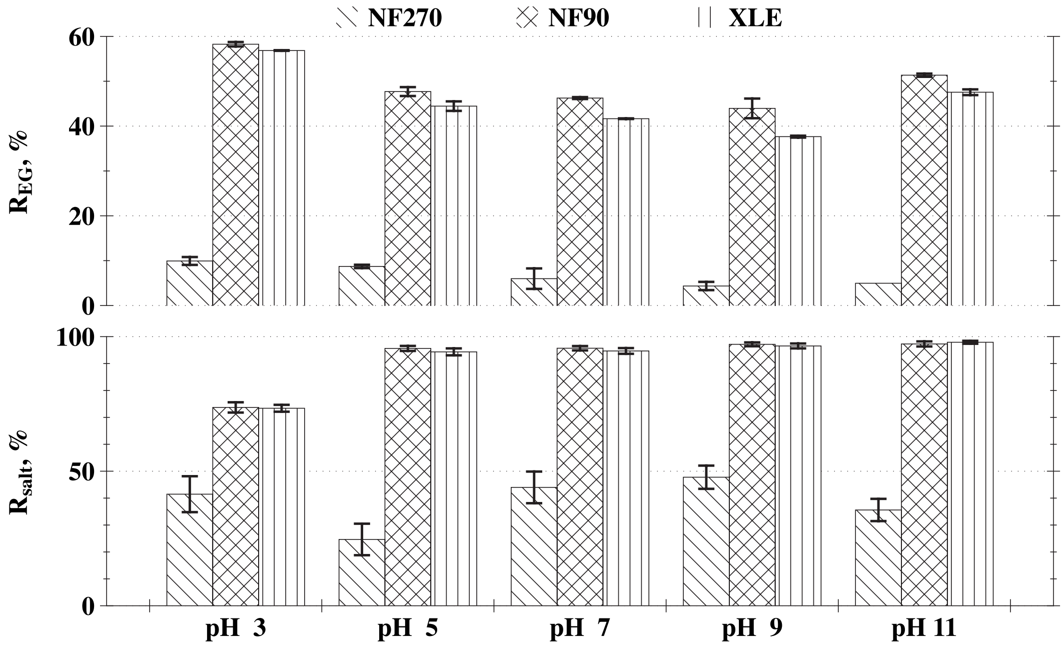

(b)

Figure 4.2. Experimental data illustrating the effects of pH on (a) water permeability normalized against measured with deionized water and (b) solute (NaCl and EG) rejection. Experimental conditions:cross-flow Re 1,900, feed temperature 20 °C, and ionic strength 50 mM. Solute rejection data reported for water flux about 13 μm/s.

4.3.1.3 Presence of divalent cations in feed

Divalent ions (e.g. Ca^{2+}, Mg^{2+}) are ubiquitous in natural waters and wastewaters. So membrane water permeability was characterized in their presence (**Figure 4.3a)** and normalized to water permeability measured with DI water as feed. For all three membranes, membrane water permeability decreased with Ca^{2+} or Mg^{2+} in the feed water. And the loss of membrane water permeability (30 to 40 %) was more than that when the same ionic strength of NaCl existing in the feed (20 to 30 %). Membrane water permeability reduction percentage of three tested membranes were almost the same for each cation. However, the membrane water permeability under $MgCl_2$ feed solution was lower than membrane water permeability under $CaCl_2$ feed for all membranes. It is interesting to point out that the DI water permeability could not fully recovered for NF90 and XLE membranes (80 to 95 %). Based on the results, magnesium ion appeared to cause more water flux loss for all membranes than calcium ion at the same ionic strength. As shown in **Figure 3b**, there is no noteworthy difference in $CaCl_2$ and $MgCl_2$ rejection for NF90 and XLE membranes. $MgCl_2$ rejection is slightly higher than $CaCl_2$ rejection for NF270 due to the larger hydrated radius of Mg^{2+} ion [19].

EG rejection was also decreased with divalent cation content in the feed water **(Figure 4.3b)**. Also, EG rejection by all three membranes was slightly higher for Mg^{2+} than Ca^{2+}, although the differences were not significant. For comparison, the results of EG rejection with 50 mM NaCl as feed solution were replotted here. It should be noted that, for NF90 and XLE membranes, divalent cations in feed solution caused more reduction in EG rejection than monovalent cations. Verliefde et al. studied the influence of addition of Ca^{2+} into feed solution on neutral pharmaceutical compounds rejection by Desal HL and Trisep TS80 membranes. Compared to the solute rejection in NaCl electrolytes, both membranes showed lower rejection for most of the neutral solute after adding 10 mM Ca^{2+} into feed solution [20]. However, for NF270 membrane, the EG rejection was smaller in feed solution with monovalent cations compared to with divalent cations.

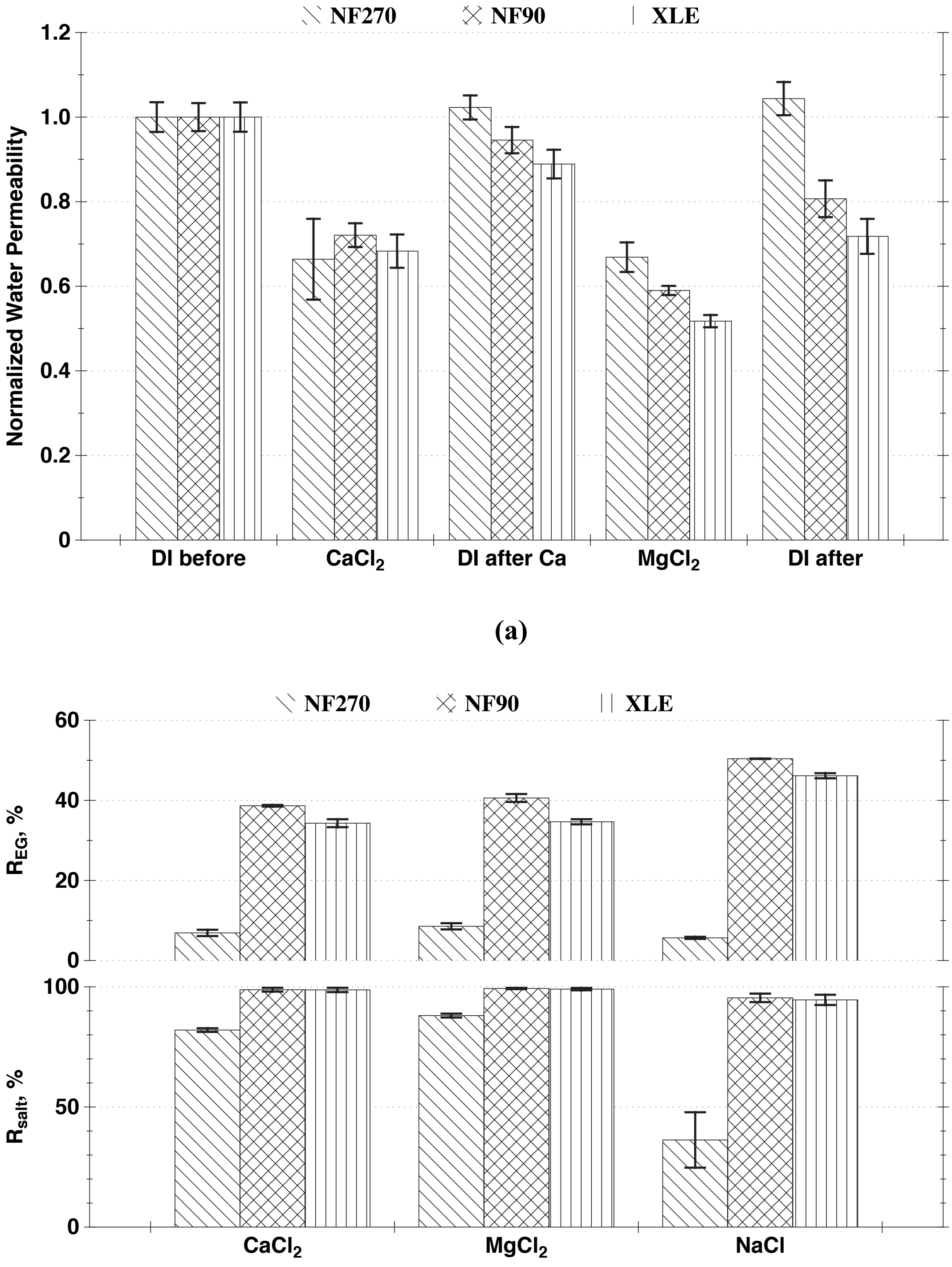

(a)

(b)

Figure 4.3. Experimental data illustrating the effects of divalent cations on (a) water permeability normalized against measured with deionized water and (b) solute rejection

($CaCl_2$, $MgCl_2$ and EG, NaCl rejection was plotted for comparison). Experimental conditions: cross-flow Re 1,900, feed temperature 20 °C, pH 6.0±0.2 and ionic strength 50 mM. Solute rejection data reported for water flux of about 13 µm/s.

4.3.2 Effects of water chemistry on solute-water-membrane interaction energy

Based on the contact angle data shown in **Table 4.4**, the electrolyte solution contact angles of all three membranes decreased with increasing ionic strength, increasing solution pH and with divalent cations (Mg^{2+}, Ca^{2+}) presenting. Solute and membrane interfacial tensions and free energies were calculated from contact angles data in **Table 4.4** using previously published methods [21]. The membrane (1)-liquid media (3) interfacial free energy, $-\Delta G_{13}$, fundamentally describes membrane surface wettability. The cohesive free energy, ΔG_{131}, which describes energetic favorability of membrane (1) interacting through a liquid media (3) (solution with various water chemistries) with itself (1), offers a quantitative description of membrane surface hydrophilicity [5]. ΔG_{13} and ΔG_{131} can be calculated according to [21]

$$\Delta G_{13} = -2\left(\sqrt{\gamma_m^{LW}\gamma_w^{LW}} + \sqrt{\gamma_m^{+}\gamma_w^{-}} + \sqrt{\gamma_m^{-}\gamma_w^{+}}\right) \tag{4.2}$$

$$\Delta G_{131} = -2\left(\sqrt{\gamma_m^{LW}} - \sqrt{\gamma_w^{LW}}\right)^2 - 4\left(\sqrt{\gamma_m^{-}\gamma_m^{+}} + \sqrt{\gamma_w^{-}\gamma_w^{+}} - \sqrt{\gamma_m^{+}\gamma_w^{-}} - \sqrt{\gamma_m^{-}\gamma_w^{+}}\right) \tag{4.3}$$

Hydrophilic membranes produce positive ΔG_{131}, while hydrophobic membranes exhibit a negative ΔG_{131} [5]. NF270 membrane was hydrophilic, while NF90 and XLE membranes were hydrophobic under the water chemistries tested in this study; all three membranes became more hydrophilic with increasing ionic strength, pH and divalent cation content increased. These results are consistent with those of Hurwitz et al. [6]

published several years ago using different samples of solvents, salts and the XLE membrane.

Water/solute-membrane interaction energy (ΔG_{mw} or ΔG_{mws}), which is the free energy difference associated with interaction of water or solute molecule in the bulk water phase compared to in the membrane phase [22], indicates the attractive or repulsive water/solute membrane interactions. If ΔG_{mw} or ΔG_{mws} is positive, a repulsive interaction between water/solute and membrane is expected. The partitioning of water/solute from water phase into membrane phase will not be favored. When ΔG_{mw} or ΔG_{mws} is negative, this suggests that there are attractive interactions between water/solute and membrane, which will result in a higher concentration of water/solute in membrane phase. The water/solute membrane interaction energies calculated based on **Eqns. 3.10 and 3.19** are plotted in **Figure 4.4**.

Table 4.4 Membrane contact angles, surface tensions and interfacial energies.

	Electrolytes	θ (°)	γ_m^{LW} (mJ/m^2)	γ_m^{+} (mJ/m^2)	γ_m^{-} (mJ/m^2)	γ_m^{AB} (mJ/m^2)	$-\Delta G_{13}$ (mJ/m^2)	$-\Delta G_{131}$ (mJ/m^2)
NF 90	**DI**	69.89	35.87	0.77	8.25	5.04	91.50	28.42
	NaCl 5mM	65.52	35.87	0.59	11.61	5.25	95.54	20.73
	NaCl 50mM	62.97	35.87	0.50	13.77	5.26	97.84	16.16
	NaCl 500mM	61.00	35.87	0.44	15.53	5.22	99.61	12.58
	NaCl 50mM, pH=3	67.66	35.87	0.68	9.90	5.18	93.60	24.52
	NaCl 50mM, pH=5	64.67	35.87	0.56	12.31	5.26	96.31	19.22
	NaCl 50mM, pH=7	62.19	35.87	0.48	14.46	5.25	98.57	14.73
	NaCl 50mM, pH=9	60.93	35.87	0.44	15.60	5.22	99.69	12.44
	NaCl 50mM, pH=11	56.26	35.87	0.31	20.04	4.96	103.68	3.95
	$MgCl_2$ 50mM	61.44	35.87	0.45	15.13	5.23	99.19	13.39
	$CaCl_2$ 50mM	64.04	35.87	0.54	12.85	5.26	96.91	18.06
NF 270	**DI**	28.25	38.94	0.20	50.28	6.41	129.78	-39.40
	NaCl 5mM	30.96	38.94	0.24	47.45	6.79	128.27	-35.56
	NaCl 50mM	26.38	38.94	0.18	52.14	6.14	130.80	-41.86
	NaCl 500mM	22.80	38.94	0.14	55.45	5.66	132.46	-46.30
	NaCl 50mM, pH=3	27.47	38.94	0.19	51.07	6.30	130.20	-40.47
	NaCl 50mM, pH=5	24.46	38.94	0.16	53.97	5.88	131.76	-44.29
	NaCl 50mM, pH=7	23.91	38.94	0.15	54.46	5.81	131.96	-45.00
	NaCl 50mM, pH=9	20.04	38.94	0.12	57.75	5.30	133.65	-49.29
	NaCl 50mM, pH=11	17.15	38.94	0.10	59.9	4.96	134.69	-52.12
	$MgCl_2$ 50mM	21.13	38.94	0.13	56.87	5.44	133.23	-48.11
	$CaCl_2$ 50mM	25.71	38.94	0.17	52.79	6.05	131.11	-42.76
XLE	**DI**	70.12	32.06	0.61	9.14	4.74	88.96	25.24
	NaCl 5mM	70.03	32.06	0.61	9.20	4.74	89.06	25.08
	NaCl 50mM	67.83	32.06	0.54	10.72	4.80	90.91	21.53
	NaCl 500mM	67.03	32.06	0.51	11.31	4.81	91.55	20.22
	NaCl 50mM, pH=3	69.85	32.06	0.61	9.32	4.75	89.25	24.77
	NaCl 50mM, pH=5	66.94	32.06	0.51	11.37	4.81	91.64	20.08
	NaCl 50mM, pH=7	62.96	32.06	0.39	14.42	4.77	94.82	13.56
	NaCl 50mM, pH=9	61.92	32.06	0.37	15.26	4.73	95.70	11.82
	NaCl 50mM, pH=11	60.34	32.06	0.33	16.55	4.66	96.92	9.23
	$MgCl_2$ 50mM	65.47	32.06	0.46	12.46	4.81	92.80	17.71
	$CaCl_2$ 50mM	67.00	32.06	0.51	11.32	4.81	91.57	20.20

Average contact angle of EG and diiodomethane were 25.1° and 35.9° for NF 90, respectively; 12.6° and 38.7° for NF 270, respectively; 26.7° and 38.2° for XLE, respectively.

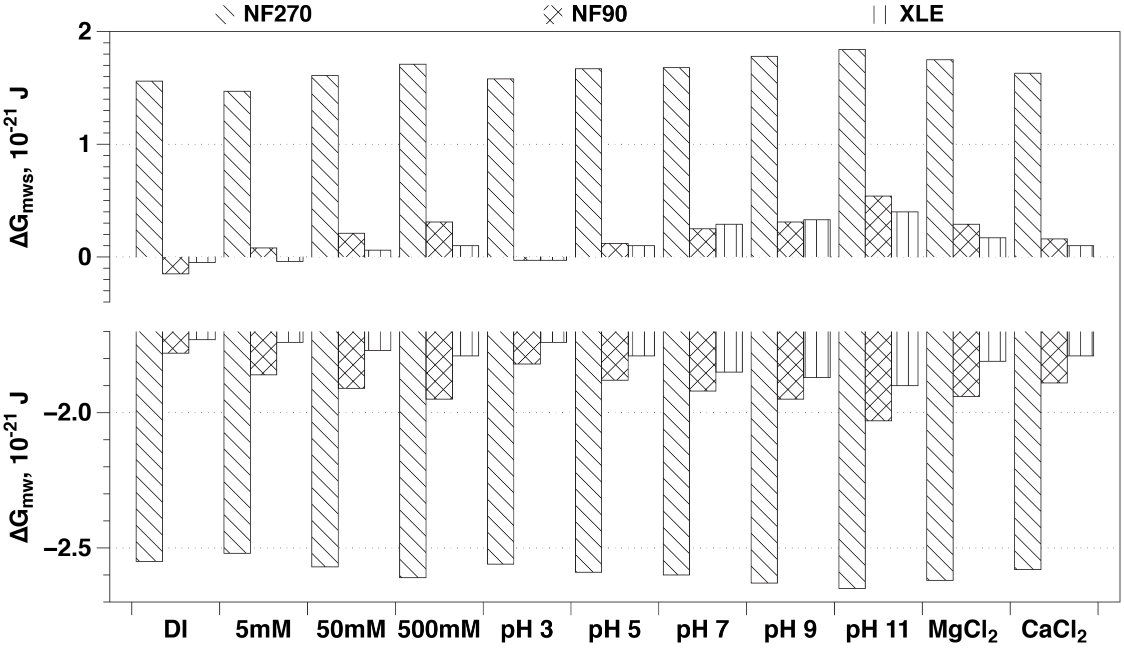

Figure 4.4. Calculated data illustrating the effect of water chemistry on water-membrane interaction energy (Δ*G*$_{mw}$) and solute-membrane interaction energy (Δ*G*$_{mws}$).

Based on the results, water–membrane interaction energy (Δ*G*$_{mw}$) became more negative (hydrophilic), which indicated the partition of water into membrane phase is favored, with increasing ionic strength, pH and presence of divalent cations for all three membranes. The trend is the same as with contact angle, surface tension and interfacial free energy. As the membrane becomes more hydrophilic, the partition of water into membrane phase will be enhanced.

Solute (EG)–membrane interaction energy (Δ*G*$_{mws}$) became more positive with increasing ionic strength, increasing pH and presence of divalent cations for all three membranes. This can be explained by the higher uptake of water, which excludes solute-electron donor interaction between solute and membrane. When the ionic strength or pH of water phase increases, or divalent cations were added into water phase, the electron donor component of membrane surface tension increased (**Table 4.4**). As the electron donor component of EG (Lewis-base) surface tension is relatively high (47 mJ/m^2), the repulsive acid-base interaction (hydrophilic repulsion) between EG and membrane is enhanced [21]. As a result, there will be resistance against partitioning of EG into membrane phase.

4.3.3 Effect of water chemistry on membrane structure

As indicated in transport model (**Eqns. 3.8 and 3.21**), increasing in pore radius (r_p) will lower solute rejection and enhances water flux, however, increasing in structural factor ($S = \Delta x/\varepsilon$) will greater solute retention and result in decline in water flux. Calculated membrane characteristic r_p and S from fitting experimental EG rejection and water flux data into Eqns. 8 and 12 were calculated and plotted in **Figure 4.5**. The details of model fitting were shown in support information. The membrane pore radiuses calculated by model fitting are close to AFM measurement by Hilal et al. [23] and in the range proposed by Kim et al. [24] and Jean et al. [25]. It is important to note that the model fitted structural factor ranged from 30 to 250 nm. As reported from positron annihilation lifetime spectroscopy (PALS) measurements by Chen et al. [26] and Jean et al. [25], the free volume fraction (FFV) of dried polyamide films under vacuum is ~1.5 %. Assuming effective porosity ε is the FFV, then the effective membrane thickness determined from this study's structure factors would range from 0.45 to 3.75 nm. These thickness seem unreasonably small; hence, the accuracy of *ex situ* techniques like PALS could be questioned. That said, it is well know that polyamide composite membranes have very rough coating films; recent numerical simulations suggest permeation occurs predominantly through thinner regions ("valleys") at very high local fluxes ("hot spots") [27]. If that model of rough membrane transport holds up it would suggest that our model fitting approach herein predominantly estimates the structural descriptors for the "hot spots" rather than the area average values such as would be the case for PALS or other *ex situ* characterization methods. Nevertheless, the results here suggest the effective membrane thickness is much smaller than the apparent thicknesses (50 to 200 nm) typically measured by AFM analyses or TEM images.

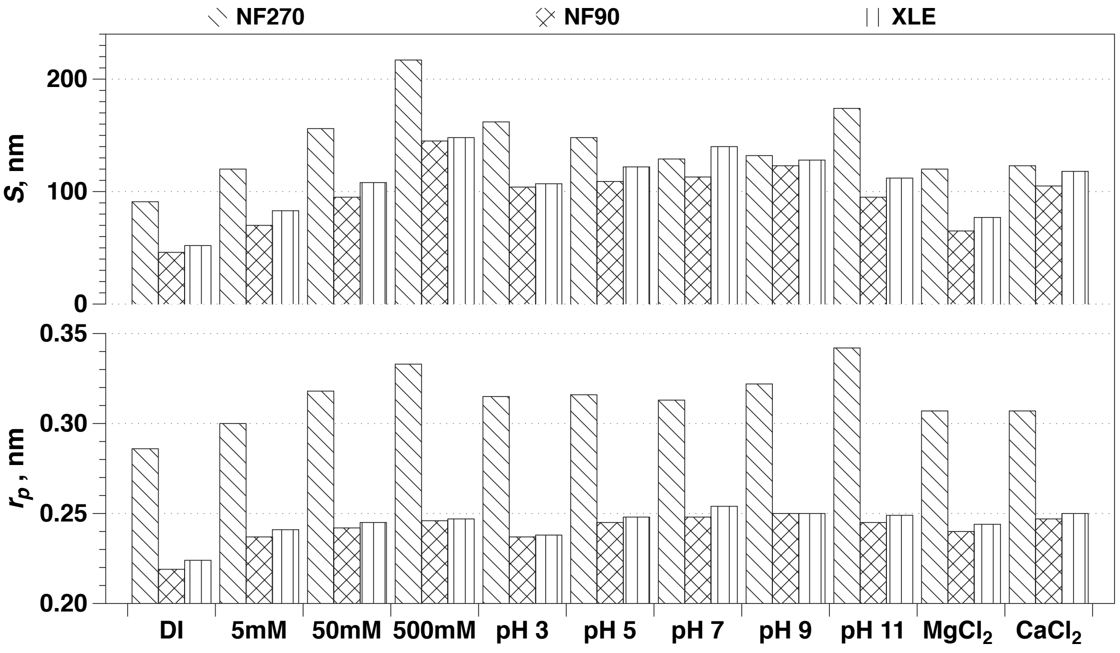

Figure 4.5. Membrane structural descriptors illustrating the apparent effects of water chemistry on membrane pore radius (r_p) and structure factor (S).

As shown in **Figure 4.5**, r_p increased while S decreased with increasing ionic strength from 5 mM to 500 mM for all three membranes. The changes in r_p were relatively less significant than in S. The trend is the same as reported by Luo et al. [14].

The ionic strength effect could be explained by salt induced membrane swelling or de-swelling. The mechanism for membrane swelling by salt is still controversial [12]. Some researchers have attributed it to the electrostatic repulsion between specific sorbed ions on the membrane pore wall or dissociation of polymer structure [9, 28-33]. Others claimed that the salt reduced the electrostatic interaction in the membrane and the hydration layer on membrane pore wall became thinner [14]. As reported by Coronell et al., the pKa values for carboxylic groups in polyamide membranes are 5.23 and 8.97, which suggest membranes contain negative charges in natural water (pH ~ 5 to 10) [34]. When salt ions were added into feed water, cations were sorbed onto the negative charged sites in membranes. The strong repulsion of cations would cause swelling of membrane polymer as illustrated in **Figure 4.6a**. "Dense" membranes (*e.g.* NF90 and XLE) swell less than "loose" membranes (*e.g.* NF270) due to fewer ions could enter into relatively small membrane pores than relatively large pores. The changing in repulsion of membrane polymer due to sorbed cations corresponded well with variations in cohesive energy (ΔG_{131}). As discussed previously, ΔG_{131} became more positive when solution ionic strength increased (**Table 4.4**) and more positive ΔG_{131} implies stronger repulsive interactions between membrane polymers. As a result, membrane pore swelled because of stronger repulsion force by sorbed salt ions. On the other hand, increase in S could be explained by increasing in membrane physical thickness (swelling of polymer across the membrane) and increasing in water/solute diffusive path length (higher probability of collisions between water/EG molecules and salt ions when solution ionic strength increased [14]). For NF90 and XLE membranes with relatively small pores, the relatively large increase in *S* was the main reason for the changes in EG rejection and water permeability in response to changes in solution ionic strength. For NF270 membrane with relatively large pores, the increase in r_p mostly accounted for the decrease of EG retention.

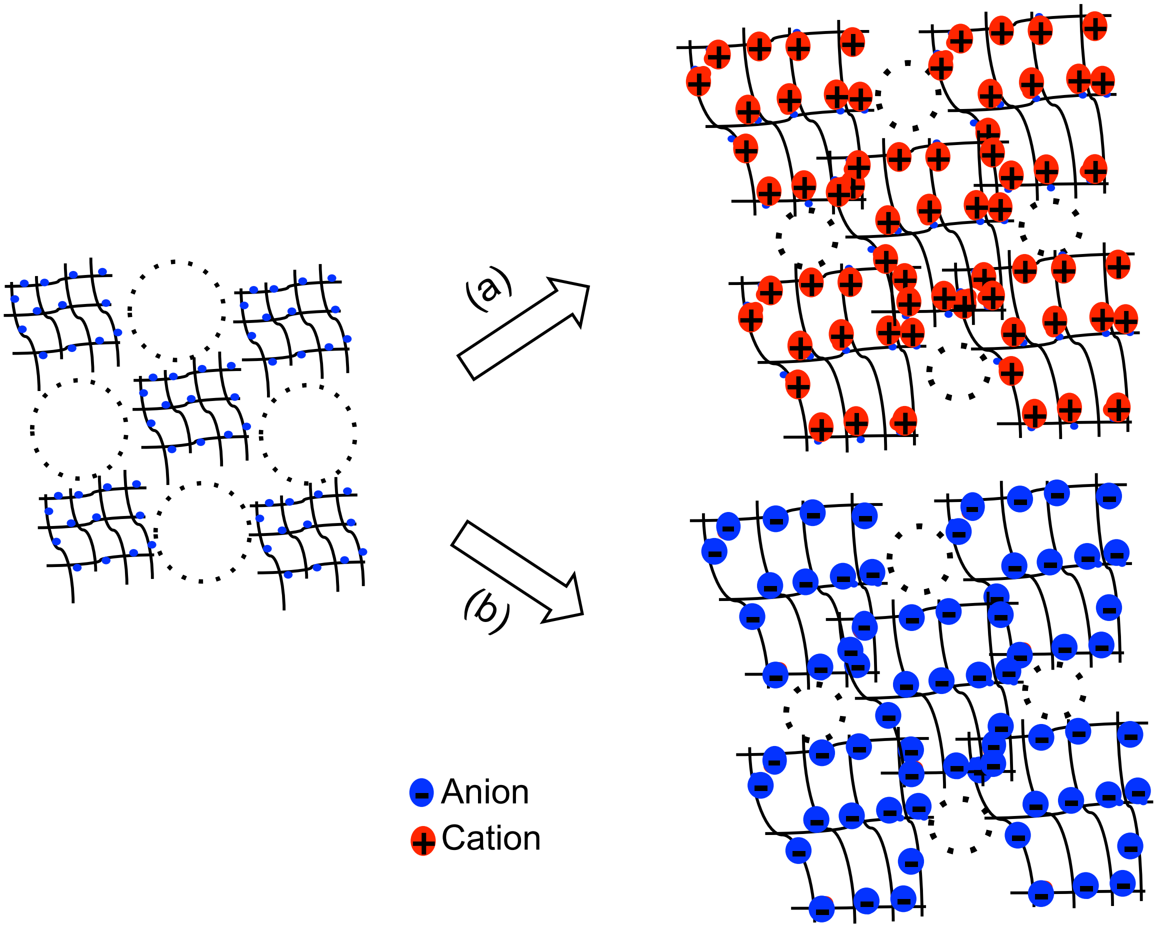

Figure 4.6. Illustration the effect of (a) salt or H^+ and (b) pH on membrane swelling state.

Solution pH also influenced the membrane structure properties. Both r_p and *S* increased with increasing solution pH. The reason for the enhanced membrane swelling at basic condition (high pH) may due to the increased repulsion interactions between the enhanced dissociation of carboxylic groups. According to Bandini et al., membrane charge concentration increased with increasing pH [30, 35], as a result, the electrostatic repulsion between membrane pore walls will be enhanced and membranes will swell (**Figure 4.6b**). The rise in repulsive interaction between membranes was also represented by more positive ΔG_{131} values (**Table 4.4**). Due to the increase in r_p with increasing pH, water flux increased and EG retention decreased. When the solution pH continued to grow, the water flux declined and EG rejection (except for NF 270) was enhanced because of the further increasing of S.

Divalent cations (Ca^{2+} and Mg^{2+}) in feed solution also swelled the membranes as indicated in **Figure 4.5** that both r_p and S of membranes are larger than with DI water as feed. Compared with monovalent cation (Na^+) with same solution ionic strength, NF90 and XLE membranes were swelled more by divalent cations (greater r_p) because divalent cations have greater electrostatic repulsion [36]. As a result, EG rejection was lower when Ca^{2+} and Mg^{2+} was presenting in feed solution than Na^+ for NF90 and XLE membranes. For NF270 membrane, divalent cations swelled membrane less then monovalent cation as smaller r_p and S were calculated from EG rejection and water permeability data. The results could be explained by the lower positive charge concentration (33 mM) in $Ca/MgCl_2$ solution than positive charge concentration in NaCl solution (50 mM) with same ionic strength. The positive charge provided by divalent cations was not enough to neutralize the negative charged NF270 membrane, which has more unreacted carboxyl groups and higher charge density than NF90 and XLE membranes [37, 38].

4.4 Conclusions

This work presented a feasible method for characterization of apparent structural descriptors of NF/RO membranes by fitting straightforward water and solute permeation experiments with an extended solution-diffusion transport model. The results obtained in this study provide new insights about the impacts of feed water chemistry on membrane transport, interfacial and structural properties for three commercial polyamide composite membranes. All polyamide composite membranes swell with different extents while changing feed water chemistry due to repulsions between sorbed cations or increasing membrane charge density. Water flux, salt rejection and neutral solute rejection changed dramatically with water chemistry, but all were largely reversible further supporting salt induced swelling and de-swelling phenomena. Model derived structural descriptors (i.e., r_p and S) should be considered semi-quantitative representations of the free volume of the membrane in a given water chemistry under realistic filtration conditions; the numbers obtained in this study fell well within the ranges previously reported using independent characterization methods [23, 39]. These results offer powerful new insights into polyamide NF/RO membrane performance suggesting we are inching closer to predictive capabilities. However, further model development and study is needed to elucidate the effects of feed water chemistry on membrane structure and charged solute transport.

4.5 List of Symbols

A	water permeability
A_s	solute-membrane contact area
A_w	water-membrane contact area
c	concentration within membrane
C_f	solute concentration of feed solution
C_p	solute concentration of permeate solution
$C_{w,f}$	water concentration at feed side of membrane
$C_{w,m}$	water concentration in membrane
$C_{w,p}$	water concentration in membrane pore
$D_{w,m}$	water diffusion coefficient in membrane
$D_{w,\infty}$	water diffusion coefficient in the bulk
$D_{s,\infty}$	solute diffusion coefficient in the bulk
J_s	solute flux
J_w	water flux
k_B	Boltzmann constant
K_c	convective hindrance factor
K_d	diffusive hindrance factor
K_w	water-membrane partition coefficient
l	membrane thickness
Re	Reynolds number
R_g	gas constant
R_o	observed solute rejection
r	roughness area ratio
r_p	pore radius
r_s	solute Stokes radius
r_w	water Stokes radius
S	structure factor
T	temperature
V_w	molar volume of water
β	concentration polarization factor
γ^-	electron-donor surface tension component
γ^+	electron-acceptor surface tension component
γ^{LW}	Liifshitz-van der Waals surface tension component
γ^{AB}	acid-base surface tension component
γ^{T}	total surface tension
ΔG_{13}	membrane-liquid interfacial free energy
ΔG_{131}	cohesive free energy
ΔG_{mw}	membrane-liquid interaction energy
ΔG_{mws}	membrane-solute interaction energy
Δp	applied pressure
Δx	effective pore length
$\Delta \pi$	osmotic pressure difference across the membrane

ε	porosity
λ_s	solute-membrane sieving factor
λ_w	water-membrane sieving factor
τ	tortuosity
ϕ_s	solute-membrane pore partition coefficient
ϕ_w	water-membrane pore partition coefficient
θ	contact angle

4.6 References

[1] A.R.D. Verliefde, E.R. Cornelissen, S.G.J. Heijman, E.M.V. Hoek, G.L. Amy, B.V.d. Bruggen, J.C. van Dijk, Influence of Solute−Membrane Affinity on Rejection of Uncharged Organic Solutes by Nanofiltration Membranes, Environ Sci Technol, 43 (2009) 2400-2406.

[2] D.R. Lide, Handbook of Chemistry and Physics: 2004-2005, CRC PressI Llc, 2004.

[3] G. Wypych, Knovel Solvents - A Properties Database, in, ChemTec Publishing.

[4] C.C. Miller, The Stokes-Einstein Law for Diffusion in Solution, Proceedings of the Royal Society of London. Series A, Containing Papers of a Mathematical and Physical Character, 106 (1924) 724-749.

[5] X. Jin, X.F. Huang, E.M.V. Hoek, Role of Specific Ion Interactions in Seawater RO Membrane Fouling by Alginic Acid, Environ Sci Technol, 43 (2009) 3580-3587.

[6] G. Hurwitz, G.R. Guillen, E.M.V. Hoek, Probing polyamide membrane surface charge, zeta potential, wettability, and hydrophilicity with contact angle measurements, J Membrane Sci, 349 (2010) 349-357.

[7] R.N. Wenzel, Surface Roughness and Contact Angle, J Phys Colloid Chem, 53 (1949) 1466-1467.

[8] B. Janczuk, W. Wojcik, A. Zdziennicka, Determination of the Components of the Surface-Tension of Some Liquids from Interfacial Liquid-Liquid Tension Measurements, J Colloid Interf Sci, 157 (1993) 384-393.

[9] V. Freger, Swelling and morphology of the skin layer of polyamide composite membranes: An atomic force microscopy study, Environ Sci Technol, 38 (2004) 3168-3175.

[10] A. Braghetta, F.A. DiGiano, W.P. Ball, Nanofiltration of natural organic matter: pH and ionic strength effects, J Environ Eng-Asce, 123 (1997) 628-641.

[11] C. Mazzoni, L. Bruni, S. Bandini, Nanofiltration: Role of the electrolyte and pH on desal DK performances, Ind Eng Chem Res, 46 (2007) 2254-2262.

[12] J. Luo, Y. Wan, Effects of pH and salt on nanofiltration—a critical review, J Membrane Sci, 438 (2013) 18-28.

[13] E. Steinle-Darling, M. Zedda, M.H. Plumlee, H.F. Ridgway, M. Reinhard, Evaluating the impacts of membrane type, coating, fouling, chemical properties and

water chemistry on reverse osmosis rejection of seven nitrosoalklyamines, including NDMA, Water Res, 41 (2007) 3959-3967.

[14] J. Luo, Y. Wan, Effect of highly concentrated salt on retention of organic solutes by nanofiltration polymeric membranes, J Membrane Sci, 372 (2011) 145-153.

[15] S. Kim, H. Ozaki, J. Kim, Effect of pH on the rejection of inorganic salts and organic compound using nanofiltration membrane, Korean J. Chem. Eng., 23 (2006) 28-33.

[16] Y.Z. Xu, R.E. Lebrun, Investigation of the solute separation by charged nanofiltration membrane: effect of pH, ionic strength and solute type, J Membrane Sci, 158 (1999) 93-104.

[17] A. Schdfer, T. Waite, Trace Contaminant Removal Using Hybrid Membrane Processes in Water Recycling, in: Chemical Water and Wastewater Treatment: Proceedings of the 10th Gothenburg Symposium 2002, June 17-19, 2002, Gothenburg, Sweden, International Water Assn, 2002, pp. 319.

[18] C. Bellona, J.E. Drewes, The role of membrane surface charge and solute physico-chemical properties in the rejection of organic acids by NF membranes, J Membrane Sci, 249 (2005) 227-234.

[19] E.R. Nightingale, Phenomenological Theory of Ion Solvation - Effective Radii of Hydrated Ions, J Phys Chem-Us, 63 (1959) 1381-1387.

[20] A.R.D. Verliefde, E.R. Cornelissen, S.G.J. Heijman, J.Q.J.C. Verberk, G.L. Amy, B. Van der Bruggen, J.C. van Dijk, The role of electrostatic interactions on the rejection of organic solutes in aqueous solutions with nanofiltration, J Membrane Sci, 322 (2008) 52-66.

[21] C.J. van Oss, Development and applications of the interfacial tension between water and organic or biological surfaces, Colloids Surf., B, 54 (2007) 2.

[22] E.M. Hoek, V.V. Tarabara, Encyclopedia of Membrane Science and Technology, John Wiley & Sons Canada, Limited, 2013.

[23] N. Hilal, H. Al-Zoubi, N.A. Darwish, A.W. Mohammad, Characterisation of nanofiltration membranes using atomic force microscopy, Desalination, 177 (2005) 187-199.

[24] S.H. Kim, S.Y. Kwak, T. Suzuki, Positron annihilation spectroscopic evidence to demonstrate the flux-enhancement mechanism in morphology-controlled thin-film-composite (TFC) membrane, Environ Sci Technol, 39 (2005) 1764-1770.

[25] Y.C. Jean, W.S. Hung, C.H. Lo, H. Chen, G. Liu, L. Chakka, M.L. Cheng, D. Nanda, K.L. Tung, S.H. Huang, K.R. Lee, J.Y. Lai, Y.M. Sun, C.C. Hu, C.C. Yu, Applications of positron annihilation spectroscopy to polymeric membranes, Desalination, 234 (2008) 89-98.

[26] H.M. Chen, W.S. Hung, C.H. Lo, S.H. Huang, M.L. Cheng, G. Liu, K.R. Lee, J.Y. Lai, Y.M. Sun, C.C. Hu, R. Suzuki, T. Ohdaira, N. Oshima, Y.C. Jean, Free-volume depth profile of polymeric membranes studied by positron annihilation spectroscopy: Layer structure from interfacial polymerization, Macromolecules, 40 (2007) 7542-7557.

[27] G.Z. Ramon, E.M.V. Hoek, Transport through composite membranes, part 2: Impacts of roughness on permeability and fouling, J Membrane Sci, 425–426 (2013) 141-148.

[28] M. Nilsson, G. Tragardh, K. Ostergren, The influence of pH, salt and temperature on nanofiltration performance, J Membrane Sci, 312 (2008) 97-106.

[29] L. Piculell, S. Nilsson, Effects of salts on association and conformational equilibria of macromolecules in solution
Surfactants and Macromolecules: Self-Assembly at Interfaces and in Bulk, in: B. Lindman, J. Rosenholm, P. Stenius (Eds.), Springer Berlin / Heidelberg, 1990, pp. 198-210.

[30] S. Bandini, C. Mazzoni, Modelling the amphoteric behaviour of polyamide nanofiltration membranes, Desalination, 184 (2005) 327-336.

[31] V. Freger, T.C. Arnot, J.A. Howell, Separation of concentrated organic/inorganic salt mixtures by nanofiltration, J Membrane Sci, 178 (2000) 185-193.

[32] G. Bargeman, J.M. Vollenbroek, J. Straatsma, C.G.P.H. Schroen, R.M. Boom, Nanofiltration of multi-component feeds. Interactions between neutral and charged components and their effect on retention, J Membrane Sci, 247 (2005) 11-20.

[33] A. Escoda, P. Fievet, S. Lakard, A. Szymczyk, S. Deon, Influence of salts on the rejection of polyethyleneglycol by an NF organic membrane: Pore swelling and salting-out effects, J Membrane Sci, 347 (2010) 174-182.

[34] O. Coronell, B.J. Marinas, X.J. Zhang, D.G. Cahill, Quantification of functional groups and modeling of their ionization behavior in the active layer of FT30 reverse osmosis membrane, Environ Sci Technol, 42 (2008) 5260-5266.

[35] S. Bandini, J. Drei, D. Vezzani, The role of pH and concentration on the ion rejection in polyamide nanofiltration membranes, J Membrane Sci, 264 (2005) 65-74.

[36] J.C. Crittenden, R.R. Trussell, D.W. Hand, K.J. Howe, G. Tchobanoglous, MWH's Water Treatment: Principles and Design, Wiley, 2012.

[37] C.S. Ong, W.J. Lau, A.F. Ismail, Treatment of dyeing solution by NF membrane for decolorization and salt reduction, Desalination and Water Treatment, 50 (2012) 245-253.

[38] Y.-N. Kwon, K. Shih, C. Tang, J.O. Leckie, Adsorption of perfluorinated compounds on thin-film composite polyamide membranes, Journal of Applied Polymer Science, 124 (2012) 1042-1049.

[39] D.G. Cahill, V. Freger, S.Y. Kwak, Microscopy and, microanalysis of reverse-osmosis and nanofiltration membranes, Mrs Bull, 33 (2008) 27-32.

CHAPTER 5

MECHANISMS OF UNCHARGED TRACE ORGANICS REMOVAL FROM GROUNDWATER BY NF AND RO MEMBRANES

5.1 Introduction

Trace organic pollutants, such as pesticides, hormones and sterols, pharmaceuticals and personal care products, industrial chemicals and by-products, food additives and water treatment by-products, have been detected and reported in all 50 states and 80% analyzed water steams in the U.S. [1-3]. Hence, the importance of advanced water treatment technologies to convert contaminated sources into potable water has increased dramatically in recent years [4]. For example, N-Nitrosodimethylamine (NDMA) can be formed as a disinfection by-product and is often present in water above the detection limit at concentrations below 10 ng/L [5]. In toxicity studies, NDMA has been found to cause cancer through methylation of DNA [6], and hence, is identified as probable human carcinogen. The USEPA has classified 1,4-dioxane as a probable human carcinogen. The concentration level of 1,4-dioxane detected in river, ocean and groundwater samples ranges from 1 to 200 μg/L [7]. Methanol is listed as a reproductive toxicant by the State of California. Methanol also serves as precursor of methyl tert-butyl ether (MTBE), which is a well-known groundwater contaminant [8]. The human toxicity of methanol is associated with formate production from metabolism of methanol, which occurs faster than formate can be metabolized [9]. Methanol was detected in drinking waters in at least 6 of 10 U.S. cities [10].

Recently, nanofiltration (NF) and reverse osmosis (RO) processes have been considered for trace organic removal from ground and surface water. However, low to moderate trace organic solute, especially neutral solute (such as NDMA, 1,4-dioxane), rejection by NF/RO membranes has been reported [11-13]. As reviewed by Bellona et al.

[14], solute physical-chemical properties, membrane properties and feed water chemistries were all identified to have influences on organic solute rejection by NF/RO membranes. However, solute rejections depend on the combination of all above parameters, so there is no single parameter can be used to correlate with solute rejection for prediction purpose. And it is hard to characterize some of the above key parameters, such as structural parameters of NF/RO membrane under filtration condition.

In this study, we experimentally study the rejections of six commercial NF/RO membranes for one model organic solute (ethylene glycol) and three trace organic pollutants (NDMA, 1,4-dioxane, methanol) in simulated groundwater. We present a new approach to characterize the membrane structural properties based on simple filtration experiments and mathematical fitting with transport model. Different parameters describing solute/membrane structure and solute-membrane interaction are used to correlate with solute rejection. And a partition coefficient, which incorporates both solute-membrane structural properties and solute-membrane interaction, is proposed to predict solute rejection by NF/RO membranes.

5.2 Materials and Methods

5.2.1 Membranes and solutes

Representative polyamide NF (NF 90 and NF 270), brackish water RO (BWRO) (XLE), seawater RO (SWRO) (SW30HR, SW30HRLE, SWC3+) membranes were used in all experiments. These membranes were kindly provided by manufacture (Dow Film Tec Corp., Minneapolis, MN and Hydranautics, Oceanside, CA) as flat-sheet samples and were stored in Nanopure deionized water at 4 °C prior to use. Chemical agents used to simulate groundwater chemistry (**Table 5.1**) were analytical grade and purchased form Fisher Scientific (Pittsburgh, PA). The organic solutes used in the rejection test were purchased from Sigma-Aldrich (Sigma-Aldrich, St. Louis, MO) and their properties are summarized in **Table 5.2**. Separation performance of NF and RO membranes was evaluated in a bench scale cross-flow membrane filtration system [15, 16].

Table 5.1. Groundwater (GW) compositions (Santa Monica groundwater).

Component	Unit	Concentration
pH		7.00
Conductivity	mS/cm	1.78
Na^+	mg/L	207
K^+		4
Ca^{2+}		124
Mg^{2+}		24
Cl^-		216
SO_4^{2-}		250
HCO_3^-		366
NO_3^-		6
TDS		1197

Table 5.2. Physical-chemical properties of tested solutes.

Solute	Molecular weight (g/mol)	Stokes radius (nm)	Diffusivity ($\times 10^{-5}$ cm^2/s)	K_{ow}
EG (C2H6O2)	62	0.184	1.16	0.044
1,4-Dioxane (C4H8O2)	88	0.223	0.95	0.537
NDMA (C2H6N2O)	74	0.201	1.06	0.269
Methanol (CH4O)	32	0.130	1.64	0.170

5.2.2 Membrane performance experiment procedures

The separation performance of NF and RO membranes was evaluated in a bench scale cross-flow membrane filtration system equipped with six parallel membrane cells (effective membrane area is 19.4 cm^2, with width of 2.54 cm, length of 7.62 cm and channel height of 0.10 cm, for each membrane cell). The detail of the description of the membrane testing system can be found in elsewhere [15]. Water permeability was determined using simulated groundwater (**Table 5.1**) at 20 °C and applied pressures between 0.48 – 3.10 MPa (70 – 450 psi). The cross-flow rate was set at 0.55 $Gal\cdot min^{-1}$ (3.46×10^{-5} $m^3\cdot s^{-1}$). Flow conditions were controlled, so that the Reynolds number was maintained at 1900 with a mesh spacer in the feed channel. This ensured that the external mass transfer coefficient was 2.42×10^{-4} $m\cdot s^{-1}$, producing a concentration polarization factor in the range of 1.004 – 1.08 for permeate fluxes in the range of 1 $\times10^{-6}$ – 20 $\times10^{-6}$ $m\cdot s^{-1}$. Permeate flux was measured by a digital flow meter (Optiflow 1000, Agilent Technology, Forster City, CA).

Prior to testing, all the membranes were compacted with deionized water at 3.10 MPa (450 psi) and 20 °C for 18 hours. After permeability measurements, the same membranes were used to characterize the selectivity of selected solute. Organic solutes were spiked into deionized water at 10 mg $carbon\cdot L^{-1}$. The concentration was chosen to be able to measure at least 99 % rejection. Solute rejection was found by measuring total organic carbon in feed and permeate solutions. During the rejection experiments, feed pressure was varied (0.48 – 3.10 MPa), while temperature (20 °C) and external mass transfer coefficient (2.42×10^{-4} m/s) were kept constant. In order to eliminate the effect of adsorption of solute onto the membrane surface and into membrane inner structure, feed solution was filtered through all the membranes at 3.10 MPa (450 psi) and 25 °C for 24 hours before rejection tests.

5.2.3 Membrane and solute surface tension and interfacial energy characterization

The membrane and solute surface tensions and water/solute-membrane interaction energies were determined from measured contact angles using an automated contact angle goniometer (DSA10, Krüss GmbH, Hamburg, Germany). At least twelve equilibrium contact angles at different locations were measured for each sample. Contact angles measurement for simulated groundwater (GW, polar liquid), diiodomethane (DM, apolar liquid) and ethylene glycol (EG, polar liquid) enables determination of surface tension components (γ_i^{LW}, γ_i^+ and γ_i^-) for membranes using the extended Young-Dupré equation [17]

$$\gamma_w^T\left(1+\frac{cos\,\theta}{r}\right)=2\left(\sqrt{\gamma_m^{LW}\gamma_w^{LW}}+\sqrt{\gamma_m^+\gamma_w^-}+\sqrt{\gamma_m^-\gamma_w^+}\right) \qquad (5.1)$$

where θ is the contact angle, *r* is the roughness area ratio (i.e. the ratio of actual surface area for a rough surface to the planar area) [18].

Table 5.3. Roughness of membranes.

Membrane	**R_q (nm)**	***SAD* (%)**
NF270	4.0 ± 1.6	0.4 ± 0.2
NF90	40.5 ± 7.0	19.1 ± 5.0
XLE	58.2 ± 14.6	33.6 ± 5.7
SW30HR	71.0 ± 8.7	42.5 ± 2.7
SW30HRLE	108.0 ± 12.0	32.4 ± 7.4
SWC3+	140 ± 21.6	45.3 ± 9.1

R_q: RMS deviation or z-data standard deviation.
SAD: surface area difference, increase in surface area over projected flat plate area (r = 1+ *SAD*).

The membrane surface roughness was analyzed form atomic force microscopy (AFM) measurement (**Table 5.3**). The surface tension components for probe liquids were obtained from literature [19, 20]. The surface tension components of liquids are given in **Table 5.4**. The details of calculation can be found in previous publications [21]

Water-membrane interaction energy (ΔG_{mw}) can be related to the contact area ($A_w = \pi r_w^2/2$) between water molecule and membrane and interfacial surface tension of water and the membrane [22]

$$\Delta G_{mw} = -2A_w\left(\sqrt{\gamma_w^{LW}\gamma_m^{LW}} + \sqrt{\gamma_w^{+}\gamma_m^{-}} + \sqrt{\gamma_w^{-}\gamma_m^{+}}\right) \tag{5.2}$$

The free energy of interaction between solute and membrane immersed in water can be determined from the Dupré equation [22]

$$\Delta G_{smw} = 2A_s\left[\begin{array}{l}\sqrt{\gamma_s^{LW}\gamma_w^{LW}} + \sqrt{\gamma_m^{LW}\gamma_w^{LW}} - \sqrt{\gamma_m^{LW}\gamma_s^{LW}} - \gamma_w^{LW} + \sqrt{\gamma_w^{+}}\left(\sqrt{\gamma_s^{-}} + \sqrt{\gamma_m^{-}} - \sqrt{\gamma_w^{-}}\right) \\ +\sqrt{\gamma_w^{-}}\left(\sqrt{\gamma_s^{+}} + \sqrt{\gamma_m^{+}} - \sqrt{\gamma_w^{+}}\right) - \sqrt{\gamma_m^{-}\gamma_s^{+}} - \sqrt{\gamma_m^{+}\gamma_s^{-}}\end{array}\right] \tag{5.3}$$

where A_s ($A_s = \pi r_s^2/2$) is the contact area between solute molecule and membrane.

Table 5.4. Interfacial tension and free energies of solutes and membranes.

Liquid/membrane	**Contact angle (°)**			γ^{LW}	γ^{+}	γ^{-}	γ^{AB}	γ^{TOT}
	GW	**DM**	**EG**			**(mJ/m^2)**		
DM	n/a	n/a	n/a	50.8	0.0	0.0	0.0	50.8
EG	n/a	n/a	n/a	29.0	1.9	47.0	18.9	47.9
GW	n/a	n/a	n/a	21.8	25.5	25.5	51.0	72.8
NF270	15.4	38.7	12.6	40.1	0.1	63.2	5.1	45.2
NF90	73.1	35.9	25.1	35.9	0.9	6.1	4.7	40.6
XLE	67.5	38.2	26.7	32.1	0.5	11.0	4.8	36.9
SW30HR	28.8	27.9	4.0	33.4	0.03	37.5	2.2	35.6
SW30HRLE	38.4	39.9	6.1	31.7	0.3	32.7	6.3	38.0
SWC3+	50.3	25.3	9.6	33.4	0.2	21.4	3.7	37.1

5.3 Theory

Water/solute-membrane partition coefficient (ϕ_i), which related water/solute concentration in membrane pore and in the bulk, is defined as [21, 23]

$$\phi_{w/s} = \left(1 - \lambda_{w/s}\right)^2 exp\left(-\frac{\Delta G_{mw/smw}}{kT}\right) \tag{5.4}$$

where λ_i is sieving factor ($\lambda_\mathrm{i} = r_i/r_p$), r_p is the membrane pore radius, r_p is the solute radus, k is Boltzmann constant and T is temperature. Structure factor, defined as the ratio of membrane thickness to porosity, was characterized by fitting experimentally measured water flux (J_w) and solute rejection (R) with the following equations.

$$J_w = \frac{\phi_w K_d D_w^\infty}{S} \frac{V_w}{R_g T}\left(\Delta p - \Delta\pi\right) \tag{5.5}$$

$$R = 1 - \frac{\beta\phi_s K_c}{1 - \left(1 - \phi_s K_c\right) exp\left(-\frac{J_w K_c S}{K_d D_s^\infty}\right)} \tag{5.6}$$

Here, Δp is applied pressure, $\Delta\pi$ is osmotic pressure difference across membrane, $D_{w,m}$ and $D_{s,m}$ is water and solute diffusivity in membrane, respectively, V_w is water molar volume, R_g is gas constant, β is concentration polarization factor, while K_d and K_c are the diffusive and convective hindrance factors for solutes in a confined pore [24].

5.4 Results

The free energy difference associated with interaction of water and solute molecules with the membrane material indicates the affinity (attraction or repulsion) of water and solute molecules with membrane polymers [25]. Generally, the sign and magnitude of ΔG_{mw} and ΔG_{smw} are subject to the membrane polymer chemistry and structure, the feed side water chemistry, and (for ΔG_{smw}) the solute chemistry and size (**Table 5.5**). For example, if ΔG_{smw} is positive, the solute is intrinsically repelled by the membrane leading to a smaller partition coefficient, f_s; a negative ΔG_{smw} indicates it is thermodynamically favorable for the solute to be drawn into the membrane matrix and a higher partition coefficient results.

Table 5.5 Membrane structural descriptors and solute/water-membrane interaction energies*.

Membrane	r_p	**S**	**GW**	**EG**	**1,4-Dioxane**	**NDMA**	**Methanol**
	(nm)	**(nm)**			**(×10^{-21} J)**		
NF270	0.303	117	-2.71	1.91	4.60	-1.15	1.71
NF90	0.237	71	-1.72	-0.32	0.17	-5.45	0.18
XLE	0.246	96	-1.78	0.08	0.75	-5.76	0.44
SW30HR	0.230	304	-2.23	1.27	3.94	1.50	1.26
SW30HRLE	0.232	336	-2.20	1.05	3.17	0.40	1.08
SWC3+	0.227	295	-2.00	0.63	2.24	3.02	0.83

*ΔG_{smw} for GW, EG and methanol were calculated using **Eqns. 5.2 and 5.3**, while ΔG_{smw} for 1,4-dioxane and NDMA were obtained from fitting rejection data and membrane structural parameters into **Eqn. 5.6.**

For all membranes, in groundwater NF270 exhibited the most negative ΔG_{mw} value followed by all three SWRO membranes and then NF90 and XLE; this is the order of decreasing hydrophilicity. All membranes except NF90 repelled EG. All the membranes except SWC3+ and SW30HR/HRLE attracted NDMA, while all membranes repelled both 1,4-dioxane and methanol. Also, in **Table 2**, apparent pore radii ranged from about 0.2 nm to about 0.3 nm, which generally agrees with AFM measurements by Hilal et al. [26] and in the range proposed by Kim et al. [27] and Jean et al. [28] for similar NF/RO membranes. All RO membranes had smaller pores than NF270 as expected, but they all shared very close to the same pore size. The structure factor was distinctly larger for all three SWRO membranes suggesting that while they exhibited similar apparent pore size their porosity was lower and/or their polyamide film was thicker [29, 30].

Methanol was poorly rejected by all membranes (**Figure 5.1**). Methanol in simulated groundwater was rejected less than 10% by NF and BWRO membranes and about 20-30% by SWRO membranes, which is consistent with other work [31]. The free energy data above suggest membrane polymers repelled methanol; hence, the low rejection must be attributed to its small size (0.130 nm). Rejection of EG was low for NF270 (18%), which has the largest pore size, and increased for BWRO (50-60%) and further for SWRO membranes (>90%). Fairly low rejection of NDMA was observed for NF270 (11%), NF90 (22%) and XLE membranes (22%), which is similar to other reports [13]; however, SWRO membranes provided 85-90% rejection of NDMA. In this study, 1,4-dioxane had the largest hydrodynamic radius among all tested solutes and was rejected well by all membranes (80-99%) except NF270 (30%). It is important to point out that SWRO membranes offer very high removal of trace organics from this simulated groundwater, which may prove interesting as a new approach to achieving better performance in groundwater remediation albeit at higher energy and operating costs.

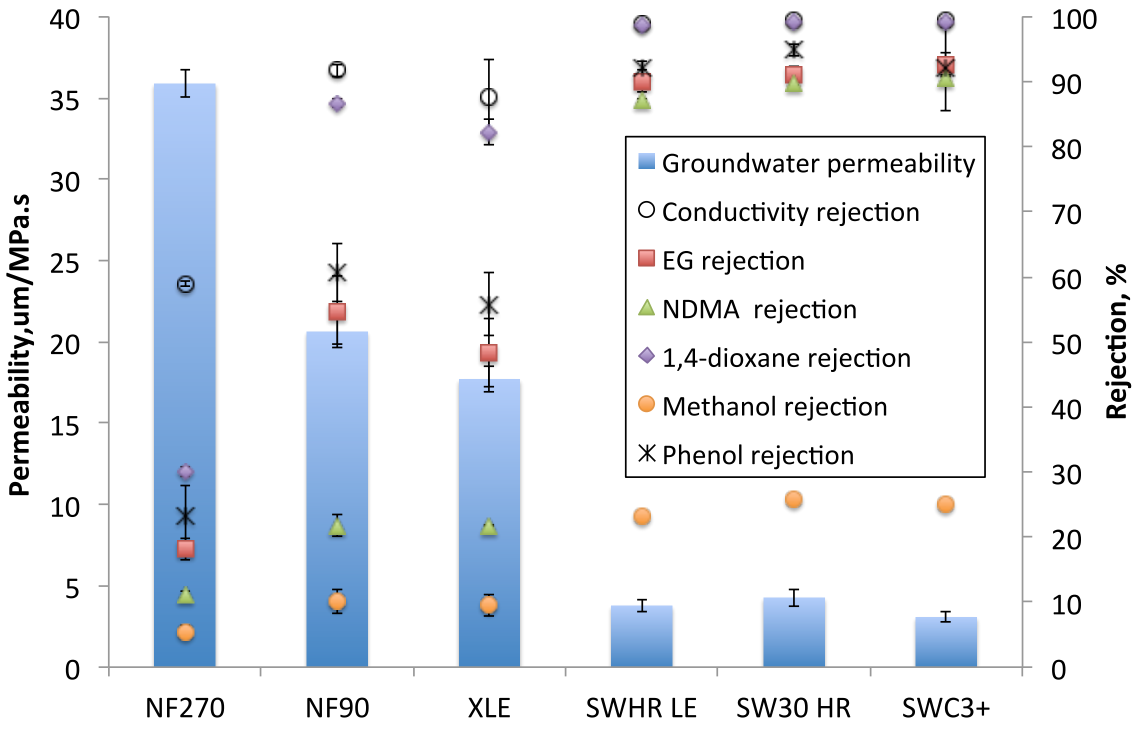

Figure 5.1. Membrane groundwater permeability and solute observed rejection. Solute rejection data were determined at a water flux of 13 µm/s, cross-flow Reynolds number of 1,900 and feed water temperature of 20±2 °C.

5.5 Discussion

Solute rejection by membranes is determined by solute properties, membrane properties, solute-membrane-water interactions and operation conditions that affect water permeation and cross-flow mass transfer [14]. This makes prediction of trace organic removal challenging as there is not a traditional measureable solute parameter (like logK_{ow} for bioaccumulation) that correlates well with observed rejection. In order to predict uncharged trace organics rejection by NF/RO membranes, size exclusion (sieving) factors and thermodynamic (partitioning) factors are often been considered [23, 32-38]. In this study, linear correlation study was performed between solute rejection and various sieving and partitioning factors. Solute-membrane pore partition coefficient, ϕ_s, which accounts for both steric effects and solute-membrane-water interactions, was used in the correlation study first. Re-arranging **Eqn. 5.6** yields

$$\frac{1-exp\left(-\frac{J_w K_c S}{D_\infty K_d}\right)}{\beta}\frac{1}{\phi_s K_c}+\frac{exp\left(-\frac{J_w K_c S}{D_\infty K_d}\right)}{\beta}=\frac{1}{1-R} \tag{5.7}$$

Table 5.6. Summary of values of exp($-J_w K_c S/D_{s,m}$) (T = 298 K).

Membrane	EG	1,4-Dioxane	NDMA	Methanol
NF270	0.998	0.998	0.994	0.999
NF90	0.997	1.000	0.995	0.999
XLE	0.996	1.000	0.986	0.999
SW30 HR	0.991	1.000	0.998	0.996
SWHR LE	0.989	1.000	0.996	0.995
SWC3+	0.991	1.000	0.999	0.996

For constant operation conditions, J_w, β and all parameters in the exponential term should remain constant (as indicated in support information **Table 5.6**); hence, 1/(1-R) should scale with $1/\phi_s$. The correlation coefficient between 1/(1-R) and $1/\phi_s$ was 0.933 (**Figure 5.2a**), so it appears one could predict uncharged organic solute rejection by NF/RO membranes using simply $1/\phi_s$.

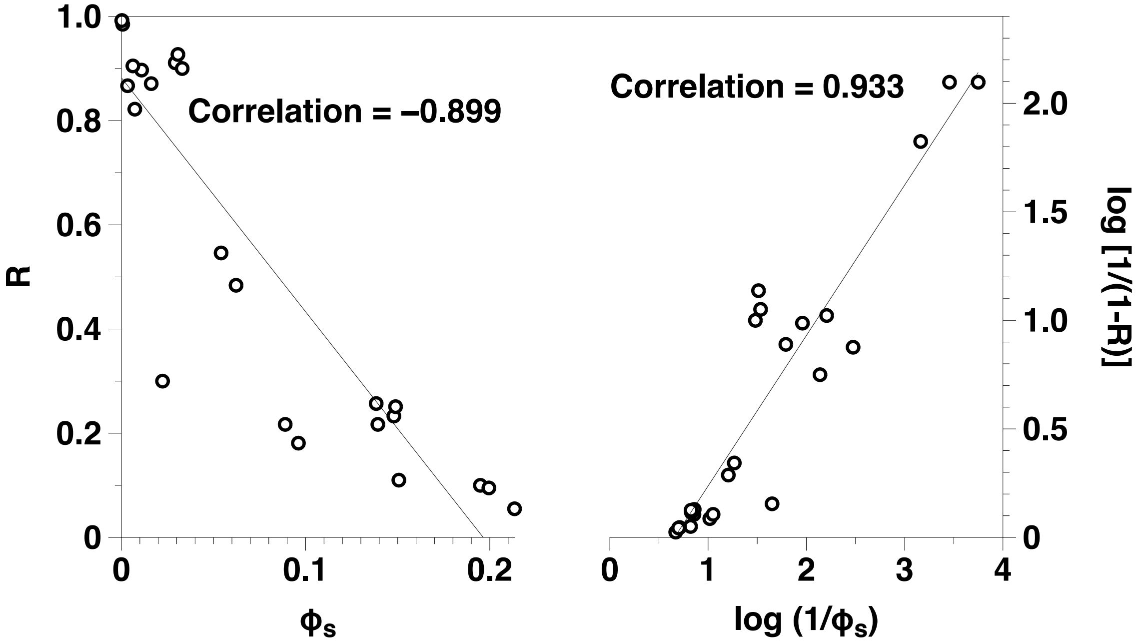

R
1.0
0.8
0.6
0.4
0.2
0
0
0.1
0.2
ϕ_s
Correlation = −0.899
Correlation = 0.933
0
1
2
3
4
$\log(1/\phi_s)$
2.0
1.5
1.0
0.5
0
$\log[1/(1-R)]$

(a)

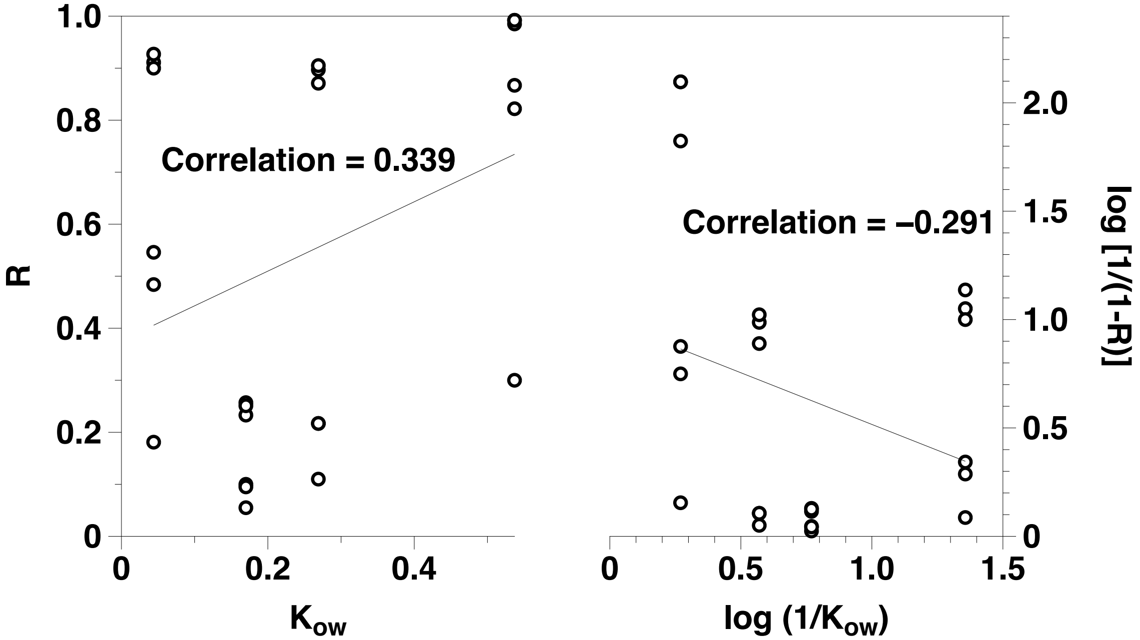

R
1.0
0.8
0.6
0.4
0.2
0
0
0.2
0.4
K_{ow}
Correlation = 0.339
Correlation = −0.291
0
0.5
1.0
1.5
$\log(1/K_{ow})$
2.0
1.5
1.0
0.5
0
$\log[1/(1-R)]$

(b)

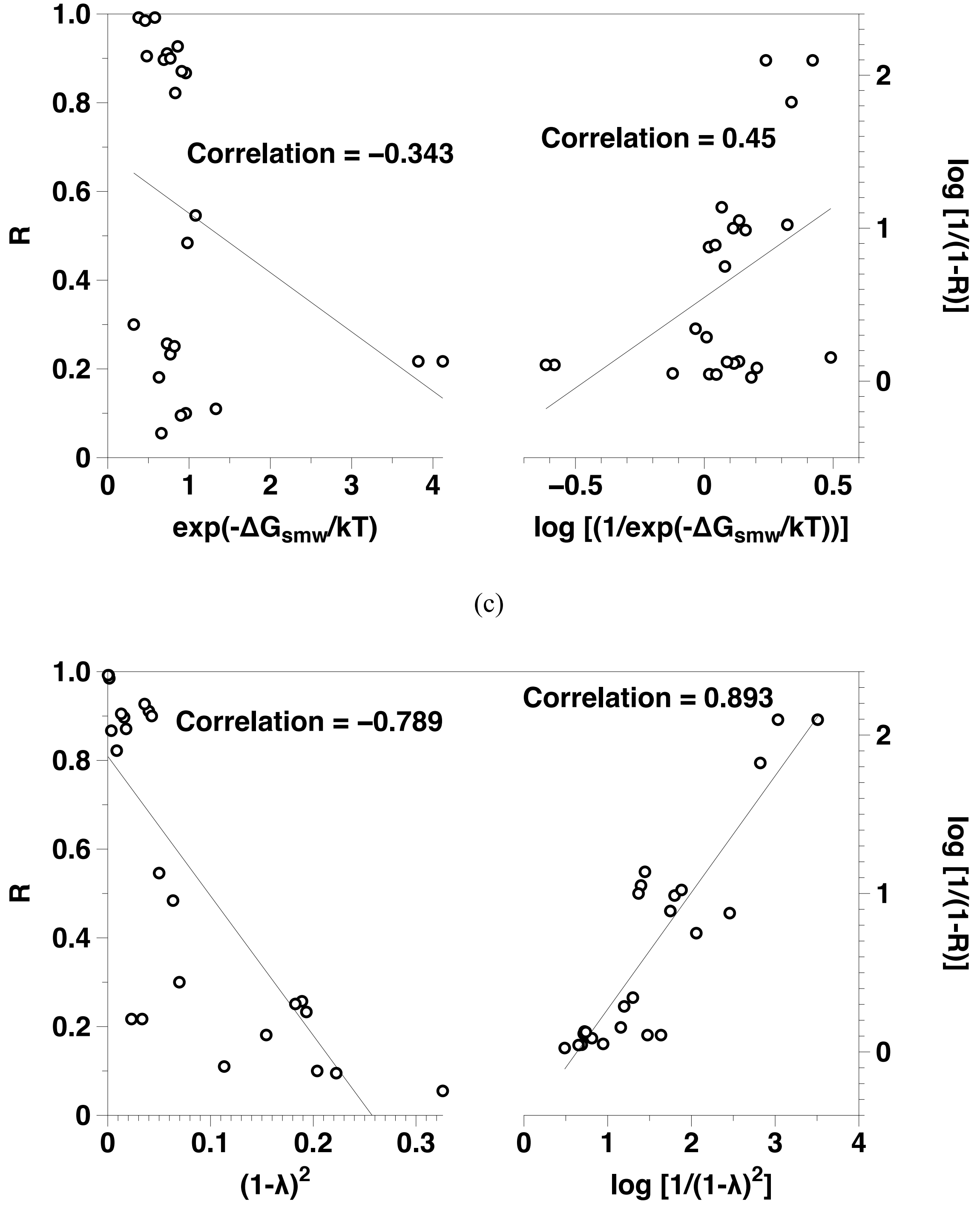

(c)

(d)

Figure 5.2. Correlation coefficient between partition coefficient and rejection.

Other partition coefficients were also investigated here. Traditionally, logK_{ow} is an important and meaningful parameter in assessing environmental behavior of organic pollutants [39]; many researchers have attempted to correlate *R* with K_{ow} of solute [34-38]. However, the results here (**Figure 5.2b**) suggested K_{ow} was not a good predictor of organic solute rejection. The specific interfacial interaction energy between solute and membrane in water (ΔG_{smw}) has also been taken into consideration in other studies [40]. The correlation between exp($-\Delta G_{smw}/kT$) and *R* was weak (**Figure 5.2c**). Some debate remains about the role of steric exclusion in NF/RO membrane transport [41], but here the steric factor, $(1-\lambda)^2$, correlated moderately well with *R* (**Figure 5.2d**), which suggested steric effect might be significant in uncharged trace organics transport through NF/RO membranes.

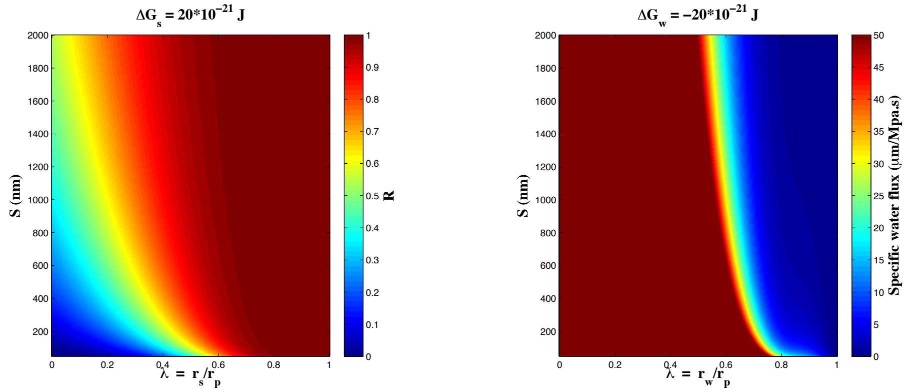

Figure 5.3. Illustration of effect of physical parameters (λ and *S*) and energetic interactions (ΔG) on (a) NDMA rejection based on **Eqn. 5.6** and (b) specific water flux based on **Eqn. 3.8**. ($D_w = 2.20\times10^{-9}$ m^2/s, $D_s = 1.06\times10^{-9}$ m^2/s, $k_f = 9\times10^{-5}$ m/s, $T = 293$ K, $J_w = 5\times10^{-6}$ m/s).

The results presented herein suggest seawater RO membranes could provide very high removal of some trace organic groundwater pollutants, which is not a common application of these membranes. Further, we now have a mechanistic framework for understanding why a given NF/RO membrane rejects a given trace organic pollutant more or less. This mechanistic framework is not yet fully predictive as rejection can change dramatically with different background electrolyte concentrations [16]. Perhaps most interesting and practical is that this new mechanistic framework may shed new light on membrane design for trace organics removal. For example, as shown in **Figure 5.3**, if one could develop a membrane with very positive ΔG_{smw} (*e.g.* 20×10^{-21} J) and very negative ΔG_{mw} (*e.g.* -20×10^{-21} J) to improved organic solute rejection while retaining high flux. However, further studies are needed to understand the rejection of charged solutes by NF/RO membranes in combination with different water chemistries.

5.6 List of Symbols

A	water permeability
A_s	solute-membrane contact area
A_w	water-membrane contact area
c	concentration within membrane
C_f	solute concentration of feed solution
C_p	solute concentration of permeate solution
$C_{w,f}$	water concentration at feed side of membrane
$C_{w,m}$	water concentration in membrane
$C_{w,p}$	water concentration in membrane pore
$D_{w,m}$	water diffusion coefficient in membrane
$D_{w,\infty}$	water diffusion coefficient in the bulk
$D_{s,m}$	solute diffusion coefficient in membrane
$D_{s,\infty}$	solute diffusion coefficient in the bulk
J_s	solute flux
J_w	water flux
k	Boltzmann constant
K_c	convective hindrance factor
K_d	diffusive hindrance factor
K_w	water-membrane partition coefficient
l	membrane thickness
Re	Reynolds number
R_g	gas constant
R	observed solute rejection
r	roughness area ratio
r_p	pore radius
r_s	solute Stokes radius
r_w	water Stokes radius
S	structure factor
T	temperature
V_w	molar volume of water
β	concentration polarization factor
γ^-	electron-donor surface tension component
γ^+	electron-acceptor surface tension component
γ^{LW}	Liifshitz-van der Waals surface tension component
γ^{AB}	acid-base surface tension component
γ^{T}	total surface tension
ΔG_{mw}	membrane-liquid interaction energy
ΔG_{mws}	membrane-solute interaction energy
Δp	applied pressure
Δx	effective pore length
$\Delta\pi$	osmotic pressure difference across the membrane
ε	porosity

λ_s	solute-membrane sieving factor
λ_w	water-membrane sieving factor
τ	tortuosity
ϕ_s	solute-membrane pore partition coefficient
ϕ_w	water-membrane pore partition coefficient
θ	contact angle

5.7 References

[1] M.J. Moran, W.W. Lapham, B.L. Rowe, J.S. Zogorski, Occurrence and status of volatile organic compounds in ground water from rural, untreated, self-supplied domestic wells in the United States, 1986-99, US Department of the Interior, US Geological Survey, 2002.

[2] M.J. Focazio, D.W. Kolpin, K.K. Barnes, E.T. Furlong, M.T. Meyer, S.D. Zaugg, L.B. Barber, M.E. Thurman, A national reconnaissance for pharmaceuticals and other organic wastewater contaminants in the United States - II) Untreated drinking water sources, Sci Total Environ, 402 (2008) 201-216.

[3] D.W. Kolpin, E.T. Furlong, M.T. Meyer, E.M. Thurman, S.D. Zaugg, L.B. Barber, H.T. Buxton, Pharmaceuticals, hormones, and other organic wastewater contaminants in U.S. streams, 1999-2000: a national reconnaissance, Environmental science & technology, 36 (2002) 1202-1211.

[4] M.M. Pendergast, E.M.V. Hoek, A review of water treatment membrane nanotechnologies, Energ Environ Sci, 4 (2011) 1946-1971.

[5] J.W. Charrois, J.M. Boyd, K.L. Froese, S.E. Hrudey, Occurrence of N-nitrosamines in Alberta public drinking-water distribution systems, Journal of Environmental Engineering and Science, 6 (2007) 103-114.

[6] A.I. Schäfer, W. Mitch, S. Walewijk, A. Munoz, E. Teuten, M. Reinhard, Chapter 7 Micropollutants in Water Recycling: A Case Study of N-Nitrosodimethylamine (NDMA) Exposure from Water versus Food, in: C.E. Isabel, I.S. Andrea (Eds.) Sustainability Science and Engineering, Elsevier, 2010, pp. 203-228.

[7] M.J. Zenker, R.C. Borden, M.A. Barlaz, Occurrence and treatment of 1, 4-dioxane in aqueous environments, Environmental Engineering Science, 20 (2003) 423-432.

[8] D. McGregor, Methyl tertiary-Butyl Ether: Studies for Potential Human Health Hazards, Critical Reviews in Toxicology, 36 (2006) 319-358.

[9] WHO, Environmental health criteria 196: methanol, Geneva: WHO, (1997).

[10] T. OOPPA, OPPT Chemical Fact Sheet EPA 749-F-94-013, USEPA, editor, (1994).

[11] E. Steinle-Darling, M. Zedda, M.H. Plumlee, H.F. Ridgway, M. Reinhard, Evaluating the impacts of membrane type, coating, fouling, chemical properties and water chemistry on reverse osmosis rejection of seven nitrosoalklyamines, including NDMA, Water Res, 41 (2007) 3959-3967.

[12] T. Fujioka, L.D. Nghiem, S.J. Khan, J.A. McDonald, Y. Poussade, J.E. Drewes, Effects of feed solution characteristics on the rejection of N-nitrosamines by reverse osmosis membranes, J Membrane Sci, 409 (2012) 66-74.

[13] V.A.Y. Quintanilla, Rejection of emerging organic contaminants by nanofiltration and reverse osmosis membranes: effects of fouling, modelling and water reuse, CRC Press Inc., 2010.

[14] C. Bellona, J.E. Drewes, P. Xu, G. Amy, Factors affecting the rejection of organic solutes during NF/RO treatment - a literature review, Water Res, 38 (2004) 2795-2809.

[15] X. Jin, X.F. Huang, E.M.V. Hoek, Role of Specific Ion Interactions in Seawater RO Membrane Fouling by Alginic Acid, Environmental science & technology, 43 (2009) 3580-3587.

[16] J. Wang, Y. Mo, S. Mahendra, E.M.V. Hoek, Effects of Water Chemistry on Structure and Performance of Polyamide Composite Membranes, J Membrane Sci, accepted, in press (2013).

[17] G. Hurwitz, G.R. Guillen, E.M.V. Hoek, Probing polyamide membrane surface charge, zeta potential, wettability, and hydrophilicity with contact angle measurements, J Membrane Sci, 349 (2010) 349-357.

[18] R.N. Wenzel, Surface Roughness and Contact Angle, J Phys Colloid Chem, 53 (1949) 1466-1467.

[19] B. Janczuk, W. Wojcik, A. Zdziennicka, Determination of the Components of the Surface-Tension of Some Liquids from Interfacial Liquid-Liquid Tension Measurements, J Colloid Interf Sci, 157 (1993) 384-393.

[20] F.B. Peng, Z.Y. Jiang, E.M.V. Hoek, Tuning the molecular structure, separation performance and interfacial properties of poly(vinyl alcohol)-polysulfone interfacial composite membranes, J Membrane Sci, 368 (2011) 26-33.

[21] A.R.D. Verliefde, E.R. Cornelissen, S.G.J. Heijman, E.M.V. Hoek, G.L. Amy, B. Van Der Bruggen, J.C. Van Dijk, Influence of Solute-Membrane Affinity on Rejection of Uncharged Organic Solutes by Nanofiltration Membranes, Environmental science & technology, 43 (2009) 2400-2406.

[22] C.J. van Oss, Development and applications of the interfacial tension between water and organic or biological surfaces, Colloids Surf., B, 54 (2007) 2.

[23] S. Bhattacharjee, A. Sharma, P.K. Bhattacharya, Estimation and influence of long range solute. Membrane interactions in ultrafiltration, Ind Eng Chem Res, 35 (1996) 3108-3121.

[24] P.M. Bungay, H. Brenner, The motion of a closely-fitting sphere in a fluid-filled tube, International Journal of Multiphase Flow, 1 (1973) 25.

[25] E.M. Hoek, V.V. Tarabara, Encyclopedia of Membrane Science and Technology, John Wiley & Sons Canada, Limited, 2013.

[26] N. Hilal, H. Al-Zoubi, N.A. Darwish, A.W. Mohammad, Characterisation of nanofiltration membranes using atomic force microscopy, Desalination, 177 (2005) 187-199.

[27] S.H. Kim, S.Y. Kwak, T. Suzuki, Positron annihilation spectroscopic evidence to demonstrate the flux-enhancement mechanism in morphology-controlled thin-film-composite (TFC) membrane, Environmental science & technology, 39 (2005) 1764-1770.

[28] Y.C. Jean, W.S. Hung, C.H. Lo, H. Chen, G. Liu, L. Chakka, M.L. Cheng, D. Nanda, K.L. Tung, S.H. Huang, K.R. Lee, J.Y. Lai, Y.M. Sun, C.C. Hu, C.C. Yu, Applications of positron annihilation spectroscopy to polymeric membranes, Desalination, 234 (2008) 89-98.

[29] C.Y.Y. Tang, Y.N. Kwon, J.O. Leckie, Effect of membrane chemistry and coating layer on physiochemical properties of thin film composite polyamide RO and NF membranes II. Membrane physiochemical properties and their dependence on polyamide and coating layers, Desalination, 242 (2009) 168-182.

[30] M. Carmona, M. Khemis, J. Leclerc, F. Lapicque, A simple model to predict the removal of oil suspensions from water using the electrocoagulation technique, Chemical Engineering Science, 61 (2006) 1237-1246.

[31] T. Gullinkala, B. Digman, C. Gorey, R. Hausman, I.C. Escobar, Chapter 4 Desalination: Reverse Osmosis and Membrane Distillation, in: C.E. Isabel, I.S. Andrea (Eds.) Sustainability Science and Engineering, Elsevier, 2010, pp. 65-93.

[32] W.M. Deen, Hindered Transport of Large Molecules in Liquid-Filled Pores, Aiche J, 33 (1987) 1409-1425.

[33] Y. Kiso, K. Muroshige, T. Oguchi, T. Yamada, M. Hhirose, T. Ohara, T. Shintani, Effect of molecular shape on rejection of uncharged organic compounds by nanofiltration membranes and on calculated pore radii, J Membrane Sci, 358 (2010) 101-113.

[34] Y. Kiso, Factors Affecting Adsorption of Organic Solutes on Cellulose-Acetate in an Aqueous-Solution System, Chromatographia, 22 (1986) 55-58.

[35] K.O. Agenson, J.I. Oh, T. Urase, Retention of a wide variety of organic pollutants by different nanofiltration/reverse osmosis membranes: controlling parameters of process, J Membrane Sci, 225 (2003) 91-103.

[36] Y. Kiso, T. Kon, T. Kitao, K. Nishimura, Rejection properties of alkyl phthalates with nanofiltration membranes, J Membrane Sci, 182 (2001) 205-214.

[37] B. Van der Bruggen, L. Braeken, C. Vandecasteele, Evaluation of parameters describing flux decline in nanofiltration of aqueous solutions containing organic compounds, Desalination, 147 (2002) 281-288.

[38] Y. Kiso, Y. Nishimura, T. Kitao, K. Nishimura, Rejection properties of non-phenylic pesticides with nanofiltration membranes, J Membrane Sci, 171 (2000) 229-237.

[39] D.W. Hawker, D.W. Connell, Octanol Water Partition-Coefficients of Polychlorinated Biphenyl Congeners, Environmental science & technology, 22 (1988) 382-387.

[40] A.R.D. Verliefde, E.R. Cornelissen, S.G.J. Heijman, E.M.V. Hoek, G.L. Amy, B.V.d. Bruggen, J.C. van Dijk, Influence of Solute−Membrane Affinity on Rejection of Uncharged Organic Solutes by Nanofiltration Membranes, Environmental science & technology, 43 (2009) 2400-2406.

[41] A. Ben-David, S. Bason, J. Jopp, Y. Oren, V. Freger, Partitioning of organic solutes between water and polyamide layer of RO and NF membranes: Correlation to rejection, J Membrane Sci, 281 (2006) 480-490.

CHAPTER 6

CONCLUSIONS AND FUTURE WORK

6.1 Major Conclusions

An impressive amount of work regarding modeling solvent and solute transport in osmotic membranes has been reviewed and summarized as follows:

1. Membrane structural characteristics (*i.e.* pore size, porosity, pore length, and tortuosity) should be included in transport models to help mechanistically explain membrane transport and to enable predictions of membrane performance.

2. Support membrane structure needs to be incorporated into composite membrane transport models since skin layer pore size and porosity significantly impact composite membrane permeability and rejection.

3. Both external (ECP) and internal concentration polarization (ICP) play crucial roles in membrane transport. Understanding and modeling concentration polarization is critical for membrane applications.

An extension of the classical solution-diffusion model for NF/RO membranes has been developed and validated.

1. In general, model predictions agree well with experimental data suggesting the model captures the phenomenological behavior of commercial NF/RO membranes for separations.

2. The model suggests the “effective pore size” may be on the order of 0.24 to 0.35 nm and the “effective diffusion path length” (i.e., barrier layer thickness) may be on the order of 10 to 20 nm; model-derived pore sizes are consistent with literature reported values for the same membranes, but thicknesses are an order of magnitude less than what is historically related to polyamide coating film thickness. These new insights provide a

framework for the creation of next-generation NF/RO membrane structures specifically targeting emerging trace organic contaminants of concern for human health and environmental protection.

3. The dependences of operation parameters, membrane structure parameters and solute properties were also clearly presented by the modeling prediction. With given membranes, applying optimal operation condition (permeate flux, mass transfer coefficient) can enhance the solute rejection. These results suggest it is possible and important to fine-tune the surface tension of membrane and membrane structure (pore size, porosity, thickness) to achieve high selectivity for certain solute.

A feasible method for characterization of apparent structural descriptors of NF/RO membranes by fitting straightforward water and solute permeation experiments with an extended solution-diffusion transport model has been developed. The effects of water chemistry on membrane structure, transport and interfacial properties were explored.

1. All polyamide composite membranes swell with different extents while changing feed water chemistry due to repulsions between sorbed cations or increasing membrane charge density.

2. Water flux, salt rejection and neutral solute rejection changed dramatically with water chemistry, but all were largely reversible further supporting salt induced swelling and de-swelling phenomena.

3. These results offer powerful new insights into polyamide NF/RO membrane performance suggesting we are inching closer to predictive capabilities.

The removal mechanisms of trace organic pollutant by NF/RO membranes were studied.

1. Seawater RO membranes could provide very high removal of some trace organic groundwater pollutants, which is not a common application of these membranes.

2. A mechanistic framework for understanding why a given NF/RO membrane rejects a given trace organic pollutant more or less has been presented. Perhaps most interesting and practical is that a partition coefficient can be used to predict trace organics rejection by NF/RO membranes.

3. This new mechanistic framework may shed new light on membrane design for trace organics removal.

6.2 Future Research

The results and conclusions summarized from this dissertation have provided insights and tools to understand trace organic pollutants transport through and removal mechanisms of NF/RO membranes. Also, questions regarding the limitation of this study open new angles for future research.

1. How to accurately model charged solute transport through NF/RO membrane? Classical models regarding charged solute are mainly based on Donnan exclusion mechanism, which is developed for ion exchange process. Charged solute-membrane interaction (affinity) should be included into the transport equation. Some researchers tried to use electrical potential to describe the interactions between membrane and charged solute (Chapter 2). However, it is hard to directly or indirectly characterize the electrical potential.

2. How to compare membrane structure parameter calculated from transport model with independent physical characterization? This study has provided a feasible way to characterize membrane structure and the obtained values are close to the values reported in the literatures (Chapter 3 and 4). However, independent physical characterization evidences are still required to validate the method proposed in this study.

3. Can the membrane be tailored to maximize rejection to certain solute while maintaining reasonable water flux? According to the model simulation results (Chapter 3), membrane structure has the same effect on solute and water flux. So, there is no optimal membrane structure for increasing solute rejection without scarifying water permeability. As discussed in Chapter 2 and 5, if one could develop a membrane with very positive ΔG_{smw} and very negative ΔG_{mw} to improved organic solute rejection while retaining high flux. For apolar solutes removal, this can be achieved by selecting a hydrophilic (polar) membrane. However, to remove a hydrophilic solute, it is hard to find a membrane material with both large positive ΔG_s and large negative ΔG_w, because solid materials are predominantly monopolar electron-donors.

APPENDIX

APPENDICES FOR CHAPTER 4

Table A4.1
Water-membrane and solute (EG)-membrane interaction energies. (Corresponding to Figure 4.4)

Electrolytes	**NF90**		**NF270**		**XLE**	
	ΔG_{swm} (10^{-21}J)	**ΔG_{mw} (10^{-21}J)**	**ΔG_{swm} (10^{-21}J)**	**ΔG_{mw} (10^{-21}J)**	**ΔG_{swm} (10^{-21}J)**	**ΔG_{mw} (10^{-21}J)**
DI	-0.15	-1.78	1.56	-2.55	-0.05	-1.73
NaCl 5mM	0.08	-1.86	1.47	-2.52	-0.04	-1.74
NaCl 50mM	0.21	-1.91	1.61	-2.57	0.06	-1.77
NaCl 500mM	0.31	-1.95	1.71	-2.61	0.10	-1.79
NaCl 50mM, pH=3	-0.03	-1.82	1.58	-2.56	-0.03	-1.74
NaCl 50mM, pH=5	0.12	-1.88	1.67	-2.59	0.10	-1.79
NaCl 50mM, pH=7	0.25	-1.92	1.68	-2.60	0.29	-1.85
NaCl 50mM, pH=9	0.31	-1.95	1.78	-2.63	0.33	-1.87
NaCl 50mM, pH=11	0.54	-2.03	1.84	-2.65	0.40	-1.90
$MgCl_2$ 50mM	0.29	-1.94	1.75	-2.62	0.17	-1.81
$CaCl_2$ 50mM	0.16	-1.89	1.63	-2.58	0.10	-1.79

Table A4.2
Membrane structural parameters. (Corresponding to Figure 4.5)

Solutions	**NF90**		**XLE**		**NF270**	
	r_p (nm)	**S (nm)**	**r_p (nm)**	**S (nm)**	**r_p (nm)**	**S (nm)**
DI	0.219	46	0.224	52	0.286	91
NaCl 5mM	0.237	70	0.241	83	0.300	120
NaCl 50mM	0.242	95	0.245	108	0.318	156
NaCl 500mM	0.246	145	0.247	148	0.333	217
NaCl 50mM, pH=3	0.237	104	0.238	107	0.315	162
NaCl 50mM, pH=5	0.245	109	0.248	122	0.316	148
NaCl 50mM, pH=7	0.248	113	0.254	140	0.313	129
NaCl 50mM, pH=9	0.250	123	0.250	128	0.322	132
NaCl 50mM, pH=11	0.245	95	0.249	112	0.342	174
$CaCl_2$ 50mM	0.240	65	0.244	77	0.307	120
$MgCl_2$ 50mM	0.247	105	0.250	118	0.307	123

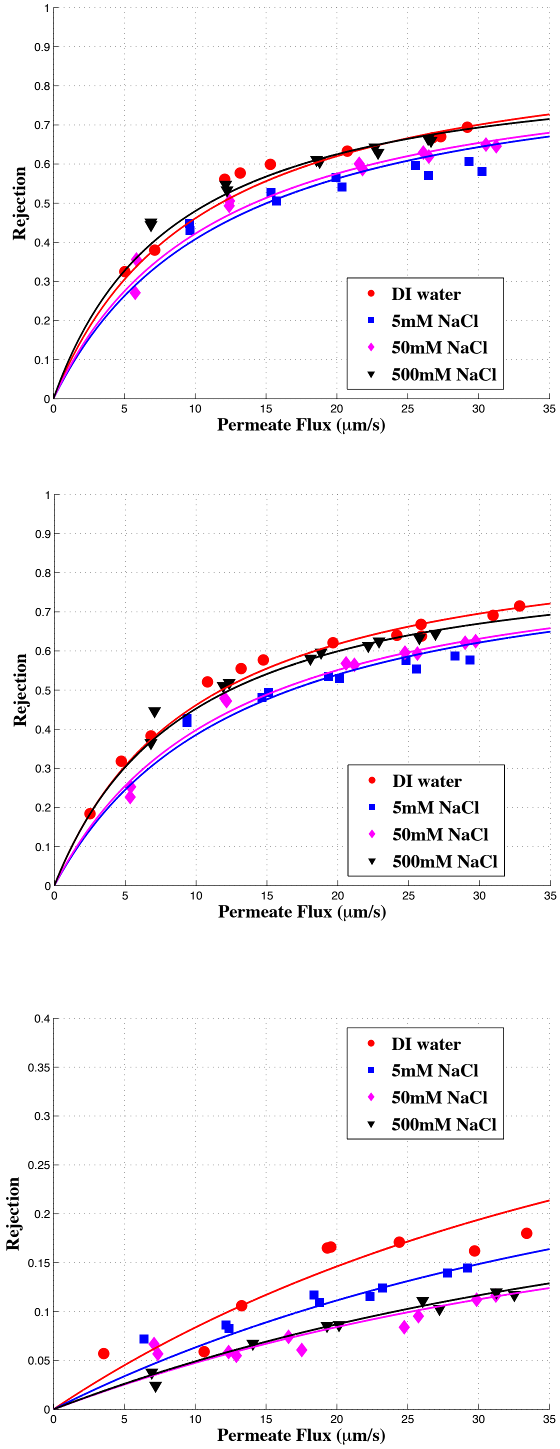

(a)

(b)

(c)

Figure A4.1. Experimental data and model fits illustrating the effects of ionic strength and water flux on EG rejection for (a) NF90, (b) XLE and (c) NF270 membranes.

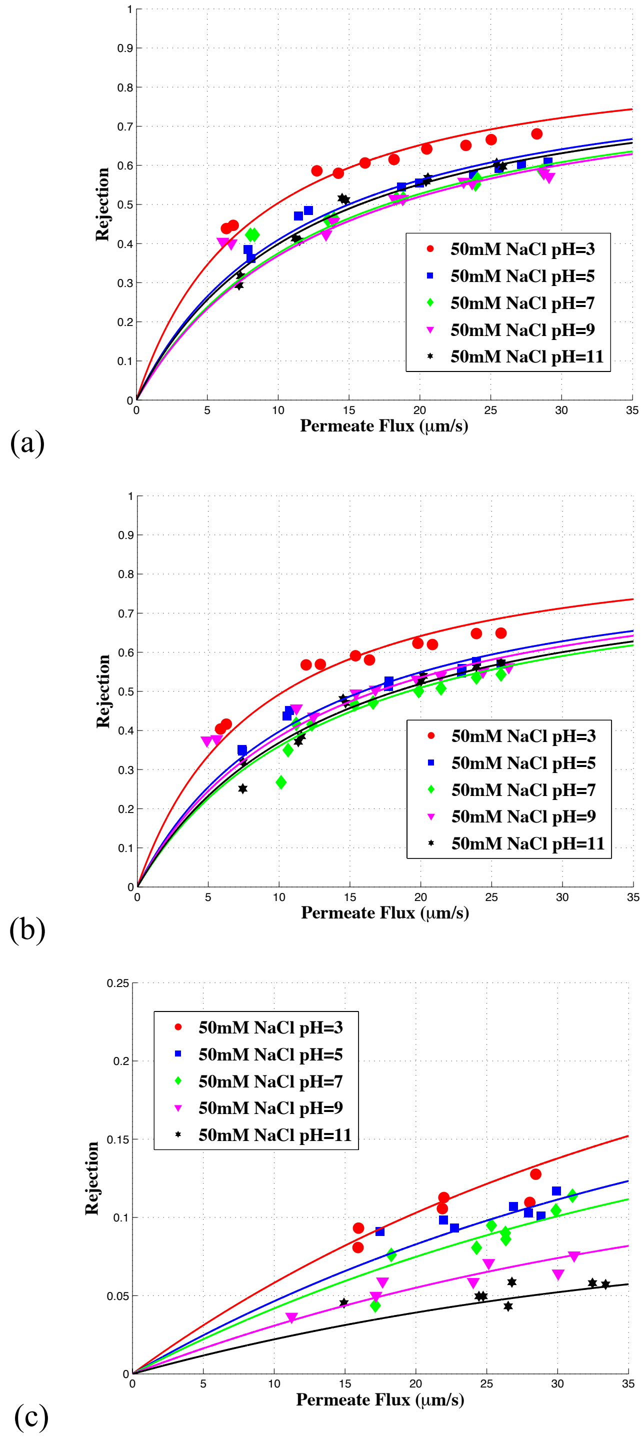

Figure A4.2. Experimental data and model fits illustrating the effects of pH and water flux on EG rejection for (a) NF90, (b) XLE and (c) NF270 membranes.

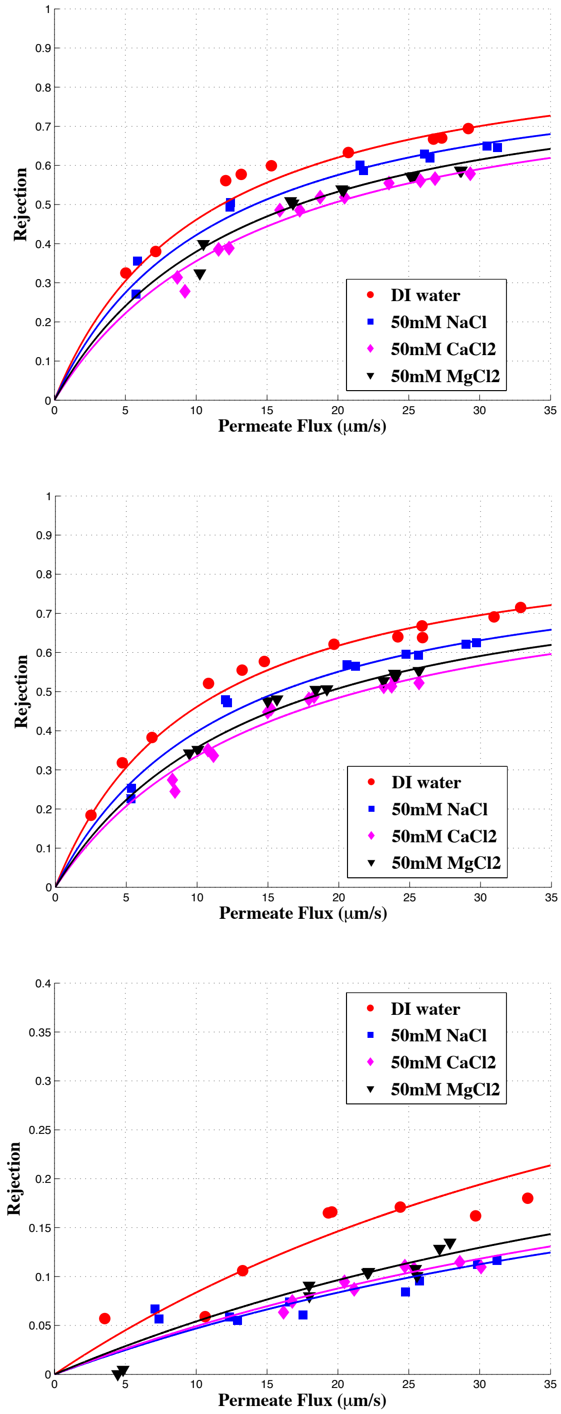

(a)

(b)

(c)

Figure A4.3. Experimental data and model fits illustrating the effects of divalent cations and water flux on EG rejection for (a) NF90, (b) XLE and (c) NF270 membranes.